



Title	Formation and evolution of giant molecular clouds in a barred spiral galaxy
Author(s)	藤本, 裕輔
Citation	北海道大学. 博士(理学) 甲第12238号
Issue Date	2016-03-24
DOI	10.14943/doctoral.k12238
Doc URL	http://hdl.handle.net/2115/61705
Type	theses (doctoral)
File Information	Yusuke_Fujimoto.pdf



[Instructions for use](#)

Formation and evolution of giant molecular clouds in a barred
spiral galaxy
(棒渦巻銀河における巨大分子雲の形成と進化)

藤本裕輔
Yusuke Fujimoto

Department of CosmoSciences, Graduate School of Science, Hokkaido University
(北海道大学大学院理学院宇宙理学専攻)

March, 2016
(平成28年3月)

Abstract

Understanding where and how gas is converted into stars in a galaxy is important for understanding a galaxy's formation and evolution through each epoch of the universe. Which physical processes control the star formation in a galaxy is heavily debated.

We are now at a stage where it is possible to investigate the giant molecular clouds (GMC) and star formation, while also taking global galactic dynamics into account. Thanks to high resolution and sensitive observations from sources such as the millimeter/submillimeter observations by ALMA and infrared observations by Spitzer and Herschel, it is becoming possible to statistically explore GMC and star forming regions through observations in nearby galaxies. In theoretical works, we can also now investigate the formation and evolution of individual GMCs using hydrodynamical isolated galaxy simulations with a self-consistent multiphase interstellar medium (ISM) thanks to developments of super-computer and effective algorithms.

Recent observations (high resolution, but not enough to resolve down to GMC scale yet) have shown the star formation activity changing between galactic-scale environments. The star formation efficiencies (SFEs) have systematic variations larger than one order of magnitude between different galaxy types and between different regions within a galaxy. This means that the gas density is not the only factor that determines the star formation activity in a galaxy. In particular, observations of barred galaxies showed that a central bar region has a lower SFE than that in the spiral arm regions even when the gas surface densities are almost the same.

Why does the star formation activity differ depending on the galactic structure's different environments? This question is key to understanding the galactic-scale star formation and has been the focus of my doctoral research. To understand this, it is important to investigate how the formation and evolution of GMCs is affected by the galactic structures. This is because the GMCs are the star formation spots in a galaxy; they are formed from the cold phase of the ISM, and their densest pockets are the birth place of stars.

We performed three-dimensional hydrodynamical simulations of a barred spiral galaxy. We clarified that galactic environments and stellar feedbacks affect GMC formation and evolution, and that could explain the different star formation activities in a barred spiral galaxy. These works consists of three parts. They are summarised below.

[1] Environmental dependence of GMCs in a barred spiral galaxy

Aim. We explored the effects of galactic structures (bar and spiral arms) on GMC formation and evolution in a barred spiral galaxy.

Methods. We performed three-dimensional hydrodynamical simulations of an M83-type barred spiral galaxy. The simulations were run using *Enzo*: a three dimensional adaptive mesh refinement (AMR) hydrodynamics code (Bryan et al., 2014). We used eight levels of refinement, giving a limiting resolution of 1.5 pc. As the typical size of the GMC is about 20 pc, the 1.5 pc resolution is sufficient to investigate the bulk cloud’s properties. Our galaxy was modelled on the barred spiral galaxy, M83, with the initial gas distribution and stellar potential taken from observational results (2MASS data). To follow the evolution of clouds statistically, we used a cloud tracking tool developed in Tasker and Tan (2009). To compare the impact of different galactic environments on cloud properties, we assigned three environment groups in the bar, spiral, and disc regions based on the cloud’s physical location.

Characteristics. 1) We simulated with sufficiently high resolution to investigate the cloud’s properties (e.g. mass, radius, velocity dispersion) taking global galactic gas dynamics into account. 2) We statistically investigated GMC formation and evolution in different environments in one galaxy. Tasker and Tan (2009) also investigated GMC formation and evolution in a disc galaxy, but their model had no bar or spiral arms. Dobbs and Pringle (2013) simulated a spiral galaxy, but they investigated only a small number of clouds around the spiral arm and inter-arm region. 3) We modelled the barred spiral galaxy, M83. M83 is a nearby galaxy and has been observed at various wavelengths. Its GMC properties are being observed by ALMA (Hirota et al., in preparation), and we would directly compare with it.

Results. The GMC distributions and properties are different between the three galactic regions, primarily due to different cloud interaction rates (see Figure 1). In the central bar region, massive giant molecular associations are formed due to a high cloud number density from the elliptical motion boosting interactions between clouds. The violent cloud-cloud interactions form dense tidal filamentary structures around them, which produce gravitationally unbound transient clouds in the filaments. In the outer-disc regions, clouds are more widely spaced and lack filament structures due to the absence of the grand design potential to gather gas and produce less cloud-cloud interactions. Spiral regions have intermediate features.

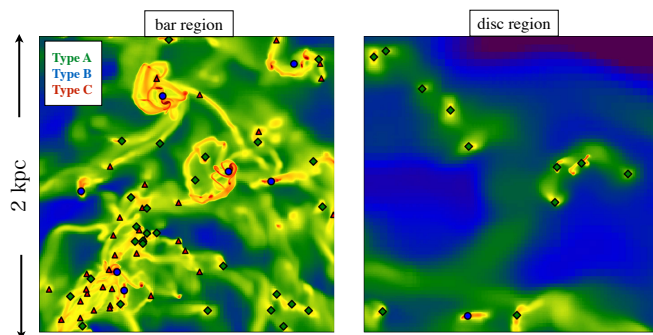


Figure 1. 2 kpc gas surface density images of a region in the bar (left) and disc. Markers show the location of three different cloud types. Green diamonds label Type A clouds, which have the typical values of observed cloud properties. Blue circles mark Type B, which are massive giant molecular associations. Red triangles are Type C, which are unbound, transient clouds.

[2] Environmental dependence of star formation induced by cloud collisions in a barred galaxy

Context. Lower SFE in the bar region than that in spiral arms has been shown by observations of nearby barred galaxies (Momose et al., 2010; Hirota et al., 2014). The physical processes that cause this difference has been debated.

We focus on triggered star formation by cloud-cloud collisions. Fujimoto et al. (2014a) showed that cloud interactions are different between galactic environments, and that gives different cloud populations in each galactic region. We hypothesised that the environmental dependence of star formation might be related to the different cloud interactions between galactic environments.

A cloud-cloud collision is one of the triggering mechanisms of massive star formation; the compressed shocked region caused during the collision forms massive cloud cores where massive star formation would occur (Habe and Ohta, 1992; Takahira et al., 2014). Moreover, Takahira et al. (2014) showed that if the relative velocity is too high in the collision, the core formation rate decreases.

Aim. We aimed to clarify the physical process that causes different SFEs in a barred galaxy.

Methods. We investigated the variation in relative velocity of cloud collisions in different regions of the simulated galaxy performed in Fujimoto et al. (2014a). Using this, we proposed a new model based on the triggered star formation model developed by Tan (2000) that varied the effectiveness of star formation from cloud collisions based on the collision speed. Taking observations of triggered star formation as the most successful velocity for forming stars, we varied the fraction of collisions that would result in star formation. Collisions between 10 and 40 km/s were successful 50 % of the time, while collisions slower and faster than this range were only successful 5 % of the time.

Characteristics. We investigated not only cloud properties but also cloud evolution, such as cloud lifetime, collision rate and collision velocity for all clouds formed in our simulated galaxy. Although several observational studies also have focused on triggered star formation by cloud collisions (e.g. Fukui et al. 2014), it has been difficult to identify the collision, much more statistical studies of them. Our study could help to interpret the observational results.

Results. The collision velocity shows a clear dependence on galactic environment (see Figure 2). Clouds formed in the bar region typically collide faster than those in the spiral. Such speeds can be unproductive, as the collision is over too quickly for gas to collapse. The unproductive collisions in the bar region lower the SFE to put it below the maximum efficiency in the spiral region, as seen in observations.

[3] Stellar feedback effects on GMCs

Context. Fujimoto et al. (2014a) missed the effects of stellar feedback on GMCs. Massive star larger than $8 M_{\odot}$ ejects huge energy into the ISM as a supernova in the end of its life. The effect of stellar feedback on the ISM, GMCs, and star formation has been heavily debated, but a consensus has not been reached yet.

Aim. We aimed to investigate the impact of both galactic structures and supernova feedback on the ISM, GMCs, and star formation.

Methods. We included star formation and thermal supernovae feedback based on Cen and Ostriker (1992) to our galaxy model of Fujimoto et al. (2014a).

Results. The stellar feedback disperses part of the cloud gas, and the ISM density in the inter-cloud region increases (see Figure 3). The high inter-cloud density causes angular momentum loss of clouds due to hydrodynamical drag. Massive clouds lose their angular momentum due to the torque from the hydrodynamical drag. They inflow toward the galactic centre, and then the total gas density in the central bar region rises. This gas supply would be important for evolution of the galaxy centre.

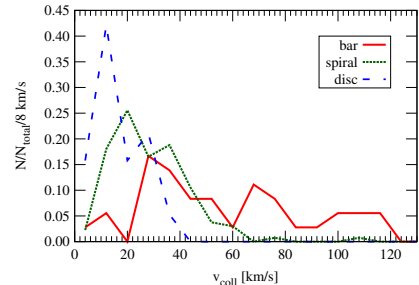


Figure 2. Distribution of the collision velocity of clouds colliding in the three galactic regions.

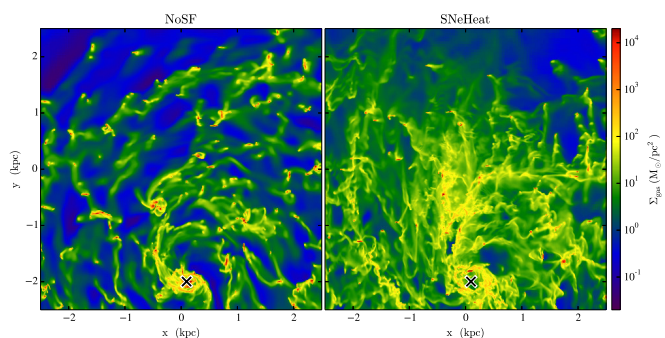


Figure 3. 5 kpc images on the bar-end region of the galactic disc for no feedback run (NoSF) and with feedback run (SNeHeat). x mark at the bottom of the image shows the galactic centre. The galactic disc rotates anticlockwise.

Contents

1	Introduction	9
1.1	Galaxies	9
1.1.1	Components of a galaxy	9
1.1.2	Types of galaxies	10
1.1.3	Barred spiral galaxy	11
1.2	Star formation in galaxies	13
1.2.1	Empirical relation of galactic-scale star formation	13
1.2.2	Environmental dependence of galactic-scale star formation	14
1.3	Giant molecular clouds: stellar nurseries	15
1.3.1	Interstellar medium (ISM)	16
1.3.2	Giant molecular cloud (GMC)	18
1.3.3	Formation and evolution of GMCs in galaxies	22
1.4	Aim of this thesis	22
2	Environmental dependence of GMCs	25
2.1	Introduction	25
2.2	Numerical methods	27
2.2.1	The code	27
2.2.2	The structure of the galactic disc	27
2.2.3	Cloud definition and tracking	30
2.3	Results	31
2.3.1	Global structure and disc evolution	31
2.3.2	Cloud classification based on galactic location	33
2.3.3	Cloud classification based on cloud properties	39
2.3.4	Star formation	44
2.4	Numerical dependences	47
2.4.1	The effect of resolution	47
2.4.2	Comparison between cloud identification methods	49
2.5	Conclusions	51
3	Environmental dependence of SF induced by CCCs	53
3.1	Introduction	53
3.2	Simulation	55
3.3	Results	55
3.3.1	Environmental dependence of collision velocity	55
3.3.2	Environmental dependence of SFE	56
3.4	Conclusion	59
4	Stellar feedback effects on GMCs	61
4.1	Introduction	61
4.2	Numerical methods	63
4.2.1	Simulation and initial conditions	63

4.2.2	Star formation and feedback	64
4.2.3	Cloud analysis	65
4.3	Results	66
4.3.1	The stellar feedback effects on the ISM	66
4.3.2	The stellar feedback effects on star formation	72
4.3.3	The stellar feedback effects on cloud properties	73
4.3.4	The effects of the warm ISM and <i>type C</i> clouds on star formation	79
4.4	Discussions	83
4.4.1	Estimation of the feedback effects	83
4.5	Conclusions	84
5	Conclusion	85
6	Future Prospects	87
6.1	Stellar feedback effects on the GMC evolution	87
6.2	Galactic environmental effects on the GMC evolution	89

Chapter 1

Introduction

Understanding where and how gas is converted into stars in a galaxy is important for understanding a galaxy's formation and evolution through each epoch of the universe. Which physical processes control the star formation in a galaxy is heavily debated, and this has been the focus of my doctoral research.

This chapter is an introduction of this thesis, consisting of three sections. The first section see components of a galaxy, types of galaxies, the barred spiral galaxy M83, which is the modelling galaxy of our simulations, and a brief summary of formation mechanisms of spiral arms and bar structures. The second section see previous studies of galactic-scale star formation focusing on observational works: empirical relation between the gas surface density of the galaxy and the star formation rate density known as the Kennicutt-Schmidt law and environmental dependence of the law suggested by recent high resolution observations. The third section see properties of the interstellar medium (ISM) and the giant molecular clouds (GMCs). GMCs form from the ISM, and stars form in them, so that they are important objects in order to understand the star formation in galaxies. Finally, we see a brief summary of previous theoretical/observational works on formation and evolution of the GMCs in galaxies. Aim of this thesis is described in the end of this introduction chapter.

1.1 Galaxies

1.1.1 Components of a galaxy

A galaxy is composed of dark matter, stars, interstellar gas, and interstellar dust. In case of our galaxy, each total mass is $M_{\text{DM}} \sim 10^{12} M_{\odot}$, $M_{\text{star}} \sim 2 \times 10^{11} M_{\odot}$, $M_{\text{gas}} \sim 10^{10} M_{\odot}$, and $M_{\text{dust}} \sim 10^8 M_{\odot}$.

Figure 1.1 shows a schematic figure of our galaxy looked from the edge-on side. The galaxy is embedded in a spherical dark matter halo, which makes the rotation curve flat. The radius of the halo is more than 20 kpc. The enclosed mass of the halo within 200 kpc is about $10^{12} M_{\odot}$. In the halo, there is almost no stars except globular clusters. The globular cluster consists of a few 10^5 old stars. The size is about 1 pc. There are about 150 globular clusters in our galaxy.

The main parts of our galaxy are a bulge and disk at the center of the dark matter halo. The bulge is an elliptical structure, and the size is about

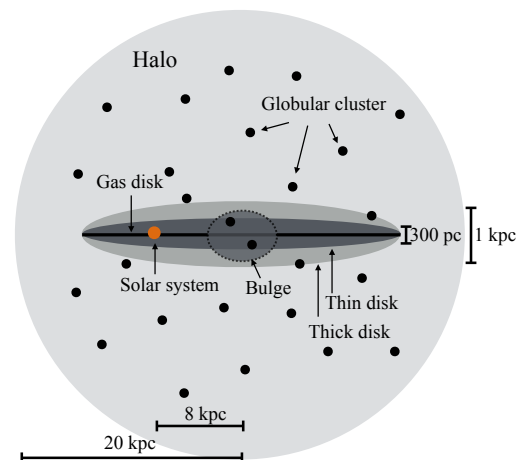


Figure 1.1. A schematic figure of our galaxy: edge-on view.

2 kpc. Random motions of stars are dominated in them, not rotational motion. The disk has two components: thin disk and thick disk (Gilmore and Reid, 1983). The thicknesses of these disk are 300 pc (thin disk) and 1 kpc (thick disk). Most of stars in the disk are in the thin disk, and all massive stars are in them. Most open clusters, which is a cluster of young massive stars, are observed in the thin disk. The radius of the disk is about 15 kpc, and our solar system locates at 8 kpc from the galaxy center.

1.1.2 Types of galaxies

There are many types of observed galaxies. Although it has been hard to classify galaxies precisely, this subsection will show roughly four groups: normal giant galaxies, dwarf galaxies, starburst galaxies, and active galaxies.

Hubble sequence

The Hubble sequence is a morphological classification scheme for giant galaxies invented by Hubble (1926). He classified a few hundred galaxies using optical images. Most galaxies (97-98 %) have rotational symmetry and a luminous core in the center; they are classified as regular galaxies. The others (2-3 %) are classified as irregular galaxies; these are hard to classify because of their complex morphologies. The regular galaxies are classified into four groups: ellipticals (the symbol E), lenticulars (the symbol S0), spirals (the symbol S), and barred spirals (the symbol SB) as shown in Figure 1.2.

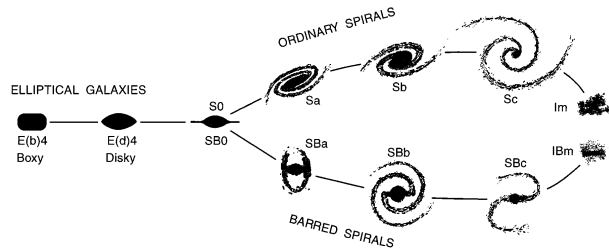


Figure 1.2. Hubble sequence: a morphological classification scheme for giant galaxies. This figure is adapted from Kormendy and Bender (1996).

Elliptical galaxies have smooth, featureless light distributions. They are composed primarily of old stars, and their star formation activities are passive. They are thought to form from interactions between galaxies, such as mergers and collisions. Elliptical galaxies have two types: Boxy and Disky. Boxy elliptical galaxies have a slow rotational speed and a high fraction of high temperature gas which emits X-ray radiation. Disky elliptical galaxies have a faster rotational speed.

Lenticular galaxies are rotational supported thin disk galaxies. They have no spiral structure. They also have almost no gas and dust, and they are composed primarily of old stars. Their star formation activities are passive.

Spiral galaxies are classified into three groups: Sa, Sb, and Sc. Compared to Sa, Sc galaxies have looser wound spiral arms, and they are clearly resolved into individual young stars and clusters and HII regions. Moreover, Sc galaxies have smaller, fainter bulge compared to the disk, and the percentages of the gas and dust mass to the stellar mass is larger. Barred spiral galaxies have the same three groups: SBa, SBb, and SBc.

M83, which is the modelled galaxy in our simulations, is an SBc nearby barred spiral galaxy.

Dwarf galaxy

A dwarf galaxy is a galaxy which has total mass less than $10^9 M_{\odot}$. They have similar morphologies, such as spirals, ellipticals, and irregulars.

Dwarf galaxies are one of the most important object for understanding galaxy formation and evolution in cosmology. In the Λ CDM model, the dwarf galaxies are building blocks for the giant galaxies. Numerical cosmological simulations based on the Λ CDM model predict that massive galaxies such as our galaxy should be surrounded by large numbers of dark matter dominated

satellite halos. However, the number of observed dwarf galaxies is orders of magnitude lower than expected from the cosmological simulations; a few tens of dwarf galaxies surrounding our galaxy are observed. This is well known as the missing satellites problem (Klypin et al., 1999; Moore et al., 1999; Simon and Geha, 2007).

Starburst galaxy

A starburst galaxy is a galaxy undergoing an exceptionally high rate of star formation. The typical star formation rate (= total stellar mass formed in 1 year) is 10-100 M_{\odot}/yr (cf. Milky-Way has 2-3 M_{\odot}/yr), and the gas consumption time is only 10-100 Myr. Starburst galaxies can be classified roughly into two groups: Luminous infrared galaxy (LIRG) and Blue compact galaxy (BCG).

A LIRG is a generally extremely dusty object. The ultraviolet radiation produced by the obscured star formation is absorbed by the dust and reradiated in the infrared spectrum. The triggering mechanism of the active star formation is under debate. One strong possibility is interactions between galaxies. The gas compression by a shock wave due to the galaxy's interactions or collisions can cause starburst in a short time. Most LIRGs show evidences of galaxy interactions, and about 50 % of high- z star-forming galaxies are the product of major mergers (Shapiro et al., 2008; Förster Schreiber et al., 2009; Tacconi et al., 2010; Daddi et al., 2010a). M82 is a good example of a starburst galaxy interacting with the nearby spiral M81. Incidentally, several spiral galaxies have starburst activities in the galactic center regions. One possibility of the starburst is also that during an interaction, it can easily transport gas into the galactic center. Second option is the transportation of gas through a bar structure toward the galactic center.

A BCG is a low mass, low metallicity, dust-free galaxy. It had been believed that they were young galaxies in the process of forming their first generation of stars. However, old stellar populations have been found in most BCGs. Formation process of BCGs is still debated.

Active galaxy

An active galaxy is a galaxy which hosts an active galactic nuclei (AGN) in the compact galactic central region. An AGN emits a huge amount of energy compared to the other regions of the galaxy; such emission has been observed in the radio, microwaves, infrared, optical, ultra-violet, X-ray and gamma ray wavebands. It is believed that the activity arises from an accretion of mass by a supermassive black hole in the galactic center, not from stellar activities. There are several types of galaxies hosting an AGN: Seyfert, Quasar, Radio galaxy, Blazar.

1.1.3 Barred spiral galaxy

In our work, we focus on a barred spiral galaxy because they have several different galactic structures, particularly bar and spiral arm structures. We can investigate the environmental dependence of star formation.

M83

We use the barred spiral galaxy M83 (NGC 5236) for modelling our galaxy simulations. M83 is a nearby galaxy located at the distance of 4.5Mpc from us (Thim et al., 2003); therefore, 1'' corresponds to 22 pc. This galaxy is one of the nearest, face-on galaxies which have prominent galactic structures: bar and spiral arms (see Figure 1.3)

This galaxy has ongoing star formation activities over the disk. In the bar and spiral regions, there are pronounced patterns of dust lanes and HII regions (Rumstay and Kaufman, 1983), large number of young massive clusters (Larsen and Richtler, 1999; Chandar et al., 2010; Bastian et al., 2012), and super nova remnants (Dopita et al., 2010; Blair et al., 2012). The central region of the galaxy hosts a bright starburst nucleus (Rieke, 1976; Bohlin et al., 1983; Turner



Figure 1.3. Image of the barred spiral galaxy M83. This image is based on data acquired with the 1.5-metre Danish telescope at ESO's La Silla Observatory in Chile, through three filters (B, V, R). Credit: ESO/IDA/Danish 1.5 m/R. Gendler, S. Guisard and C. Thone.

and Ho, 1994). The bar structure is likely responsible for feeding gas to the nuclear region (Lundgren et al., 2004a; Fathi et al., 2008). Offset ridges reside along the stellar bar, and those ridges are associated with shocked gas (Ondrechen, 1985).

There are many mapping observations in CO lines (Wiklind et al., 1990; Handa et al., 1990; Lord and Kenney, 1991; Kenney and Lord, 1991; Rand et al., 1999; Crosthwaite et al., 2002; Sakamoto et al., 2004; Lundgren et al., 2004b; Muraoka et al., 2009a,b; Hirota et al., 2014). Total mass of HI gas is $7.7 \times 10^9 M_{\odot}$ (Huchtmeier and Bohnenstengel, 1981). Total mass of H_2 gas is $3.2 \times 10^9 M_{\odot}$ (Crosthwaite et al., 2002) or $3.9 \times 10^9 M_{\odot}$ (Lundgren et al., 2004b).

Formation of spiral arm and bar structures

The formation process of spiral arm structures has been well debated, but consensus has not been reached yet. One of the most popular theories of spiral structure is the density wave theory of Lin and Shu (1964) (see also Bertin and Lin 1996). They formulated the spiral features not as a specific collection of stars, but rather a density wave that propagates azimuthally through the galactic disc. Spiral structures can be self-induced and maintained in a globally stable disk. This theory does not meet a winding dilemma, that is, if the stellar spiral is a material arm, the lifetime of the arm is shorter than that of its hosting galaxy (> 1 Gyr) because the galactic rotation curve is flat and then the spiral arm would wind up into nothing after a few galactic rotations. This is inconsistent with the fact that most nearby galaxies have spiral arms, indicating that the lifetime of the arm should be longer than 1 Gyr. Moreover, the long lived spirals can explain the observed offset between the stellar arm and dust lane; a supersonic gas flow into a spiral density wave experiences a shock as a result of the rapid deceleration, and this occurs before reaching the minima of the spiral potential (Fujimoto, 1968; Roberts, 1969).

Recent numerical simulations with a live (i.e. time-dependent) stellar disk, however, shows that stars and gas populate the spiral arms for the lifetime of the arm itself, rather than flowing into and out of the arm as in the density wave theory (Wada et al., 2011; Baba et al., 2013; Grand et al., 2013). The stellar arms are non-steady (i.e. transient and recurrent); they are wound and stretched by the galactic shear and merge with other arms. This is due to a swing amplification mechanism that reinforces density enhancement which seeds a wake in the disk (Goldreich and Lynden-Bell, 1965b; Julian and Toomre, 1966; Toomre, 1981; Baba et al., 2013). This non-steady stellar spiral makes the gas spirals associated with the stellar arms non-steady. The timescale of the change of the stellar spiral arm is 1-2 rotational periods at each radius

with and without central stellar bar structure (Wada et al., 2011; Baba, 2015).

Spiral structures can also be excited by tidal interactions with companion galaxies (Oh et al., 2008; Dobbs et al., 2010; Struck et al., 2011) and by the central stellar bars (Sellwood and Sparke 1988; Binney and Tremaine 2008, Section 6.4).

Many theoretical works, particularly in numerical simulations, have shown that stable bar structures are easily created (Ostriker and Peebles, 1973; Sparke and Sellwood, 1987; Combes et al., 1990; Baba et al., 2009; Shen et al., 2010; Grand et al., 2012). Bar structures are formed from a global instability of the galactic disk, known as bar instability, on the other hand, the spiral arm formation mentioned above comes from a local instability of the disk. In the gas disk, the criterion of the bar formation is $T/|W| > 0.2738$, where T is a rotational kinetic energy and W is a gravitational energy of the disk. In the stellar disk, the criterion of the bar formation is $T/|W| > 0.1286$. These are known as Ostriker-Peebles criterion (Ostriker and Peebles, 1973).

1.2 Star formation in galaxies

Understanding where and how gas is converted into stars in a galaxy is important for understanding galaxy's formation and evolution through each epoch of the universe: from the early universe after the formation of first stars (= population III stars), through the active star formation epoch around $z = 2$, and onto the current universe that includes the Milky Way and nearby galaxies. Which physical processes control the star formation in a galaxy is heavily debated; this is a mystery I would like to unlock.

1.2.1 Empirical relation of galactic-scale star formation

There are two important parameters for understanding the star formation activities in galaxies. First is the star formation rate (SFR), which is defined as a total stellar mass formed in 1 yr (SFR [M_{\odot}/yr]). This shows the total star formation activity in a galaxy or in a given area in a galaxy. Second is the star formation efficiency (SFE), which is defined as a ratio of the SFR and the total gas mass in a given region (SFE = SFR/ M_{gas} [yr^{-1}]). The inverse of the SFE is a depletion time scale of the gas in the region.

A relation between SFR and gas mass has been investigated well. Schmidt (1959) observed solar neighbour star forming clouds and suggested the existence of a power law correlation between the volume density of SFR (ρ_{SFR}) and the volume gas density (ρ_{gas}),

$$\rho_{\text{SFR}} \propto \rho_{\text{gas}}^n, \quad (1.1)$$

known as Schmidt law. Kennicutt (1989, 1998) observed 61 nearby disk and 36 nuclear starburst galaxies and found a power law correlation between the surface density of SFR (Σ_{SFR}) and the gas surface density (Σ_{gas}),

$$\Sigma_{\text{SFR}} \propto \Sigma_{\text{gas}}^{1.4}. \quad (1.2)$$

This correlation is known as the Kennicutt-Schmidt law, which has been the most widely used in the community (KS law, see Figure 1.4).

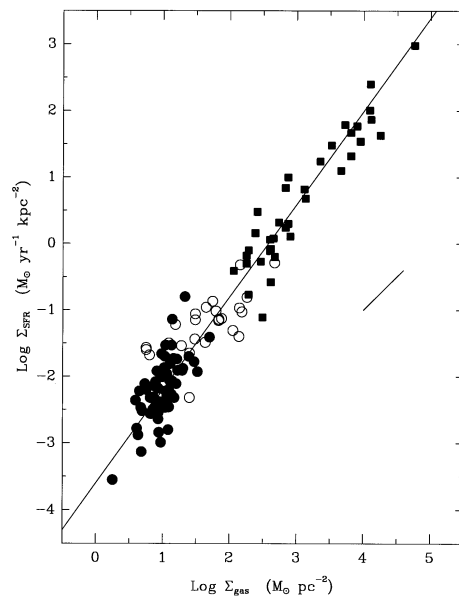


Figure 1.4. KS plot for the normal disk (filled circles) and starburst (squares) samples (taken from Kennicutt 1998, Figure 6). The gas mass includes both neutral (HI) and molecular (H_2) hydrogen. Open circles show the SFRs and gas densities for the centers of the normal disk galaxies. The line is a least-squares fit with index $N = 1.4$. The short, diagonal line shows the effect of changing the scaling radius by a factor of 2.

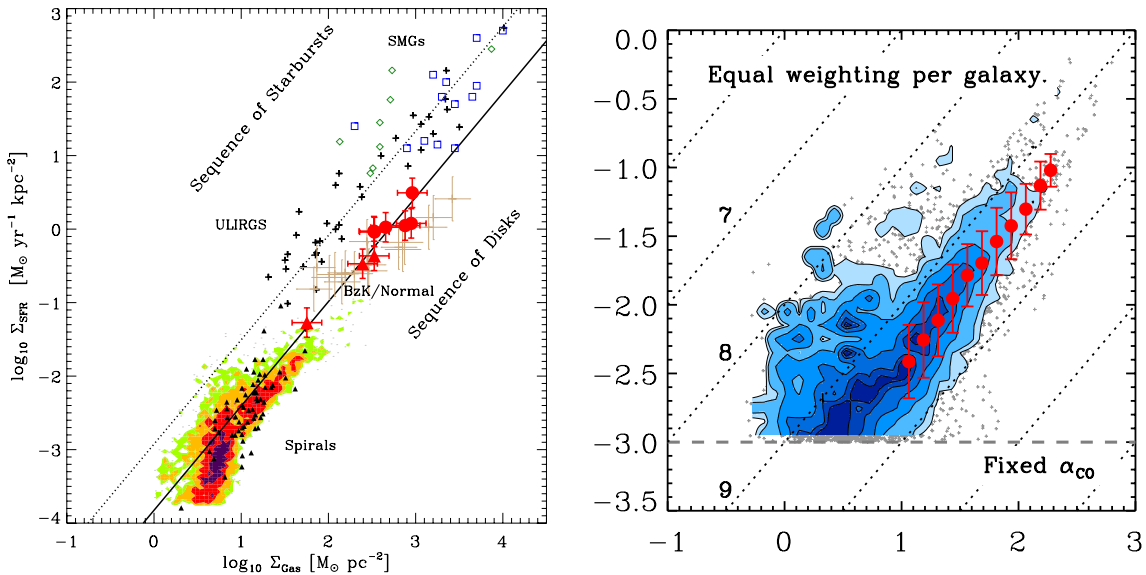


Figure 1.5. Left: KS plot for many types of galaxies (taken from Daddi et al. 2010b, Figure 2). x axis is the gas (atomic and molecular) surface density. Red filled circles and triangles are $z = 1.5$ normal (BzK-selected) galaxies (Daddi et al., 2010a) and $z \sim 0.5$ disks (Salmi et al., 2012), brown crosses are $z = 1 - 2.3$ normal galaxies (Tacconi et al., 2010). The empty squares are SMGs (Bouché et al. 2007, blue, Bothwell et al. 2009, light green) Crosses and filled triangles are (U)LIRGs and spiral galaxies from the sample of Kennicutt (1998). The shaded regions are THINGS spirals from Bigiel et al. (2008). The lower solid line is a fit to local spirals and $z = 1.5$ BzK galaxies (slope of the KS law is 1.42), and the upper dotted line is the same relation shifted up by 0.9 dex to fit local (U)LIRGs and SMGs. SFRs are derived from IR luminosities for the case of a Chabrier (2003) IMF. Right: KS plot for 30 nearby disk galaxies, not including high z starburst galaxies (taken from Leroy et al. 2013, Figure 1). Star formation rate surface density, Σ_{SFR} , estimated from $\text{H}\alpha + 24 \mu\text{m}$ emission, as a function of molecular gas surface density, Σ_{mol} , derived from CO (2-1) emission.

A popular physical approach is assuming that the SFR volume density (ρ_{SFR}) scales with gas volume density (ρ_{gas}) and local free-fall time (t_{ff}) as,

$$\rho_{\text{SFR}} = \epsilon_{\text{ff}} \frac{\rho_{\text{gas}}}{t_{\text{ff}}} \propto \rho_{\text{gas}}^{1.5} \quad \text{since} \quad t_{\text{ff}} = \sqrt{\frac{3\pi}{32G\rho_{\text{gas}}}} \propto \rho_{\text{gas}}^{-1/2}. \quad (1.3)$$

This formula is widely used for theoretical models of galaxy formation, either based on semianalytical realizations or numerical simulations (e.g. Cen and Ostriker 1992).

One of the most important points of this KS law is that only the gas density (or gas surface density) seems to control the galactic-scale star formation.

1.2.2 Environmental dependence of galactic-scale star formation

Recent high resolution observations have shown the star formation activity changing between galactic-scale environments; the SFEs have systematic variations larger than one order of magnitude between different galaxy types and different regions within a galaxy. This means that the gas density is not the only factor controlling the galactic-scale star formation. The details are as follows.

Left panel of Figure 1.5 shows the KS plot for different types of galaxies observed by Daddi et al. (2010b): nearby spiral galaxies, $z = 0.5 - 2.3$ normal disk galaxies, and high- z galaxies of submillimeter selected galaxies (SMGs) and IR-luminous galaxies (LIRGs/ULIRGs). This result is based on the current consensus for the CO luminosity to gas mass conversion factors. The data suggest the existence of two different star formation regimes: a long-lasting mode for disk galaxies (low SFEs) and a more rapid mode for starburst galaxies (high SFEs), the latter probably occurs during major mergers or in dense nuclear star-forming regions. Similar conclusions have been reached by Genzel et al. (2010).

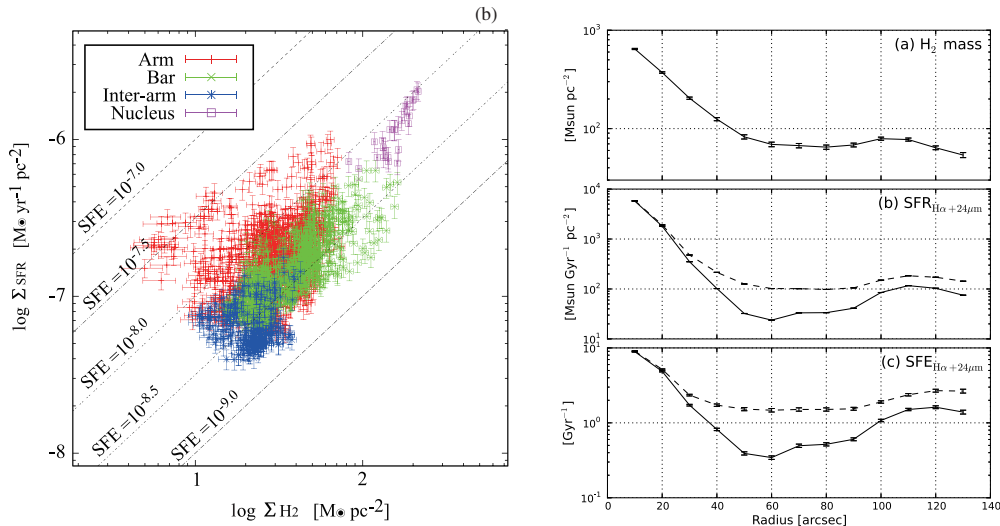


Figure 1.6. Left: KS plot for the barred spiral galaxy NGC 4303 at the native resolution of ~ 250 pc and the smoothing resolution of ~ 500 pc (taken from Momose et al. 2010, Figure 10). Right: Radial distributions of H_2 mass, SFR derived from $\text{H}_\alpha + 24 \mu\text{m}$, and SFE for the barre spiral galaxy M83 (taken from Hirota et al. 2014, Figure 15). Solid and dashed lines indicates the SFR with and without background subtraction.

Right panel of Figure 1.5 shows the KS plot for nearby disk galaxies, not including high z starburst galaxies, done by Leroy et al. (2013). The data is from the HERA CO-Line Extragalactic Survey (HERACLES, first maps in Leroy et al. 2009) used the IRAM 30 m telescope (supported by France, Germany, and Spain). The common spatial resolution of the survey is ~ 1 kpc sufficient to place many resolution elements across a typical disk galaxy. They found a first-order linear correspondence between Σ_{SFR} and Σ_{mol} (KS law) but also important second-order systematic variations about this scaling. This result suggests an environmental dependence of star formation activities between internal regions of a nearby disk galaxy.

Left panel of Figure 1.6 shows the KS plot for the barred spiral galaxy NGC 4303 at the smoothing resolution of ~ 500 pc observed by Momose et al. (2010). They quantified the differences in star formation activity between the galactic regions (nucleus, bar, spiral arm, and inter-arm) in the context of the KS law and found that the SFRs and SFEs are twice as high in the spiral arms than in the bar region. Right panel of Figure 1.6 also shows the difference of star formation activity (SFRs and SFEs) between the galactic regions in a barred galaxy observed by Hirota et al. (2014). They observed the nearby barred spiral galaxy M83, which is the modelling object for our galaxy simulations, and found the radial dependence of the SFR and SFE in the bar region: a low star formation activity in the end of the bar region and, on the other hand, a high activity in the middle of the region. Muraoka et al. (2007) also observed the M83 and found the higher SFEs in the nuclear starburst region than those in the disk regions.

Why does the star formation activity differ depending on the galactic structure's different environments? This question is key to understanding the galactic-scale star formation and has been the focus of my doctoral research. To understand this, it is important to investigate how the formation and evolution of giant molecular clouds (GMCs) is affected by the galactic structures. This is because the GMCs are the star formation spots in a galaxy.

1.3 Giant molecular clouds: stellar nurseries

Giant molecular clouds (GMC) are star formation spots in a galaxy, which makes them an important clue for understanding the galactic-scale star formation. They are formed from the cold phase of the interstellar medium (ISM), and the densest pockets within them are the birth place of stars. Properties (e.g. mass, size, and velocity dispersion) of the GMCs control

formation of these gravitationally unstable dense clumps and hence determine the rate of star formation in the galaxy.

1.3.1 Interstellar medium (ISM)

The interstellar medium (ISM) consists of gas and dust; main components of the gas are hydrogen (74 %) and helium (25 %), and those of the dust are C, Si, O, and Fe. The mass ratio of the gas and dust is 100:1.

Figure 1.7 shows multi-phase of the ISM; x axis is the density and y axis is the temperature of the ISM. HI is the neutral hydrogen gas; the typical density is 1 cm^{-3} , and the typical temperature is 100 K. GMCs mainly consist of molecular hydrogen and are confined self gravity; all stars are formed in them. The typical density is $10^2 - 10^5 \text{ cm}^{-3}$, and the typical temperature is $10 - 100 \text{ K}$. The mass ratio of the neutral and molecular hydrogen in the ISM is about 1:1. The HII region are ionised gas associated with newly formed massive stars. The density is higher than 10^2 cm^{-3} , and the typical temperature is 10^4 K . The typical size is $0.1 - 1 \text{ pc}$. Hot ionised gas is formed from supernovae explosions. The typical density is 10^{-2} cm^{-3} , and the typical temperature is 10^6 K , observed in X-ray wavelengths. The typical size of a supernova remnant extends to 100 pc where several massive stars explode in an open cluster or OB association. For example, several tens of supernovae occur together within several 10 Myrs in a star cluster whose number of stars are about a thousand. The multi supernovae form a large bubble in the ISM, a so called supershell. The supershell breaks through the galactic disk and supplies hot gas to the galactic halo. The cooling time of this hot diffuse gas is quite long, and they are widely distributed in the galactic halo.

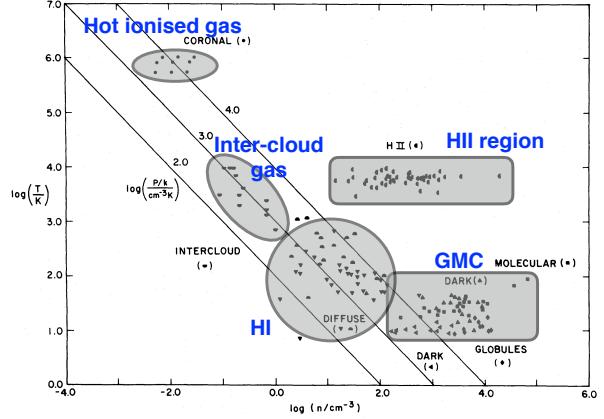


Figure 1.7. Phase diagram of the ISM (Myers, 1978). x axis is the density of the ISM and y axis is the temperature.

Cooling processes of the ISM

The ISM cools due to the following radiative processes (see also Dalgarno and McCray 1972 and Spitzer 1978):

1. Collisional excitation followed by radiation: at around 10^6 K , atomic cooling by Ne, Fe, and Si is dominant. Around 10^5 K , atomic cooling by O, C, and N is dominant and effective as seen in Figure 1.8. Around 10^4 K , atomic cooling by H is dominant ($\text{Ly-}\alpha$ emission). Below 10^4 K , radiative cooling by fine structures of such as CII, OII, OIII and a rotational/vibrational line emission of such as CO and H_2 molecule are dominant.

2. Free-free emission (bremsstrahlung) of electrons: in an ionised gas, electrons are decelerated when deflected by another charged particle, typically an ion. The decelerated electrons emit photons, and they lose their kinetic energy by radiation. This process is im-

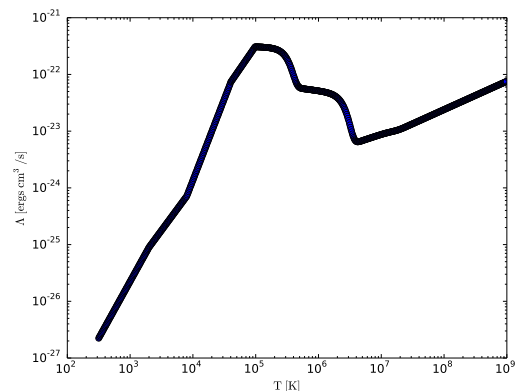


Figure 1.8. Cooling function, $\Lambda(T)$ [ergs $\text{cm}^3 \text{ s}^{-1}$], of the ISM taken from the analytical expression of Sarazin and White (1987) for solar metallicity down to 10^5 K , and continued to 300 K with rates provided by Rosen and Bregman (1995). We use this cooling function in our simulations.

portant for higher temperature ionised gas above 10^7 K. The cooling function ($\Lambda =$ Cooling rate [ergs $\text{cm}^{-3} \text{s}^{-1}$]/ n_{H}^2) is described as $\Lambda \propto T^{1/2}$.

3. Dust emission: the interstellar dust gains kinetic energy through collisions with the gas and radiates infrared emission.

4. Compton cooling (inverse Compton scattering): low energy photons (e.g. microwave and infrared) gains energy interacting with high energy electrons, and high energy radiation (e.g. X-ray and Gamma-ray) is emitted. This process is important in the high- z universe ($z > 6$) and not in the nearby universe because the cooling time is longer than the age of the universe.

Heating processes of the ISM

The ISM is heated up due to the following processes:

1. Photoionization. A photon interacts with an atom, stripping its electrons so that it becomes ionised (ionisation energy of atomic hydrogen is 13.6 eV). The excess energy which the photon had is transferred to the kinetic energy of the released electron, and then the bulk temperature of the ISM rises. This process is important in HII regions. The heating rate is given as $\Gamma = 8 \times 10^{-25} n_{\text{H}}^2$ [ergs $\text{cm}^{-3} \text{s}^{-1}$]. HI gas is easily ionised via this photoionization because it is optically thin to UV radiations although only the surface of the GMC is ionised because it is optically thick.

2. Cosmic ray ionisation. This is collisional ionisation of atomic hydrogen with cosmic ray particles (relativistic particles, most of them are protons). The heating rate is given as $\Gamma = 3.8 \times 10^{-29} n_{\text{H}}$ [ergs $\text{cm}^{-3} \text{s}^{-1}$]. Unlike UV radiation, the cosmic ray particles easily transmit into the GMC and ionise the inside gas (partially, not entirely).

3. Photoelectric heating effect on grain surface. The interstellar dust effectively absorbs UV radiation and emits an electron, so called a photoelectric effect. This process is important in HI gas. The heating rate is given as $\Gamma = 2 \times 10^{-25} n_{\text{H}}$ [ergs $\text{cm}^{-3} \text{s}^{-1}$].

4. Shock heating induced by spiral arms of galaxies and supernovae is also an important heating source of the ISM. Moreover, heat from H_2 formation on dust grains is also a heating source of the ISM.

Instabilities and Turbulence

Instabilities in the ISM, such as hydrodynamical instabilities and a thermal instability, and nonlinear growth are important physical processes for structure formation in the ISM.

1. The Rayleigh-Taylor instability is an instability at the interface between two fluids of different densities which occurs when the lighter fluid is pushing the denser fluid. For example, when denser water is put on lighter oil in a cup, instability occurs at the interface, and the two fluid mix. This is a basic process for mixing of the two different phase of the ISM.

2. The Kelvin-Helmholtz instability is an instability of an interface between two fluids of different velocities. An example is wind blowing over water; the instability manifests in waves on the water surface.

The balance between cooling and heating of the ISM determines multi thermally stable equilibrium states with different temperatures that can coexist in pressure balance (Figure 1.9, see also Field et al. 1969; Wolfire et al. 1995). This multi-phase of the ISM comes from the thermal

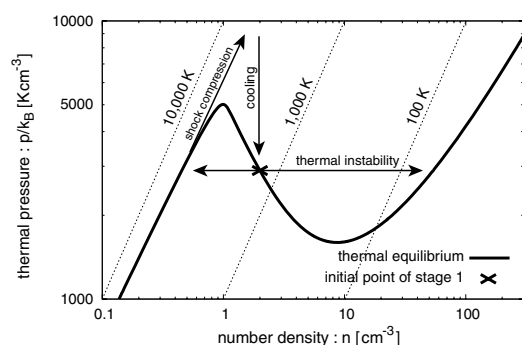


Figure 1.9. The thermal instability of the ISM (this figure is taken from Inoue et al. 2009). Stable warm and cold ISM exit with temperatures of the order 10^4 K and 10^2 K. The other temperature phase, for example 10^3 K, is in unstable due to runaway cooling/heating; gas cooling is dominant above the thermal equilibrium line, and on the other hand, gas heating is dominant below the line.

instability (Field, 1965); for example, in the unstable phase, a slight increase of the gas density causes gas cooling and further getting denser. Generally, the ISM has three thermally stable phases at 10^6 K, 10^4 K, and 10^2 K, so called three-phase model (McKee and Ostriker, 1977).

Because viscosity can be negligible in the ISM, there is no need to solve the Navier-Stokes equations. However, because of the small viscosity, the instabilities of the ISM can easily grow to nonlinear phase and, in the end, to a turbulence.

The Reynolds number (Re) is a dimensionless quantity that is used to help predict similar flow patterns in different fluid flow situations. For an incompressible fluid, the Re is defined as,

$$Re = \frac{\text{inertial force}}{\text{viscous force}} = \frac{\partial v / \partial t + (\mathbf{v} \cdot \nabla) \mathbf{v}}{\nu \Delta \mathbf{u}} \sim \frac{v^2 / L}{\nu v / L^2} = \frac{Lv}{\nu}, \quad (1.4)$$

where L is a characteristic linear dimension, v is the maximum velocity of the object relative to the fluid, and ν is the kinematic viscosity. $Re \gg 1$ means that the viscous term can be neglected. Generally, the ISM has quite a large Re (HI gas has the order of 10^3), so that a viscosity is negligible in the ISM as mentioned in the above paragraph.

After the formation of instabilities and their nonlinear growth, a whirlpool can emerge, that is described by vorticity ($\boldsymbol{\omega} \equiv \nabla \times \mathbf{v}$). A new instability would be formed at the surface of the whirlpool, and a smaller whirlpool would form. This process occurs again and again, and the kinetic energy of the initial whirlpool cascades to that of smaller one. Finally, the energy would change into the thermal motion of the small particles (atom and molecule) because the viscosity could not be negligible at the small scale, and the turbulence energy would disperse. The energy spectrum of the turbulence is described as,

$$E(k) \propto \epsilon^{2/3} k^{-5/3} \quad (k_0 < k < k_d), \quad (1.5)$$

where ϵ is a rate of energy dissipation and k is a wave number. This is a well known turbulence theory as the third Kolmogorov's hypothesis (Kolmogorov, 1941). The larger Re the fluid has, the wider wave number space ($k_0 < k < k_d$) the turbulence has. Note that this theory is for an incompressible fluid; the ISM is a compressible fluid. When the viscosity is quite small ($Re \rightarrow \infty$), the compressible fluid has energy spectrum as,

$$E(k) \propto k^{-2} \quad (\text{Tatsumi and Kida, 1973}). \quad (1.6)$$

Observation of HI gas in our galaxy has also shown that the energy spectrum is $E(k) \propto k^{-2}$ (Miville-Deschênes et al., 2003).

Numerical simulations of supersonic turbulence show that the dissipation timescale of the turbulence is an only one dynamical time (L/v) with/without a magnetic field (Mac Low et al., 1998). That is because the ISM is a compressible and supersonic fluid, and can easily lose turbulent energy through radiation due to shock waves. However, typical lifetime of the cloud is longer than the dynamical time. That means that some kind of mechanisms keep supplying turbulent energy into the ISM; the origin of this has been well debated, e.g. bipolar flows from a protoplanetary disk, expansions of HII regions, stellar winds from O stars, supernovae, self-gravity of the clouds, collisions of clouds, a galactic shear, and a spiral shock, etc (e.g. Norman and Ferrara 1996).

Though not mentioned above, the magnetic instabilities: Magneto-Rotational Instability (MRI) and Parker Instability are also important instabilities in the ISM seeding a supersonic turbulence.

1.3.2 Giant molecular cloud (GMC)

Giant molecular clouds (GMCs) are an aggregation of cold dense gas. Most gas in the GMC is in the molecular phase. The typical radius is $3 - 20$ pc, and the typical mass is $10^3 - 10^6 M_\odot$. The typical density is $10^2 - 10^5 \text{ cm}^{-3}$, and the typical temperature is $10 - 100$ K.

Larson's law: properties of the GMC

Observationally, there are three popular scaling relations between the velocity dispersion of the internal gas motion (σ), cloud size (L), and total mass (M) of the GMC (Larson, 1981).

1. The first Larson's law; velocity dispersion is proportional to cloud size,

$$\sigma(\text{km/s}) = 1.1 L(\text{pc})^{0.38}. \quad (1.7)$$

The larger size the GMC has, the larger velocity dispersion the internal gas has. Moreover, the typical values of σ (> 10 km/s) is higher than the sound velocity of the GMC ($c_s(10 \text{ K}) \sim 0.3$ km/s), so that the internal gas in the GMC is in supersonic turbulence. Solomon et al. (1987) showed that the power law index is 0.5, that is $\sigma \propto L^{0.5}$.

2. The second Larson's law; velocity dispersion is proportional to cloud mass,

$$\sigma(\text{km/s}) = 0.42 M(M_\odot)^{0.2}. \quad (1.8)$$

This relation shows that the GMCs are in virial equilibrium (i.e., gravitationally bound), with $2GM/\sigma^2 L \simeq 1$.

3. The third Larson's law; cloud size is inversely proportional to density,

$$\langle n(\text{H}_2) \rangle (\text{cm}^{-3}) = 3400 L(\text{pc})^{-1.1}. \quad (1.9)$$

Note that the density $\langle n \rangle$ is the average density of the GMC, calculated by dividing the total cloud's mass by its volume, not the peak density. This relation implies that the GMCs have approximately constant column densities Σ , since $\Sigma \sim nL \propto L^{-0.1}$. Solomon et al. (1987) also found that the surface density is approximately constant for all clouds with $\Sigma(\text{H}_2) = 170 M_\odot \text{pc}^{-2}$. Heyer et al. (2009) analysed the same samples but using ^{13}CO emission instead of ^{12}CO and found the same trend but a different value for $\Sigma(\text{H}_2) = 42 M_\odot \text{pc}^{-2}$ (see also Bolatto et al. 2008). Several theoretical studies using numerical simulations have questioned this third Larson's law (e.g., Ballesteros-Paredes et al. 2006). It has been suggested that this law is merely the result of the limited dynamic range of observations, and that in reality mass surface densities span at least two orders of magnitude. Recent observational work with a broader range of the data done by Lombardi et al. (2010) verified that the law of constant column density holds with a very small scatter and found that entire clouds are characterised by a universal structure, but single clouds and cores cannot be described by a constant column density.

Virial theorem

A hydrodynamical equation describing an equilibrium state of a spherical cloud, neglecting effects of magnetic field and rotation of the cloud, is

$$\frac{dP}{dr} = -\rho \frac{GM}{r^2}, \quad (1.10)$$

where $M = M(r)$ is a enclosed mass within a radius r . The integration of this equation from the centre of this sphere ($r = 0$) to the out edge ($r = R$) is,

$$\int_0^R 4\pi r^3 \frac{dP}{dr} dr = - \int_0^R 4\pi r^3 \rho \frac{GM}{r^2} dr. \quad (1.11)$$

The left term becomes,

$$\begin{aligned} (\text{Left}) &= 4\pi [r^3 P(r)]_0^R - 3 \int_0^R 4\pi r^2 P dr \\ &= 4\pi R^3 P_{\text{ex}} - 3 \int_0^R 4\pi r^2 P dr, \end{aligned} \quad (1.12)$$

where $P_{\text{ex}} = P(R)$ is an external gas pressure at interface of the cloud. The right term becomes,

$$\begin{aligned}
 (\text{Right}) &= -\frac{1}{2} \int_0^R \frac{G}{r} \frac{dM^2}{dr} dr \\
 &= -\frac{1}{2} \left[\frac{GM^2}{r} \right]_0^R - \frac{1}{2} \int_0^R \frac{GM^2}{r^2} dr \\
 &= -\frac{GM(R)^2}{2R} - \frac{1}{2} \int_0^R \frac{GM^2}{r^2} dr,
 \end{aligned} \tag{1.13}$$

assuming the gas distribution is homogeneous, not having radial dependence; $\rho = \text{const} \neq \rho(r)$. When $r < R$, a gravitational potential $\Phi(r)$ is,

$$\begin{aligned}
 \Phi(r) &= \int_{\infty}^r \frac{GM(s)}{s^2} ds \\
 &= \int_R^r \frac{GM(s)}{s^2} ds + \int_{\infty}^R \frac{GM(s)}{s^2} ds \\
 &= -\int_r^R \frac{GM(s)}{s^2} ds + \int_{\infty}^R \frac{GM(R)}{s^2} ds \\
 &= -\int_r^R \frac{GM(s)}{s^2} ds + GM(R) \left[-\frac{1}{s} \right]_{\infty}^R \\
 &= -\int_r^R \frac{GM(s)}{s^2} ds - \frac{GM(R)}{R}.
 \end{aligned} \tag{1.14}$$

Using this equation, a gravitational energy E_G is described as,

$$\begin{aligned}
 E_G &= \frac{1}{2} \int_0^R 4\pi r^2 \rho \Phi(r) dr \\
 &= -\frac{1}{2} \int_0^R 4\pi r^2 \rho \left[\int_r^R \frac{GM(s)}{s^2} ds \right] dr - \frac{1}{2} \int_0^R 4\pi r^2 \rho \left[\frac{GM(R)}{R} \right] dr \\
 &= -\frac{1}{2} \int_0^R \frac{GM(s)}{s^2} \left[\int_0^s 4\pi r^2 \rho dr \right] ds - \frac{1}{2} \frac{GM}{R} \int_0^R 4\pi r^2 \rho dr \\
 &= -\frac{1}{2} \int_0^R \frac{GM(s)^2}{s^2} ds - \frac{GM(R)^2}{2R} \quad (\text{= equation 1.13})
 \end{aligned} \tag{1.15}$$

The gravitational energy can easily be described in $E_G = -a \frac{GM^2}{R}$, where a is a constant factor, normally having around 1. Homogenous density sphere has $a = 3/5$. Using (1.12), (1.13) and (1.15), we get,

$$4\pi R^3 P_{\text{ex}} - 3 \int_0^R 4\pi r^2 P dr = E_G. \tag{1.16}$$

This is known as the virial theorem. Assuming an isothermal and homogenous cloud, the second term of the right side can change into,

$$3 \int_0^R 4\pi r^2 P dr = 3 \frac{P}{\rho} \int_0^R 4\pi r^2 \rho dr = 3 \frac{P}{\rho} M = 3 \frac{k_B T}{\mu m_H} M = 3c_s^2 M, \tag{1.17}$$

where c_s is a sound speed. Therefore, the virial theorem can be other form as,

$$4\pi R^3 P_{\text{ex}} = 3c_s^2 M - a \frac{GM^2}{R} \tag{1.18}$$

$$\Rightarrow P_{\text{ex}} = \frac{3c_s^2 M}{4\pi R^3} - \frac{aGM^2}{4\pi R^4}. \tag{1.19}$$

When cloud mass M is constant ($P_{\text{ex}} = P_{\text{ex}}(R)$), the external pressure P_{ex} has a peak,

$$P_{\text{ex,max}} = 0.68 \frac{c_s^8}{a^3 G^3 M^2} \quad \text{when } R = \frac{4aGM}{9c_s^2} \text{ and } M = \text{const.} \quad (1.20)$$

This means that there is a maximum of the external pressure ($P_{\text{ex,max}}$) that the spherical cloud whose mass is M can be in an equilibrium. Moreover, there is a maximum of the cloud mass M that the spherical cloud which is embedded in a medium with an external pressure P_{ex} can be in an equilibrium, as

$$M_{\text{max}} = 0.82 \frac{c_s^4}{a^{3/2} G^{3/2} P_{\text{ex}}^{1/2}} = 1.77 \frac{c_s^4}{G^{3/2} P_{\text{ex}}^{1/2}} \quad \text{when } R = \frac{4aGM}{9c_s^2} \text{ and } P_{\text{ex}} = \text{const,} \quad (1.21)$$

where $a = 3/5$ is used, which is a value for a homogenous density sphere. This critical mass also can be calculated directly through differentiating the equation of (1.19) assuming the external pressure P_{ex} is constant ($M = M(R)$). Ebert (1955) and Bonnor (1956) calculated this critical mass considering the internal gas density distribution (note that we have assumed a cloud which has a homogeneous profile, not considering a realistic internal gas density distribution in the above calculations). They showed,

$$M_{\text{BE}} = 1.18 \frac{c_s^4}{G^{3/2} P_{\text{ex}}^{1/2}}. \quad (1.22)$$

This is well known as the Bonnor-Ebert mass, which is the largest mass that an isothermal gas sphere embedded in a pressurized medium can have while still remaining in hydrostatic equilibrium. The difference between the form of (1.21) and (1.22) is only the coefficient.

When the external pressure is so small as to neglect the P_{ex} in equation (1.19),

$$M_{\text{virial}} = \frac{3c_s^2 R}{aG} = \frac{3k_B T R}{aG\mu m_H}, \quad (1.23)$$

where the M_{virial} is known as one of the virial mass. A half width of a distribution of the internal gas motion, Δv , can be described as $\Delta v^2 = 8(\ln 2)k_B T/(\mu m_H)$. Then the virial mass is,

$$M_{\text{virial}} [M_\odot] = \frac{3R(\Delta v)^2}{8(\ln 2)aG} = 210 (R [\text{pc}]) (\Delta v [\text{km/s}])^2. \quad (1.24)$$

This is used in observations to estimate the virial mass of the cloud or cloud core.

Gravitational collapse

To understand a gas collapse toward the star formation in a GMC, it is important to understand a basic figure of a gravitational collapse of a homogeneous sphere (uniform density distribution) neglecting a internal thermal gas pressure. When we set the initial mean density of a cloud is ρ_0 , and the initial radius is a , the equation of motion of the shell whose radius is $R(t)$ is,

$$\frac{d^2 R}{dt^2} = -\frac{GM(a)}{R^2} = -\frac{4\pi G \rho_0 a^3}{3R^2}. \quad (1.25)$$

Multiplying dR/dt by both side of this equation and integrating them give us,

$$\frac{dR}{dt} = -a \left[\frac{8\pi G \rho_0}{3} \left(\frac{a}{R} - 1 \right) \right]^{1/2}. \quad (1.26)$$

Setting $R/a = \cos^2 \beta$ and integrating of the above equation give us,

$$\beta + \frac{1}{2} \sin(2\beta) = t \left(\frac{8\pi G \rho_0}{3} \right)^{1/2}. \quad (1.27)$$

Every shell has the same β because the equation (1.27) has no a . Therefore, every shell reaches the centre of the sphere at the same time, when $\beta = \pi/2$. This time is defined as the free-fall time, t_{ff} :

$$t_{\text{ff}} = \left(\frac{3\pi}{32G\rho_0} \right)^{1/2} = 4 \text{ Myr} \left(\frac{10^2 \text{ cm}^{-3}}{n_{\text{H}+\text{H}_2}} \right)^{1/2}. \quad (1.28)$$

Even though the initial gas distribution is not uniform, we can use this formula if the cloud has spherical symmetry. In this case, we use a initial mean density of the cloud as the ρ_0 .

1.3.3 Formation and evolution of GMCs in galaxies

Observations of the Milky Way and nearby galaxies have revealed typical GMC properties: Milky Way (Larson, 1981; Solomon et al., 1987; Lada and Blitz, 1988; Dame et al., 2001; Heyer et al., 2009; Roman-Duval et al., 2010), LMC (Fukui et al., 1999, 2001, 2008; Mizuno et al., 2001b; Kawamura et al., 2009; Hughes et al., 2010), SMC (Mizuno et al., 2001a), M31 (Vogel et al., 1987; Lada et al., 1988; Wilson and Rudolph, 1993; Rosolowsky, 2007), M33 (Wilson and Scoville, 1990; Engargiola et al., 2003; Rosolowsky et al., 2003, 2007; Miura et al., 2012; Gratier et al., 2012), M51 (Koda et al., 2009, 2012; Meidt et al., 2013, 2015; Colombo et al., 2014), M64 (Rosolowsky and Blitz, 2005), M83 (Muraoka et al., 2009b), IC 10 (Wilson and Reid, 1991; Leroy et al., 2006), IC 342 (Hirota et al., 2011), NGC 4039 (Espada et al., 2012; Wei et al., 2012), NGC 6822 (Wilson, 1994), NGC 6946 (Rebolledo et al., 2012), Local Group (Blitz et al., 2007; Bolatto et al., 2008; Hughes et al., 2013; Donovan Meyer et al., 2013; Rebolledo et al., 2015). However, it is difficult within our own disc to assess the effects of global galactic structures, and extragalactic data are limited by resolution, which makes it hard to assemble large enough samples of GMCs to explore the dependence on internal galactic structures.

In theoretical works, it has become possible to investigate formation and evolution of individual GMC using hydrodynamical isolated galaxy simulations thanks to developments of super computer and effective algorithms (Dobbs et al., 2006, 2011b; Tasker and Tan, 2009; Renaud et al., 2013; Benincasa et al., 2013; Fujimoto et al., 2014a; Williamson et al., 2014; Tasker et al., 2015; Khoperskov et al., 2015). Tasker and Tan (2009) investigated GMC formation and evolution in a pure-disc (no grand design) galaxy and found that the cloud-cloud collision timescale is a small fraction, $\sim 1/5$, of the orbital time. Tasker et al. (2015) newly included a thermal stellar feedback effects and found the same conclusions as their previous pioneer work.

A few works have hinted at galactic structures affecting GMC distributions and properties. Dobbs et al. (2006) performed hydrodynamical simulations of a isolated spiral galaxy and found a dependence on GMC properties with grand design spiral arms, with clouds leaving the spiral arms to be sheared and form inter-arm feathering. Renaud et al. (2013) found more compact inter-arm spurs due to Kelvin-Helmholtz instabilities forming down the side of the spiral arms. There are a few observations which investigate the impact of galactic structures on GMCs. Koda et al. (2009) observed spiral galaxy M51 and found cloud assembling in the spiral arm, forming giant molecular associations and leaving smaller clouds into the inter-arm region. Meidt et al. (2013) and Colombo et al. (2014) observed the same galaxy and found that shearing flows and shocks driven by the spiral arms stabilise GMCs, and that changes the shape of the cloud mass distributions between the galactic environments. Hirota et al. (2011) observed the intermediate spiral galaxy IC342 and found GMCs that are associated with star forming regions are located downstream of the spiral arm and are more massive and closer to virial equilibrium.

1.4 Aim of this thesis

Understanding where and how gas is converted into stars in a galaxy is important for understanding a galaxy's formation and evolution through each epoch of the universe. Which physical

processes control the star formation in a galaxy is heavily debated; this is a mystery I would like to unlock.

Recent observations (high resolution, but not enough to resolve down to GMC scale yet) have shown the star formation activity changing between galactic-scale environments. Why does the star formation activity differ depending on the galactic structure's different environments? To understand this, it is important to investigate how the formation and evolution of GMCs is affected by the galactic structures. This is because the GMCs are the star formation spots in a galaxy; they are formed from the cold phase of the ISM, and their densest pocket are the birth place of stars.

We are now at a stage where it is possible to investigate the giant molecular clouds (GMC) and star formation, while also taking global galactic dynamics into account. We can investigate the formation and evolution of individual GMCs using hydrodynamical isolated galaxy simulations with a self-consistent multiphase interstellar medium (ISM) thanks to developments of super-computer and effective algorithms.

We performed three-dimensional hydrodynamical simulations of a barred spiral galaxy, and investigated environmental features of formation and evolution of the GMCs. These works consists of three parts. Aims of each part are;

1. We aimed to explore the effects of galactic structures (bar and spiral arms) on GMC formation and evolution in a barred spiral galaxy.
2. We aimed to clarify the physical process that causes different SFEs in a barred galaxy, focusing on triggered star formation by cloud-cloud collisions.
3. We aimed to investigate the impact of both galactic structures and supernova feedback on the ISM, GMCs, and star formation.

Chapter 2

Environmental dependence of GMCs in a barred spiral galaxy

We investigate the impact of galactic environment on the properties of simulated giant molecular clouds (GMCs) formed in a M83-type barred spiral galaxy. Our simulation uses a rotating stellar potential to create the grand design features and resolves down to 1.5 pc. From the comparison of clouds found in the bar, spiral and disc regions, we find that the typical GMC is environment independent, with a mass of $5 \times 10^5 M_{\odot}$ and radius 11 pc. However, the fraction of clouds in the property distribution tails varies between regions, with larger, more massive clouds with a higher velocity dispersion being found in greatest proportions in the bar, spiral and then disc. The bar clouds also show a bimodality that is not reflected in the spiral and disc clouds except in the surface density, where all three regions show two distinct peaks. We identify these features as being due to the relative proportion of three cloud types, classified via the mass-radius scaling relation, which we label *A*, *B* and *C*. *Type A* clouds have the typical values listed above and form the largest fraction in each region. *Type B* clouds are massive giant molecular associations (GMAs) while *Type C* clouds are unbound, transient clouds that form in dense filaments and tidal tails. The fraction of each clouds type depends on the cloud-cloud interactions, which cause mergers to build up the GMA *Type Bs* and tidal features in which the *Type C* clouds are formed. The number of cloud interactions is greatest in the bar, followed by the spiral, causing a higher fraction of both cloud types compared to the disc. While the cloud types also exist in lower resolution simulations, their identification becomes more challenging as they are not well separated populations on the mass-radius relation or distribution plots. Finally, we compare the results for three star formation models to estimate the star formation rate and efficiency in each galactic region.

2.1 Introduction

At first glance, star formation appears to be a localised process. The coldest gas in the galactic interstellar medium (ISM) clumps into turbulent aggregations known as the giant molecular clouds (GMCs). These stellar nurseries are on average, three orders of magnitude smaller than the galactic radii and the pockets within them that collapse to form stars are another order of magnitude smaller still. Additionally, GMC properties have been observed to be remarkably similar across different galaxies, which might suggest a disregard for the structure of the galactic host (Blitz et al., 2007; Bolatto et al., 2008; Heyer et al., 2009; Donovan Meyer et al., 2013).

Yet, there is still more evidence that star formation is far from being unaware of its global environment. Observations indicate an empirical relation that relates the galaxy's gas surface density (Σ_{gas}) and its star formation rate surface density (Σ_{SFR}) by a simple power law (Schmidt, 1959; Kennicutt, 1989, 1998; Wong and Blitz, 2002; Kennicutt et al., 2007; Bigiel et al., 2008; Leroy et al., 2008; Schruba et al., 2011):

$$\Sigma_{\text{SFR}} \propto \Sigma_{\text{gas}}^N \quad (2.1)$$

where the measurements of the power index, N , vary between 1 and 2. Generally referred to as the Kennicutt-Schmidt Relation, this link between the gas distribution in a galaxy and its star formation holds on both local and global scales. Moreover, recent work has shown that systematic variations exist in the relation and that the star formation activity may also be sensitive to global structural variations such as galaxy type (Daddi et al., 2010b; Leroy et al., 2013), conditions in the galactic central region (Oka et al., 2001) and the grand design (Sheth et al., 2002; Momose et al., 2010). Notably, this is distinct from material simply being gathered to produce a higher star formation rate, since then both the gas density and star formation rate density would rise in unison and not produce a variation in the Kennicutt-Schmidt relation. However, observations of the barred galaxy NGC 4303 by Momose et al. (2010) revealed a different star formation efficiency in the spiral arms and bar region of the disc, even in locations where the gas surface density is comparable.

If star formation truly does care about its large-scale environment then this should be reflected in the properties of the GMCs, the nurseries whose conditions determine whether a star can form. Within the Milky Way, the properties of GMCs have been measured to high precision (Larson, 1981; Solomon et al., 1987; Heyer et al., 2009; Roman-Duval et al., 2010), yet it is difficult from within our own disc to assess the impact of global structure. A more likely source of information comes from the growing catalogue of nearby galaxy GMC properties, many of which elude to environmentally driven differences between the populations in different galaxies (Hughes et al., 2013). However, extragalactic data is limited by resolution, making it hard to assemble large enough samples of GMC properties to explore the dependence on internal galaxy structure (a deficit that ALMA will tackle). The results we do have from such surveys strongly indicate that structure plays a key role in star formation. In the spiral arms of M51, observations by Koda et al. (2009) find evidence for giant molecular associations (GMAs) which later fragment into smaller GMCs in the interarm region. These GMAs have a significantly higher surface density, while having the same estimated volume density, as a typical galactic GMC, suggesting they are a distinct group of objects and not simply an agglomeration of overlapping clouds. In the same galaxy, Meidt et al. (2013) observed that sheering flows and shocks driven by spiral structures can stabilise GMCs that would otherwise collapse to form stars, changing the dependence between the star formation rate and gas surface density in such environments. It is clear, therefore, that understanding environment effects on GMC properties is key to understanding star formation itself.

On the theoretical side, a dependence on GMC properties with galactic structure has been found by Dobbs and Bonnell (2006) who saw a similar result to Koda et al. (2009), with clouds leaving the spiral arms to be sheared and form interarm feathering. More compact interarm spurs were found by Renaud et al. (2013), due to Kelvin-Helmholtz instabilities forming down the side of the spiral arms. Renaud et al. (2013) also found that the elongated gas structures in their spiral arms dictated the spacing of their GMCs, with fragmentation occurring at regularly spaced intervals. In the transient spiral galaxy models of Wada et al. (2011), gas arms can gather material to form a GMA, but then can themselves disperse the arm and their own structure. The two-dimensional simulations of M83 by Nimori et al. (2013) found that GMCs forming in the bar region tended to be less bound than those in the spiral arms. Their findings were consistent with observations that the velocity dispersion of molecular gas in the bar region both in M83 and in Maffei 2 is high (Lundgren et al., 2004a; Sorai et al., 2012), raising the value of the virial parameter.

One possible reason for Nimori et al. (2013)'s findings is the increased likelihood of collisions between GMCs in regions of high gas density. Such interactions can either build the cloud via mergers, deepening its potential well and central density to boost star formation or by triggering a shock at the collisional interface to produce stars. The latter mechanism has been previously suggested as a way to unite the local star formation process with the globally

observed Kennicutt-Schmidt relation (Tan, 2000; Tasker and Tan, 2009) and also as a way to create massive stars (Furukawa et al., 2009; Ohama et al., 2010; Habe and Ohta, 1992). Therefore, the structure of the disc has both the potential to change the properties of the GMCs and increase their interactions to trigger star formation.

In this chapter, we will focus on the effect of a grand design bar and spiral on the formation and evolution of the GMCs. In section §2, we present our model of the barred galaxy, M83 and discuss the details of the three-dimensional hydrodynamical simulation. Section §3 details our results, discussing first the global evolution of the disc and moving on to exploring the cloud properties and estimated star formation rates. In section §4, we consider the effect of resolution and the way in which GMCs are identified. Section §5 presents our conclusions.

2.2 Numerical methods

2.2.1 The code

The simulations presented in this chapter were run using *Enzo*: a three-dimensional adaptive mesh refinement (AMR) hydrodynamics code (Bryan et al., 2014). *Enzo* has previously been used to model galactic discs where it successfully produced a self-consistent atomic multiphase ISM, consisting of a wide range of densities and temperatures (Tasker and Bryan, 2006, 2008; Tasker and Tan, 2009; Tasker, 2011; Benincasa et al., 2013).

We used a three-dimensional box of side 50 kpc with a root grid of 128^3 cells and 8 levels of refinement, giving a limiting resolution (smallest cell size) of about 1.5 pc. Cells were refined whenever the mass included in the cell exceeded $1000M_{\odot}$, or whenever the Jeans' Length covered less than four cells. This latter condition is suggested by Truelove et al. (1997) as the minimum resolution required to avoid artificial fragmentation.

The evolution of the gas in *Enzo* was performed using a three-dimensional version of the *Zeus* hydrodynamics algorithm (Stone and Norman, 1992). *Zeus* uses an artificial viscosity as a shock-capturing technique with the variable associated with this, the quadratic artificial viscosity, set to the default value of 2.0.

The gas was self-gravitating and allowed to cool radiatively down to 300 K. The radiative cooling used rates from the analytical expression of Sarazin and White (1987) for solar metallicity down to 10^4 K, and continued to 300 K with rates provided by Rosen and Bregman (1995). This allowed the gas to cool to temperatures at the upper end of the atomic cold neutral medium (Wolfire et al., 2003). Actual GMCs have temperatures of about 10 K, an order of magnitude below our minimum radiative cooling temperature. However, we lacked the resolution to sufficiently resolve the full turbulent structure of our smaller clouds, nor did we include pressure from magnetic fields. This temperature floor therefore imposed a minimum sound speed of 1.8 km/s to crudely allow for these effects. In fact, the velocity dispersion within our clouds was typically higher than this by about a factor of three, implying that the floor was not having a significant impact on our cloud properties.

To prevent unresolved collapse at the finest resolution level, a pressure floor was implemented that injected energy to halt the collapse once the Jeans length became smaller than four cells. Gas in this regime followed a $\gamma = 2$ polytrope, $P \propto \rho^{\gamma}$. In order to study the evolution of the gas clouds alone, there was no star formation or stellar feedback in this simulation.

2.2.2 The structure of the galactic disc

Our galaxy was modelled on the barred spiral galaxy, M83, with the gas distribution and stellar potential taken from observational results (see below). At 4.5 Mpc away, M83 is a nearby type SABC galaxy and has been observed at various wavelengths to measure its atomic (Huchtmeier and Bohnenstengel, 1981) and molecular gas (Lundgren et al., 2004b,a; Sakamoto et al., 2004; Muraoka et al., 2007) as well as optical emission lines (Dopita et al., 2010) and X-ray (Soria

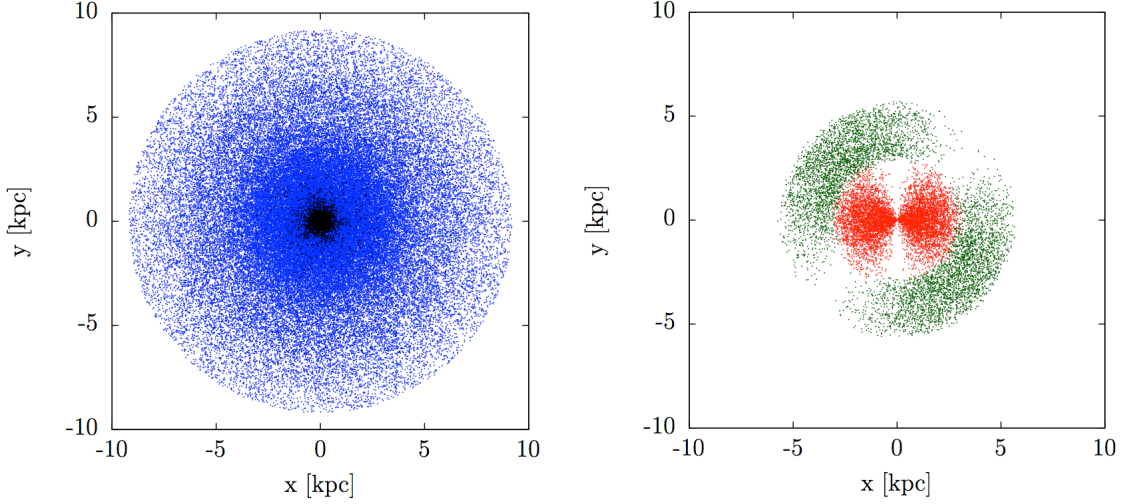


Figure 2.1. The stellar component of the galactic potential. Left panel shows the axisymmetric star particle distribution, where blue dots denote disc particles and black form the bulge. Right panel shows the non-axisymmetric star particle distribution (red dots are the bar particles and green are the spiral arms) which are rotated at a constant pattern speed.

and Wu, 2003). Its GMC properties are also being observed by ALMA in Cycle 0 and Cycle 1 (Hirota et al., in prep.).

Initial gas distribution

For the galaxy's radial gas distribution, we assumed an initial exponential density profile with a radial scale length of 2265 pc, based on the observations of Lundgren et al. (2004b). The initial vertical distribution was assumed to be proportional to $\text{sech}^2(z/z_h)$ with a vertical scale height of $z_h = 100$ pc. The total gas mass in the simulation was taken again from the observations of Lundgren et al. (2004b), where the H_2 gas mass was recorded as $3.9 \times 10^9 M_\odot$. This gave an initial gas distribution:

$$\rho_{\text{gas}}(r, z) = 0.67 \exp\left(-\frac{r}{2265\text{pc}}\right) \text{sech}^2\left(\frac{z}{100\text{pc}}\right) M_\odot/\text{pc}^3 \quad (2.2)$$

The gas was set in circular motion as calculated via $V_{\text{cir}}(r) = (GM_{\text{tot}}/r)^{1/2}$, where M_{tot} is the enclosed mass of stars, dark matter and gas within the radius r .

Stellar potential

We used 10^5 fixed-motion star particles to create a stellar potential model in keeping with the observed global characteristics of the stellar distribution in M83. This model was from the work of Hirota et al. (2009), who analysed the 2Mass K-band image of M83 (Jarrett et al., 2003). The stellar density, consisting of the disc, bulge, bar and spiral arms was given by:

$$\begin{aligned} \rho_{\text{star}}(r, \theta, z) &= \Sigma(r, \theta)h(z) \\ &= \{\Sigma_{\text{disc}}(r) + \Sigma_{\text{bulge}}(r) + \\ &\quad \Sigma_{\text{bar}}(r) \cos(2\theta) + \Sigma_{\text{spiral}}(r) \sin(2\theta)\}h(z), \end{aligned} \quad (2.3)$$

where $\Sigma_i(r)$ is the radial distribution of each component and $h(z)$ is the vertical distribution. Each of these were given by:

$$\Sigma_{\text{disc}}(r) = 20 \exp(-r/2231\text{pc}), \quad (2.4)$$

(0 pc \leq r \leq 9200 pc)

$$\Sigma_{\text{bulge}}(r) = \frac{1000}{\{1 + (r/138\text{pc})^2\}^{1.5}}, \quad (2.5)$$

(0 pc \leq r \leq 9200 pc)

$$\Sigma_{\text{bar}}(r) = \frac{3}{100}(1150\text{pc} - r) + 2.7, \quad (2.6)$$

(0 pc \leq r \leq 3220 pc)

$$\Sigma_{\text{spiral}}(r) = -\frac{0.7}{900}(r - 3450\text{pc})^2 + 0.7$$

$$-\frac{0.6}{2500}(r - 3450\text{pc})(r - 5750\text{pc}). \quad (2.7)$$

(2760 pc \leq r \leq 5750 pc)

In this model, Hirota et al. (2009) assumed that the mass to light ratio was constant between bulge and outer disc region. However, M83 has a starburst at the nucleus and so the actual total stellar mass of the nucleus has to be less than what was assumed. Owing to this, we decreased the influence of the bulge potential by 35% by distributing the star particles between Equations 2.4 - 2.7 in a 2:0.7:2:2 ratio.

We assumed the vertical stellar distribution $h(z)$ was:

$$h(z) = \frac{1}{892} \text{sech}^2\left(\frac{z}{446\text{pc}}\right) \quad (-4600\text{ pc} \leq z \leq 4600\text{ pc})$$

$$= \frac{1}{892} \left\{ \frac{2}{\exp(z/446\text{pc}) + \exp(-z/446\text{pc})} \right\}^2. \quad (2.8)$$

Figure 2.1 shows the resulting distribution of the star particles. The left panel shows the axisymmetric star particles distribution where blue dots mark disc particles and black show the bulge. The right panel shows the non-axisymmetric star particle distribution (where red dots are the bar particles and green dots denote spiral arms) which is rotated at 54 km/s/kpc, the estimated pattern speed for M83 (Hirota et al., 2009).

Each star particle has a mass of $5.0 \times 10^5 M_{\odot}$, giving a total stellar mass of $M_* = 5.0 \times 10^{10} M_{\odot}$, in agreement with observational results (see section 2.2.2).

To remove the discreteness effects of the star particles, we smoothed the particles' gravitational contribution by adding the mass onto the grid at AMR level 4, with a cell size of 50 pc.

Dark matter potential

In addition to the stellar potential, the galaxy sits in a static dark matter halo with an NFW profile (Navarro et al., 1997). The halo concentration parameter was set to $c = 10$, while the virial mass (within which the density is 200 times the cosmological critical value), $M_{200} = 1.0 \times 10^{10} M_{\odot}$, a value obtained by comparison with the observational results (see section 2.2.2).

Stellar and dark matter mass ratio

The stellar and dark matter masses of $M_* = 5.0 \times 10^{10} M_{\odot}$ and $M_{200} = 1.0 \times 10^{10} M_{\odot}$, were selected via comparisons between our model's rotation curve and that from the observational

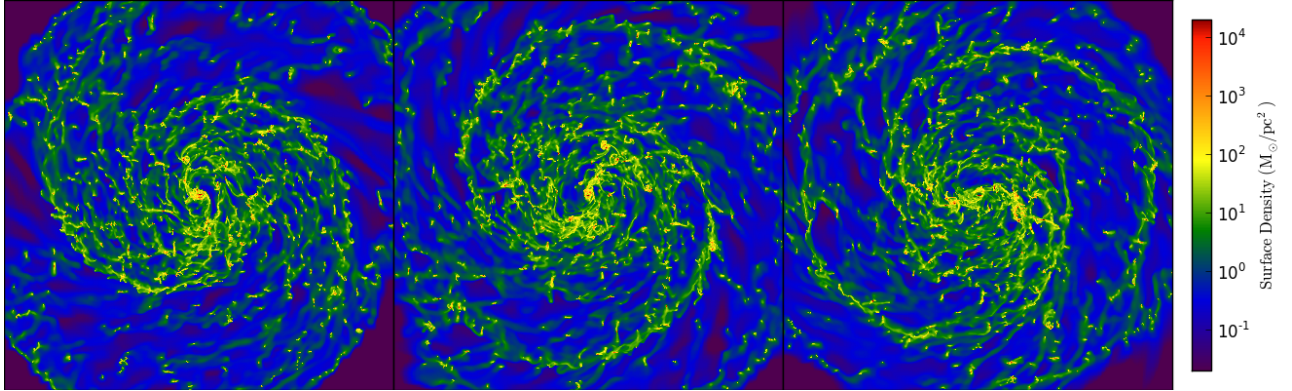


Figure 2.2. Evolution of the galactic disc. Images show the surface gas density at times, $t = 200$, 240 , and 280 Myr. Each image is 15 kpc across.

results from M83 (Lundgren et al., 2004a). We also compared and matched the size of the bar obtained from the M83 $^{12}\text{CO}(J=1-0)$ observations (Lundgren et al., 2004b) with the size of the bar structure formed in the simulation at 240 Myr. In both cases, the position of the bar-end from the galactic centre was approximately 2.3 kpc. Within the radius of the galaxy disc, the stellar mass dominated over the dark matter to ensure a grand design spiral.

2.2.3 Cloud definition and tracking

The giant molecular clouds in our simulation were identified as coherent structures contained within contours at the threshold density of $n_{\text{H},c} = 100 \text{ cm}^{-3}$, similar to the observed mean volume densities of typical galactic GMCs. Note that since the formation of molecules was not being followed in our simulation, the gas is purely atomic. However, at the threshold density, it is reasonable to assume the cloud would consist of both a molecular core and atomic envelope. We refer to this method as the ‘*contour method*’ for cloud identification.

We also used an additional method for defining GMCs that builds clouds around density local maxima (Tasker and Tan, 2009). Here, peaks are found in the baryon density field that have $n_{\text{H}} \geq n_{\text{H},c} = 100 \text{ cm}^{-3}$. Neighbouring cells are then recursively searched and assigned to the cloud if they also have densities $n_{\text{H}} \geq 100 \text{ cm}^{-3}$. Density peaks further 20 pc apart are identified as separate clouds. We refer to this method as the ‘*peak method*’.

The main difference between these two methods is that in the second case, multiple clouds may exist within the same continuous density structure if it contains more than one well-separated peak.

In this chapter, we mainly focus on the results of the *contour method* due to its ability to identify large bodies that (visually) appear to be a single entity. This allows us to assess more easily the difference the environment was having on the cloud properties. Notably, however, the overall results from these two methods are very similar. We discuss this in a quantitative way in section 2.4.2.

To follow the evolution of the clouds, simulation outputs were analysed every 1 Myr and the clouds were mapped between outputs with a tag number assigned to each cloud. The algorithm of this cloud tracking is described in Tasker and Tan (2009). A merger is said to have happened when a single cloud is at the predicted position for two other clouds after 1 Myr of evolution.

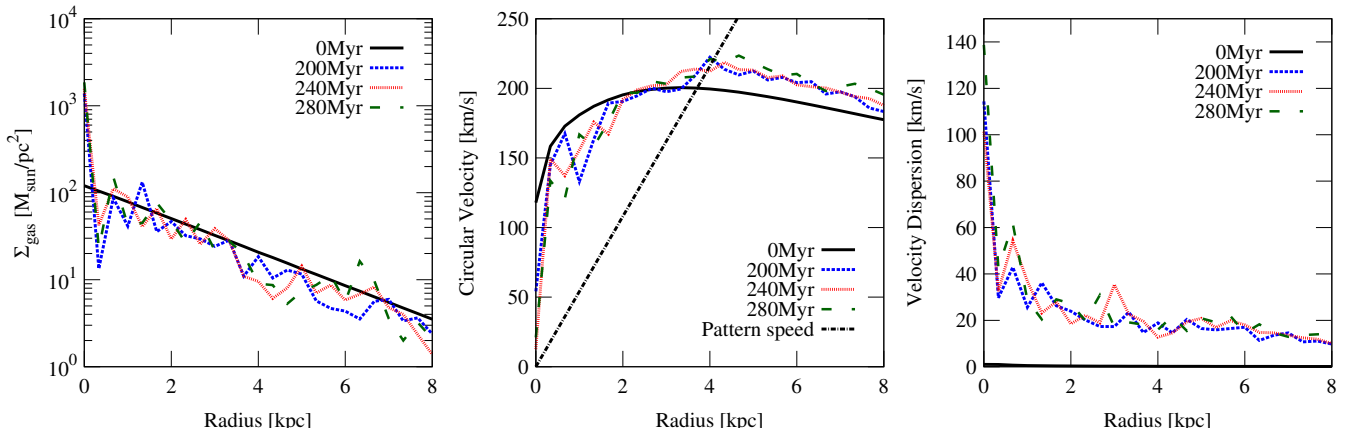


Figure 2.3. Azimuthally averaged (bin size 333 pc) radial gas profiles for the galactic disc at $t = 0, 200, 240$ and 280 Myr. From left to right: (1) gas surface density, $\Sigma_{\text{gas}} = \int_{-1\text{kpc}}^{+1\text{kpc}} \rho(z) dz$, (2) gas circular velocity (mass-weighted average over $-1\text{kpc} < z < 1\text{kpc}$) and (3) 1D gas velocity dispersion (also mass-weighted average over $-1\text{kpc} < z < 1\text{kpc}$).

2.3 Results

2.3.1 Global structure and disc evolution

In the initial stages of the simulation, the gas profile is smoothly exponential as described in section 2.2.2. As the simulation begins and the gas feels the impact of the stellar potential, two shock waves are formed at the point of co-rotation between the stellar potential’s pattern speed and the gas circular velocity. As they move in opposite directions through the disc, the gas falls into the grand design pattern. Self-gravity then begins to act, fragmenting the gas into knots and filaments. After 120 Myr (one pattern rotation period), the gas is fully fragmented, and between 200 Myr and 280 Myr, the galactic disc settles into a quasi-equilibrium with no large structural change.

The surface density of the inner 15 kpc of the galactic disc is shown in Figure 2.2 at three different times after the main fragmentation: $t = 200, 240$ and 280 Myr. Given the period of rotation for the non-antisymmetric stellar potential (pattern speed) is about 120 Myr, the figure shows approximately 2/3rd of a pattern rotation. The gas circular velocity gives a orbital period of about 240 Myr (our middle panel) at the disc’s outer edge, 8 kpc.

The grand design of the bar and spiral arms can be clearly seen in each panel of Figure 2.2. These global galactic structures are consistent with the $^{12}\text{CO}(J=1-0)$ image of M83 (Lundgren et al., 2004b), with the bar-end at $r \sim 2.3$ kpc. The bar and spiral arms rotate counter-clockwise in pace with the non-axisymmetric stellar potential.

We can see the formation of clouds as dense knots in the surface density field. These clouds are seen not only in the bar and spiral arms but also in the inter-arm region and outer disc. This is in keeping with observations, where clouds are observed both within the grand design’s main features and also the inter-arm regions (Koda et al., 2009). The properties of the clouds during this quasi-equilibrium stage are the focus of this chapter.

The azimuthally averaged radial profiles for the galaxy disc are shown in Figure 2.3 at four different simulation times, $t = 0, 200, 240$ and 280 Myr. Between 200 Myr and 280 Myr (our main analysis time period), the disc properties are settled and show little evolution in agreement with what is seen visually in Figure 2.2.

The left-most panel of Figure 2.3 plots the gas surface density, averaged over a height of $-1\text{kpc} < z < 1\text{kpc}$, containing the full extent of the disc’s vertical height. Small fluctuations are seen in the surface gas density as the gas fragments interact and are stirred by the stellar potential, but the profile shape remains unchanged. At the very centre of the disc, the surface

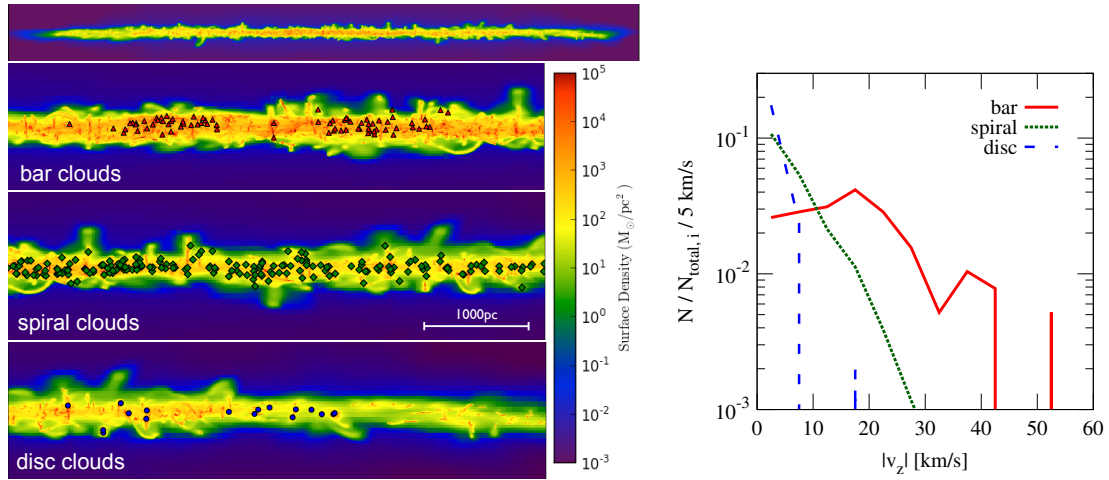


Figure 2.4. Galactic disc vertical gas properties. Left panel shows the surface density of edge-on galactic disc with the cloud positions marked by the red, green and blue symbols (bar, spiral and disc region, respectively). Right panel shows the normalised distributions of the vertical velocity of the clouds in each region at 240 Myr.

density does increase with time due to infall both from resolution (it is impossible to maintain perfect circular motion on a Cartesian grid at very small radii) and gas motion induced by the bar’s potential. In M83, this bar instability causes a starburst in the central region at radius $r < 300\text{pc}$ (Harris et al., 2001). If we allowed star formation and stellar feedback in our model, we would expect the gas ejection from such a burst to suppress this concentration of central gas. Since we do not include this process in our model, we ignore the galaxy’s central region ($r < 600\text{pc}$) in our analysis of the cloud properties.

The middle panel of Figure 2.3 shows the radial profile of the mean circular velocity of the gas. This is calculated as a mass-weighted average over $-1\text{kpc} < z < 1\text{kpc}$. Here, the effect of the rotating stellar potential is clearly visible, with the gas deviating from its initial orbit away from the point of co-rotation between the pattern and initial gas orbital speed at $r \sim 3.5$ kpc. Beyond this point, the stellar potential rotates faster than the initial gas circular speed, driving the gas to a faster orbit. The circular velocity here is approximately 200 km/s, agreeing with the rotation curve of M83 (Lundgren et al., 2004a). Within 3.5 kpc, the gas motion is dominated by the bar which, inside the bar ends at $r = 2.3$ kpc, forces the gas to flow along elliptical orbits. This produces an average velocity lower than the initial conditions, since the motion is not truly circular any more.

The final right-most panel of Figure 2.3, shows the one-dimensional velocity dispersion as defined by $\sigma_{1D} = \sqrt{(\vec{v} - \vec{v}_{\text{cir}})^2/3}$, where \vec{v} is the velocity of the gas and \vec{v}_{cir} is its circular velocity at that point. It is also calculated as a mass-weighted average over $-1\text{kpc} < z < 1\text{kpc}$. With the gas motion initially set to follow a circular orbit, the dispersion at $t = 0$ is zero. As the gas falls into the stellar potential and fragments into self-gravitating clumps that interact, the dispersion increases. As seen in the middle panel, beyond the co-rotation point, gas is accelerated by the spiral arms. Meanwhile, within the bar region, the velocity dispersion is at its highest as the gas is pulled from its circular orbit to follow elongated elliptical paths through the bar. Within this dense region, further cloud interactions also increase the velocity dispersion, a point we will return to when we consider cloud properties.

In Figure 2.4, we show the vertical gas distribution and motion in the galactic disc. The left-panel shows the surface density of four regions of the edge-on disc at 240 Myr (two pattern rotation periods and one gas orbital period at 8 kpc). The top most image shows the complete disc, while the three images below show close-up sections of the bar, spiral and outer disc regions. Overlaid on the lower three images are the positions of the clouds as identified by the contour method in section 2.2.3. Despite the gas cooling from its initial equilibrium temperature

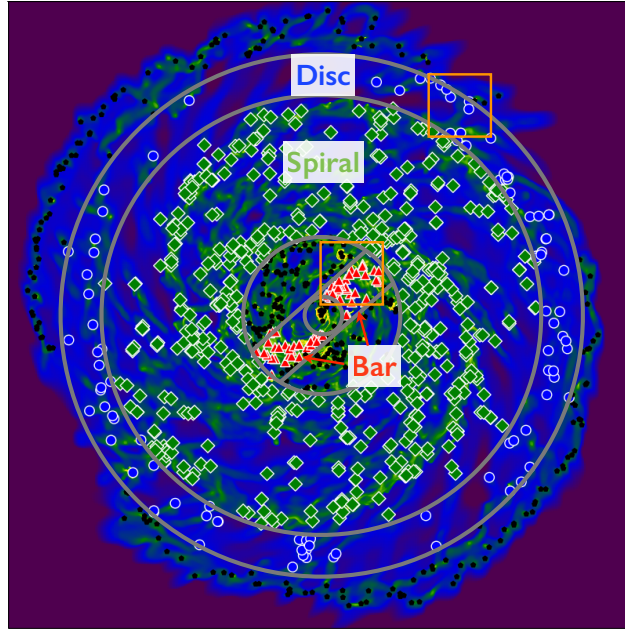


Figure 2.5. The three different galactic environments: bar, spiral and disc. The surface density of the galactic disc is shown at 240 Myr, overplotted with markers denoting the cloud type according to location. Blue circles, green diamonds and red triangles show clouds in the disc, spiral and bar respectively. The black markers show clouds not included in our analysis. The width of the image is 20 kpc, with the two squares marking regions that are shown in close-up in Figure 2.10.

at 10^4 K and the lack of stellar feedback to inject energy, the gas scale height remains around its initial value of 100 pc, but with marked differences between the regions. Within the bar region, the scale height is 115 pc, the spiral region has a scale height of 105 pc and the outer disc has a lower value at 80 pc.

The reason for the regional variations in the scale height can be seen in the right-hand plot of Figure 2.4. This plot shows the normalised vertical velocity distribution of clouds in each of the three bar, spiral and outer disc regions at 240 Myr. In the bar region, the clouds have a broad velocity profile, with vertical velocities out to 50 km/s. In the disc, meanwhile, cloud vertical velocities remain more uniformly around 10 km/s. This difference is due to strong interactions between the clouds. In the bar region, the gas density is high and its flow is highly elongated by the bar potential, decreasing the distance between the clouds. The shear flow at the bar ridge and bar ends also decreases the interaction time, adding to the boost in the velocity dispersion we saw in Figure 2.3. A lesser but still notable effect is also seen in the spiral region, where the arms also gather material together to increase cloud interactions. In the outer disc however, the density of clouds is much lower as can be seen visually in the left-panel of Figure 2.4. The number of interactions is therefore less, resulting in a lower scale height.

2.3.2 Cloud classification based on galactic location

To compare the impact of different galactic environments on GMC properties, we assigned an environment group based on the cloud's physical location within the disc. The boundaries of our three regions, the bar, spiral and disc, are shown in Figure 2.5. If a cloud is found within the radii $2.5 > r > 7.0$ kpc, we recognise the cloud as a *spiral cloud*. Outside $r = 7.0$ kpc are the *disc clouds*, where we intentionally ignore clouds forming on the outer ring instability. This outer dense band of gas is from the Toomre instability (Toomre, 1964) during the disc's initial fragmentation and therefore not as realistic an environment for cloud formation. *Bar clouds* form in a box-like region at the galactic centre, with a length of 5.0 kpc and width 1.2 kpc. The nucleus region inside 600 pc is ignored due to it being very difficult to track clouds in this very

high density area and the absence of a star burst degrading the comparison with observed GMC populations, as discussed in section 2.3.1. We also do not distinguish the difference between spiral arm and interarm regions; the number of clouds sitting between the spiral arms is small and hard to identify consistently as the spiral pattern rotates.

The results of our identification scheme are shown using different coloured markers overlaying the gas surface density at 240 Myr in Figure 2.5. Blue circles show the position of the disc clouds, green diamonds denote spiral clouds and red triangles mark the bar clouds. Black markers are for clouds identified via our contour method described in section 2.2.3 but which we do not include in our analysis for one of the reasons described above. The number of clouds is roughly constant during our main time period of analysis, from 200 - 280 Myrs and clouds rarely move environment during their lifetime. In the 240 Myr snap-shot shown in Figure 2.5, 77 clouds are in the bar region, 515 are in the spiral region and 102 are in the disc.

Cloud properties in each galactic environment

To see the impact of their environment on the cloud formation, we plot the cloud property distributions for clouds in each of our defined regions at 240 Myr in Figure 2.6. In each plot, the red solid line denotes the distributions for clouds found in the bar region, the green dotted line is for clouds in the spiral region and the blue dashed line is the disc clouds. When describing our results below, we have compared most extensively with observational GMC catalogues from the Milky Way (Roman-Duval et al., 2010) and M33 (Rosolowsky et al., 2003). These comparisons have limits, since as Hughes et al. (2013) notes, GMC populations between galaxies have systematic differences and the surveys have been performed at different resolutions. At present, there is no survey of GMCs in M83 due to the low resolution of the molecular line observations; a situation that should change with the results from ALMA cycle 0 and 1. In the meantime, the observations from M33 and the Milky Way provide a guide to assess our simulated cloud results.

Figure 2.6(a) shows the mass distribution for these three environments, where the cloud mass is calculated the sum of the gas mass in each cell belonging to the cloud, as identified by the contour method described in section 2.2.3. In all three cases, the peak value for the cloud mass lies at around $M_c \simeq 5 \times 10^5 M_\odot$. This is in reasonable agreement with the GMCs observed in M33, where the peak mass was found to be $\simeq 10^5 M_\odot$ and larger than observations of the Milky Way, where the peak weighs in at $\simeq 5 \times 10^4 M_\odot$. The Milky Way, however, has an average surface density than is almost one-eighth that of M83 (Lundgren et al., 2004b; Sparke and Gallagher, 2000), likely aiding the production of smaller clouds.

While the typical mass for the clouds does not appear to depend on galactic environment, there are two clear differences between the mass distributions in Figure 2.6(a). Firstly, there is a trend in the broadness of the mass distribution, with the bar clouds having the larger abundance of the most massive ($M_c > 10^7 M_\odot$) and smallest ($M_c < 10^5 M_\odot$) clouds. The disc cloud profile has the most limited range, with the maximum cloud mass found in the disc being just under $2 \times 10^7 M_\odot$, compared to the bar region's maximum at almost $2 \times 10^8 M_\odot$. This high mass end is in keeping with observations performed by Foyle et al. (2013), who investigated the compact FIR bright sources on the *Herschel* maps of M83 to estimate the mass of the giant molecular associations. These GMAs had a gas mass in the range of $10^6 - 10^8 M_\odot$, in agreement with our own clouds. It should be noted, however, that Foyle et al. (2013)'s resolution is limited to spatial scales around 200-300 pc and our own simulation lacks star formation and feedback. Both of these may have an influence in increasing maximum cloud size, with similar simulations demonstrating star formation can reduce cloud mass above $10^7 M_\odot$ (Tasker, 2011).

The second notable feature is that the distribution of the bar clouds is bimodal, with two peaks at $M_c \simeq 5 \times 10^5 M_\odot$ and at $M_c \simeq 2.0 \times 10^7 M_\odot$. The second of these peaks marks out the high mass clouds which appear as a distinct population, rather than a declining tail as seen in the spiral and disc regions. Similar splits can be seen in the radii and surface density distributions and was an unexpected phenomenon whose origin we will return to below.

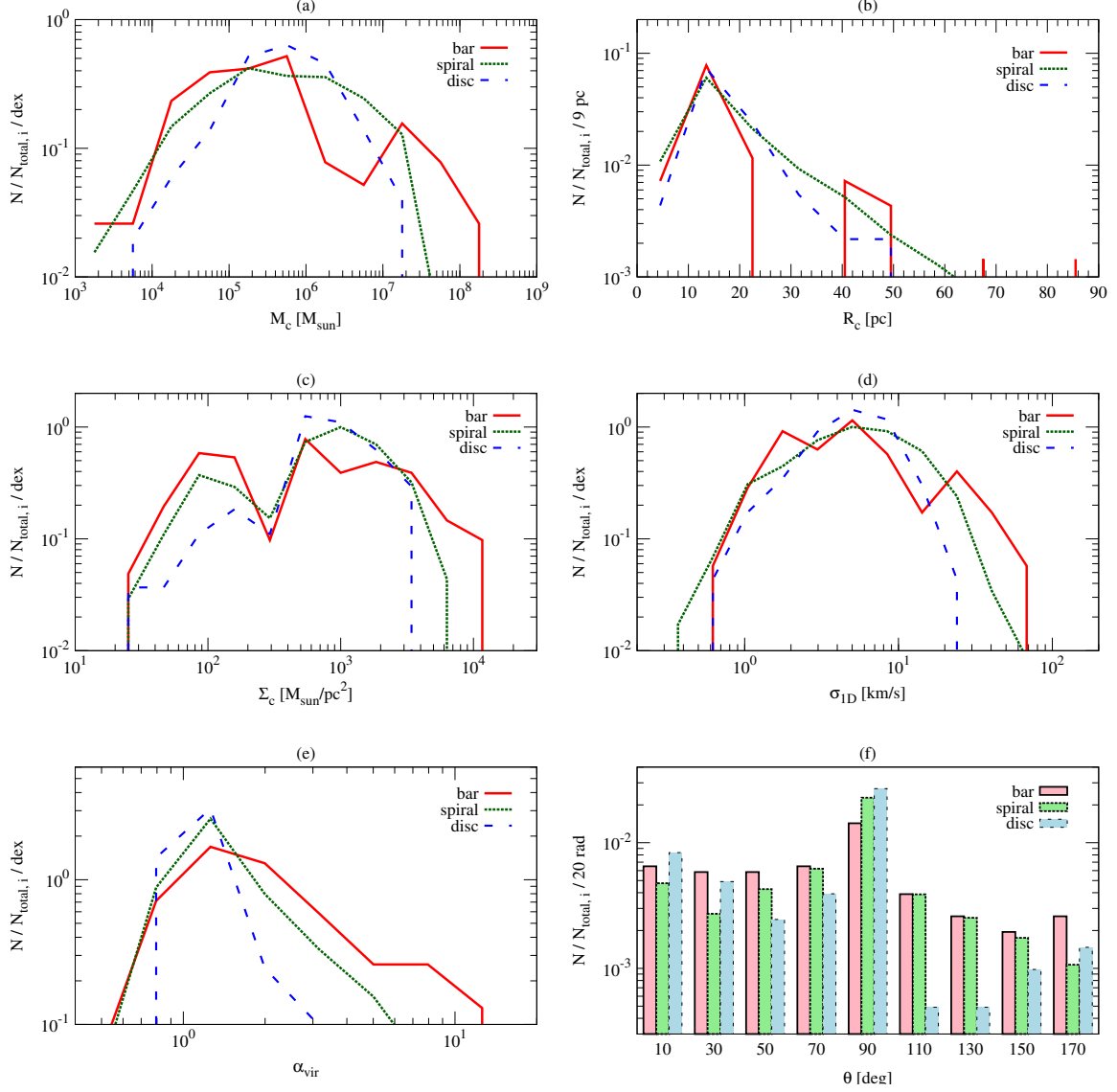


Figure 2.6. Normalised distributions of the cloud properties in the bar region (solid red lines), spiral region (dotted green lines) and disc region (dashed blue line) at 240 Myr. Plots show: (a) the cloud mass, M_c , (b) the average cloud radius, $R_c = \sqrt{(A_{xy} + A_{yz} + A_{zx})/3\pi}$, where A_{xy} is the projected area of the cloud in the x-y plane, A_{yz} is that in the y-z plane, and A_{zx} is in the z-x plane, (c) the cloud surface density, $\Sigma_c = M_c/(\pi R_c^2)$, (d) the 1D velocity dispersion, $\sigma_{1D} = \frac{1}{\sqrt{3}}\sqrt{[(v_x - v_{cx})^2 + (v_y - v_{cy})^2 + (v_z - v_{cz})^2]}$, where (v_x, v_y, v_z) is the velocity of the gas and (v_{cx}, v_{cy}, v_{cz}) is the cloud's centre of mass velocity, (e) the virial parameter, $\alpha_{\text{vir}} = 5(\sigma_{1D}^2 + c_s^2)R_c/(GM_c)$, where c_s is a sound speed. The virial parameter is a measure of gravitational binding; a value greater than 1 indicates that the cloud is gravitationally unbound, (f) the angle θ between the cloud angular momentum vector and the galactic rotation axis.

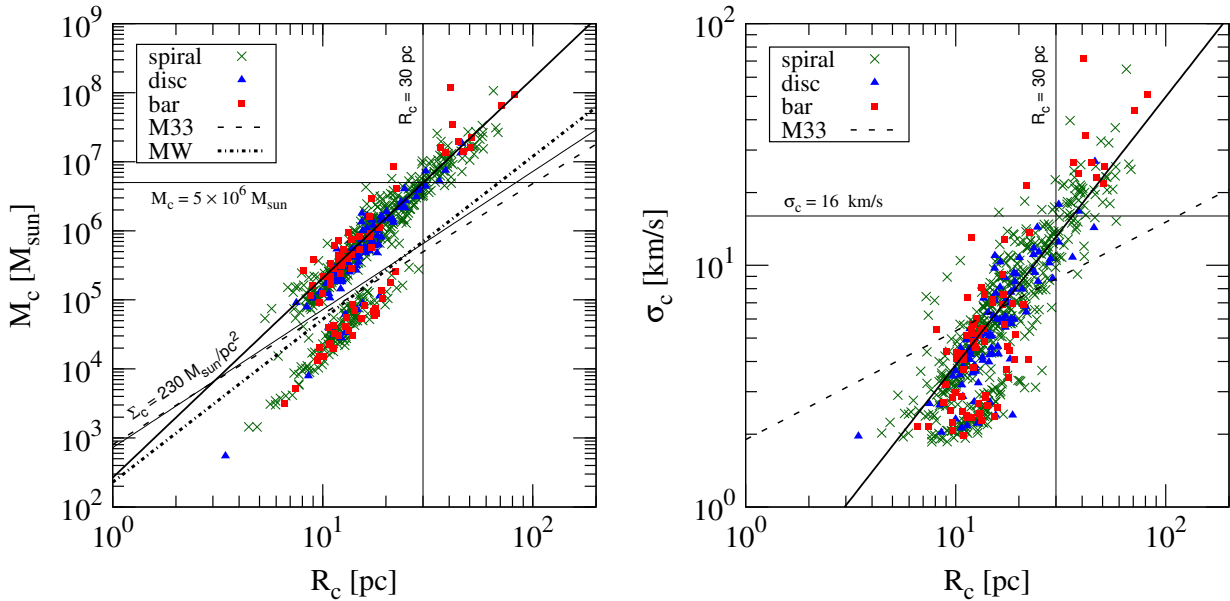


Figure 2.7. Mass versus radius relation (left) and velocity dispersion versus radius relation (right) for clouds at 240 Myr. Coloured markers denote clouds in different galactic regions: green crosses show spiral clouds, blue triangles are disc clouds and red squares are bar clouds. The black solid lines show the turning points of the distributions in Figure 2.6. The black dashed lines in the both panels show the scaling relation for M33, with $M_c = 801 R_c^{1.89}$ (left panel) and $\sigma_c = 1.9 R_c^{0.45}$ (right panel) (Rosolowsky et al., 2003), while the black dotted-dashed line in the left panels shows scaling relation for the Milky Way, with $M_c = 228 R_c^{2.36}$ (Roman-Duval et al., 2010).

All the trends observed in the mass distribution are repeated in the distribution for the cloud radii, shown in Figure 2.6(b), which defines the average radius of the cloud as

$$R_c \equiv \sqrt{\frac{(A_{xy} + A_{yz} + A_{zx})}{3\pi}}, \quad (2.9)$$

where A_{xy} is the projected area of the cloud in the x-y plane, A_{yz} is that in the y-z plane, and A_{zx} is that in the z-x plane. As with the mass, the peak value for the radius is the same for the bar, spiral and disc regions at $R_c \simeq 11$ pc. This typical size agrees well with observations of the GMCs in both the Milky Way and M33, which show characteristic radii of 9 pc and 10 pc, respectively. While the majority of clouds are found at this radius in all environments, there is again a trend to find larger clouds in the spiral and bar, with the largest clouds in the galaxy forming in the bar region. Disc clouds, meanwhile, remain below 50 pc.

We also see further evidence for a bimodal bar region population, with a clear deficit of clouds between 20-40 pc in this environment. The spiral and disc populations appear to show a more gradual decline with the numbers of clouds at higher radii steadily decreasing.

This situation changes when we look at the cloud surface density in Figure 2.6(c). Here, the cloud surface density is defined as

$$\Sigma_c \equiv \frac{M_c}{\pi R_c^2}. \quad (2.10)$$

In this distribution, all three environments show a clear bimodal nature, with peaks at $\Sigma_c \simeq 10^2 M_{\odot}/\text{pc}^2$ and $\Sigma_c \simeq 10^3 M_{\odot}/\text{pc}^2$. The first of these two peaks corresponds well with the typical surface density of the Milky Way clouds, which peaks around $10^2 M_{\odot}/\text{pc}^2$.

The two populations in the bimodal distributions are most evenly distributed in the case of the bar clouds, with the peaks taking approximately equal magnitudes. The spiral and disc clouds show a smaller population for the lower surface density peak, which is least marked in

the disc clouds. The three environment groups also follow the previous trend, with the bar clouds having the largest fraction of low surface density clouds ($\Sigma_c < 3 \times 10^2 \text{ M}_\odot/\text{pc}^2$) and high surface density clouds ($\Sigma_c > 4 \times 10^3 \text{ M}_\odot/\text{pc}^2$), while the disc clouds retain the smallest range.

Perhaps the most surprising feature of the bimodality in the surface density is that it is seen in all three populations, while the mass and radius distributions only show a split for the bar clouds. Moreover, the divide in the surface density appears to occur in the middle of the distribution, whereas the mass and radial plots suggest a smaller population of larger objects. To explore the origin of this phenomenon, we plotted the mass versus radius in the left-hand panel of Figure 2.7.

Known as one of Larson (empirical) laws (Larson, 1981), the scaling relation between cloud mass and radius has been observed both for GMCs in the Milky Way and for cloud properties in other galaxies. The dashed and dot-dashed line on the left-hand panel of Figure 2.7 show the observational fits, with the former being the M33 relation, $M_c = 801 R_c^{1.89}$ and the latter, the Milky Way's scaling, $M_c = 228 R_c^{2.36}$.

However, instead of seeing a single correlation between the cloud mass and its radii, Figure 2.7 shows two parallel sequences lying either side of the observational results. These two sequences exist within each environment and correspond to the bimodality in the cloud surface density distribution in Figure 2.6(c). The upper correlation contains clouds with a surface density higher than $\Sigma_c = 230 \text{ M}_\odot/\text{pc}^2$, while the lower line has clouds below that limit.

If we focus purely on the bar clouds in Figure 2.7 (shown with red square markers), we can see there is another split in the upper, high surface density, sequence. In the plot region around $M_c \sim 5 \times 10^6 \text{ M}_\odot$ and $R_c \sim 30 \text{ pc}$, there is a complete deficit of bar clouds. This then, corresponds to the bimodality of the mass and radii distributions in the bar cloud population in Figure 2.6(a) and (b). Clouds above these values are large and massive and typically not found in the disc region. The spiral region has clouds that extend into this area, but the number is low compared to the quantity of clouds of smaller size. The bar clouds, meanwhile, have a significant fraction of their number in this upper region, with the smaller clouds split between the two scaling sequences. Thin black lines on Figure 2.7 show the divisions for these three cloud groups which will be discussed as their own cloud types in the next section.

If we return to Figure 2.6(d), the distribution of the one-dimensional velocity dispersion of the clouds in the three environments is shown. The mass weighted, one-dimensional velocity dispersion is defined as

$$\sigma_{1D} = \sqrt{\frac{(v_x - v_{cx})^2 + (v_y - v_{cy})^2 + (v_z - v_{cz})^2}{3}}, \quad (2.11)$$

where (v_x, v_y, v_z) is the velocity of the gas and (v_{cx}, v_{cy}, v_{cz}) is the cloud's centre of mass velocity. As with the previous distributions, the peak dictating the typical cloud velocity dispersion is the same for all regions with a value of $\sigma_{1D} \simeq 6 \text{ km/s}$. This is comparable to the 6 km/s characteristic velocity of the M33 and slightly larger than the Milky Way's 1 km/s, which corresponds to the smaller cloud size.

At the high velocity dispersion end of the plot, the bar clouds have the largest relative population, with the greatest fraction of clouds with $\sigma_{1D} > 30 \text{ km/s}$. This is followed by the spiral and then disc populations, with the majority of the disc clouds having velocity dispersions less than 20 km/s. The bar population is again bimodal, with peaks at $\sigma_{1D} \simeq 5 \text{ km/s}$ and $\sigma_{1D} \simeq 23 \text{ km/s}$.

We can see this bimodality again by looking at the second Larson scaling relation between velocity dispersion and radius ($\sigma_c \propto R^b$), as shown in the right-hand panel of Figure 2.7. To better compare with the observational measurements, the velocity dispersion used includes the combined thermal component and is defined as:

$$\sigma_c = \sqrt{\sigma_{1D}^2 + c_s^2}, \quad (2.12)$$

where c_s is the sound speed of cloud. This addition makes only a small difference, since the cold cloud gas has a typical sound speed of $c_s \simeq 1.8$ km/s, 0.6% of the non-thermal 16 km/s motions. The power-law fit for the observational data from M33 is shown as a dashed line, with an index of $b = 0.45$. The upper sequence in the bimodality lies on this observational relation but with a steeper inclination, giving $b = 1.1$. This value sits on the upper observed bound (Shetty et al., 2012) but is considerably higher than the typical measurements, which agree with the M33 result of $b \sim 0.5$ (Solomon et al., 1987; Bolatto et al., 2008; Hughes et al., 2010). This steepening may be due to a sensitivity to the physics not included in this simulation. In particular, the lack of feedback may allow our larger clouds to become more bound (and thereby have a higher velocity dispersion) while our smaller clouds may struggle to resolve the internal motions.

As with the mass-radius scaling relation in the left panel, the linewidth-radius relation shows two sequences, although the lower sequence is significantly smaller than the upper trend. In the upper sequence of the bar clouds, there is a gap at $\sigma_c \sim 16$ km/s and $R_c \sim 30$ pc, corresponding to the bimodal splits in Figure 2.6(d) and (b), the same segregation that is seen for the bar clouds in the mass and radius relations.

The final two plots in Figure 2.6 show the virial parameter and the orientation of the GMCs. The virial parameter in Figure 2.6(e) is defined at

$$\alpha_{\text{vir}} = 5 \frac{\sigma_c^2 R_c}{GM_c}. \quad (2.13)$$

and is a measure of the gravitational binding. A value of $\alpha_{\text{vir}} > 2$ indicates that the cloud is gravitationally unbound while $\alpha_{\text{vir}} < 2$ suggests a bound system (Bertoldi and McKee, 1992). The clouds in all three environments show a peak α_{vir} value of ~ 1 , indicating that the majority of the clouds are virialised but only marginally bound. Clouds in the Milky Way are observed to have a slightly lower α_{vir} value of $\simeq 0.46$.

There is no obvious bimodal split in any of the cloud populations, but at values of $\alpha_{\text{vir}} > 2$, the bar region contains a significantly higher fraction of clouds. This is followed by clouds in the spiral and disc region, whose distributions drop off smoothly after $\alpha_{\text{vir}} \sim 1$. While the bar clouds also peak at this value, the majority of clouds sit to its right, indicating that most clouds in the bar region are unbound and take on a wide range of virial parameters. By contrast, the range in α_{vir} in the disc is much lower, with most of the populations sitting close to the peak value. This difference in the range of α_{vir} could indicate a more dynamic environment, where clouds have less time to settle to a virialised state.

The final plot in Figure 2.6, (f), shows the distribution of the angle θ , between the cloud angular momentum vector and the galactic rotation axis. The cloud angular momentum is defined as the rotation with respect of the centre of mass of the cloud, with $0^\circ < \theta < 90^\circ$ indicating a prograde rotation in the same sense as the galaxy and $90^\circ < \theta < 180^\circ$ consisting of clouds with retrograde motion. In agreement with previous simulations (Tasker and Tan, 2009), clouds forming during the initial fragmentation of the disc ($t < 10$ Myr) are born prograde, inheriting the galactic disc's rotational direction, $\theta \sim 0^\circ$. After one pattern rotation period ($t < 120$ Myr), when the disc has fully fragmented, the fraction of clouds at different spin orientations begins to increase. The disc clouds show the slowest evolution, with the population of high prograde and retrograde clouds increasing fastest in the bar, followed by clouds in the spiral region. By 240 Myr, all three regions have clouds with the full range of orientations to the galactic rotation axis. The peak rotation angle actually sits at $\theta = 90^\circ$, suggesting most clouds rotate perpendicular to the disc. The fraction of retrograde rotating clouds is largest in the bar region, with the disc clouds remaining predominantly prograde.

In their isolated Milky Way model, Tasker and Tan (2009) suggest that the cloud's initial prograde rotation can be lost during encounters with other clouds, e.g. cloud-cloud collisions or tidal interactions. The faster shift towards a more retrograde population is therefore indicative of a more dynamic environment with many cloud interactions. This ties in with the virial

	Bar	Spiral	Disc
Type A	49.4% (38/77)	64.1% (330/515)	83.3% (85/102)
Type B	13.0% (10/77)	12.8% (66/515)	5.9% (6/102)
Type C	37.7% (29/77)	23.1% (119/515)	10.8% (11/102)

Table 2.1. The percentage of each cloud type in each galactic region at $t = 240$ Myr. Bracketed numbers show the actual number of clouds of that type divided by the total cloud number in the region.

parameter distribution in Figure 2.6(e), which shows clouds in the spiral and bar tend to be less bound, consistent with a high number of interactions.

Observations of M33 shows a range of cloud rotations, with 47% having a prograde rotation, 32% having a rotation perpendicular to the disc and 21% with retrograde rotation. If cloud interactions are a dominant form of higher θ values, then this suggests that cloud environment (which will dictate such encounters) is a key factor in determining GMC properties.

A last property that can be extracted from the data in this section concerns the stability of the disc. Traditionally, the resistance of a rotating disc to fragmentation is measured by the Toomre Q parameter for gravitational stability (Toomre, 1964). Defined as $Q = \kappa c_s / \pi G \Sigma_g$, where κ is the epicycle frequency, c_s is the thermal sound speed in the disc and Σ_g is the gas surface density, a value of $Q < 1$ indicates instability while higher Q values imply the disc will not fragment. Since Toomre (1964)'s original calculation involved a two-dimensional disc, the exact threshold for stability is debatable, with values between 1.5 - 0.7 being suggested via calculation and observation for a three-dimensional system (Goldreich and Lynden-Bell, 1965a; Kennicutt, 1989; Gammie, 2001).

Our disc begins with a steadily rising Q value between 2 and 4 from 1 kpc to the outer edge. As the gas cools, this drops to between 0 and 2 over the majority of the disc surface, suggesting (correctly) that the disc will fragment. However, when the gas breaks into the objects we identify as the GMCs, the azimuthally averaged Q value increases as cold gas is bound up in the clouds while the larger volume of surrounding warmer gas is stable. This has also been seen in other simulations of galaxy discs such as Tasker and Tan (2009); Tasker (2011). While the Q value implies the disc is now stable, this conclusion has to be incorrect since regions within the clouds must collapse to form stars. This discrepancy was noticed by Romeo et al. (2010), who pointed out that the Toomre equation assumes a well defined surface density and velocity dispersion, whereas in fact the Larson scaling relations show these properties are strongly dependent on the size of the region being measured due to turbulence. They argue that turbulence within the GMCs produces a transition between instabilities governed by large-scale gravitational fragmentation (Toomre) and those controlled by small-scale turbulence.

To assess which of these forces has the upper hand, Romeo et al. (2010) created a stability map based on the indices in the Larson scaling relations, a and b : $M \propto R^{a+2}$ and $\sigma \propto R^b$. From our fits in Figure 2.7, we find $a = 0.9$ and $b = 1.1$, placing our clouds close to the border between Toomre stability and small-scale instability. Such a balance is expected if the clouds are virialised since the pressure balancing the self-gravity would follow the same scaling with size (Romeo et al., 2010; Hoffmann and Romeo, 2012). However, our exact values place our clouds just above the line, suggesting that while close to virialisation, turbulence will initiate further instability. We therefore conclude that after the initial fragmentation, the disc is borderline stable to gravitational instabilities but unstable to turbulence.

2.3.3 Cloud classification based on cloud properties

To understand with physical reasons for the distinct splits in the cloud properties found in section 2.3.2, we re-classify all clouds according to the two sequences seen on the mass-radius relation in Figure 2.7 and the bimodality in the bar mass and radius distributions in Figure 2.6(a) and (b). This is shown in Figure 2.8(a), where clouds that sit on the upper bimodal

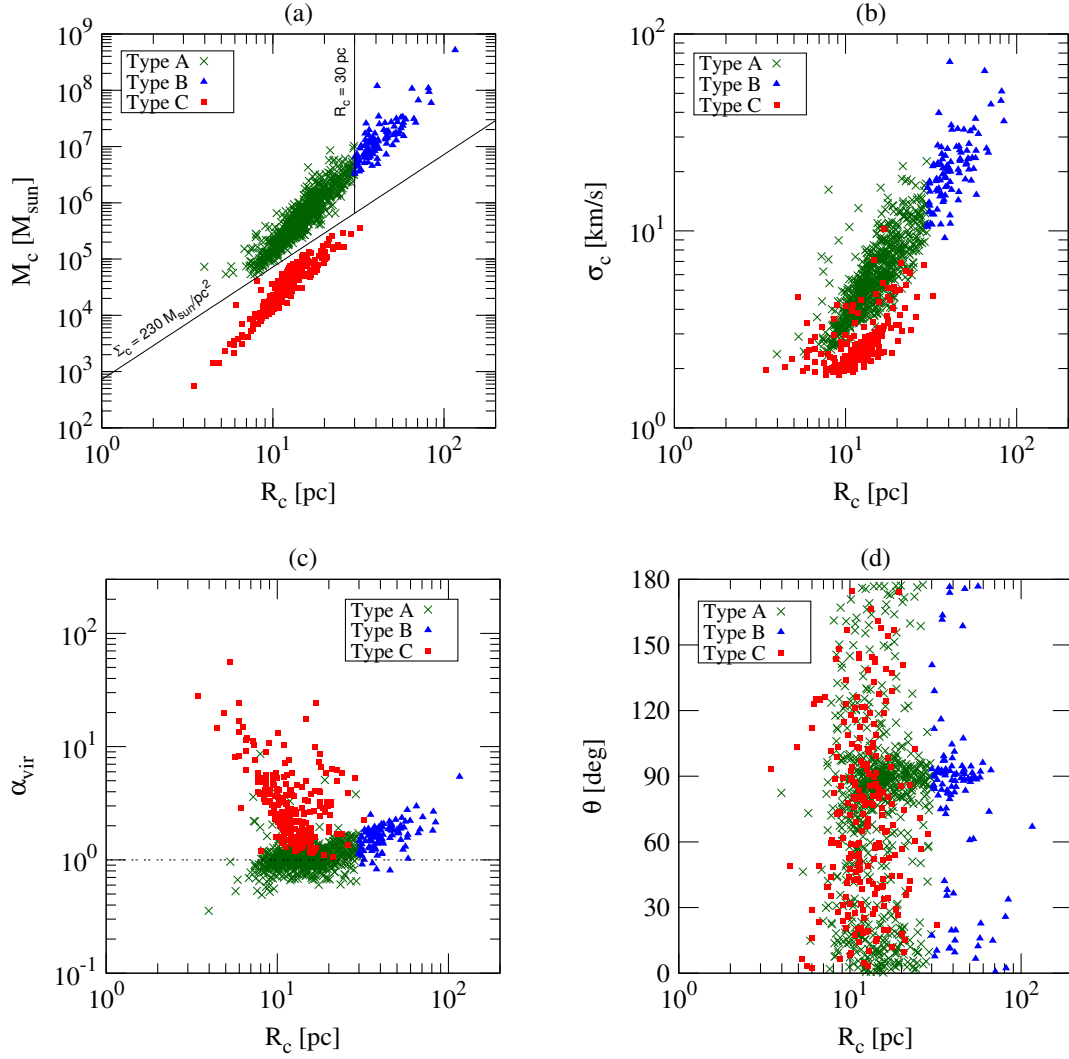


Figure 2.8. Scaling relations for our three cloud type categorisations at $t = 240$ Myr. Top left (a) shows the mass versus cloud radius and defines the three cloud types: *Type A* clouds exist on the upper trend of the bimodal split, with surface densities greater than $230 M_{\odot}/\text{pc}^2$. *Type B* clouds sit at the high end of the same sequence, with radii greater than 30 pc. *Type C* clouds follow the lower trend and have surface densities less than $230 M_{\odot}/\text{pc}^2$. The top right plot (b) shows the velocity dispersion versus cloud radius, lower left (c) plots the virial parameter against radius and lower right (d) shows the angle between the cloud’s angular momentum axis and that of the disc, plotted against cloud radius.

trend with surface densities above $230 M_{\odot}/\text{pc}^2$ and radii less than 30 pc form the group of *Type A* clouds, clouds along the same sequence but with radii above 30 pc are declared *Type B* and clouds following the lower trend with surface densities below $230 M_{\odot}/\text{pc}^2$ are *Type C*.

The split between cloud types in each galactic region is shown in Table 2.1. In all galactic environments, the most numerous cloud is *Type A*, but this percentage is significantly smaller in the bar regions where 38% of the cloud population are of *Type C* and a further 13% are *Type B*. In contrast, the disc region comprises mainly of *Type A* clouds with less than 6% *Type B* and only about 10% *Type C*.

Properties of the three cloud types

While these three new cloud classifications are based on their surface density and radius, their other properties also show marked differences. From our initial definition plot in Figure 2.8(a), it is clear that *Type B* clouds are not only extended, they are also massive. This is not surprising, since we see the bimodality in the bar clouds both in the mass and radius distributions, but it rules out the possibility that this cloud type could be dense tidal tails.

Figure 2.8(b) shows the scaling relation between velocity dispersion and cloud radii. As was indicated in Figure 2.7, the velocity dispersion also differs between the three types, with *Type C* clouds having a lower velocity dispersion than a *Type A* cloud with the same radius. To match their extended structure, *Type B* clouds have higher velocity dispersions than either *Type A* or *Type C* objects, with values above 10 km/s.

Another significant difference between the cloud types involves their gravitationally binding. Figure 2.8(c) plots the virial parameter, α_{vir} as defined in section 2.3.2, against the cloud radius. *Type A* clouds are borderline gravitationally bound, with their α_{vir} values clustered around 1.0. The extended *Type B* clouds are less bound, fitting in with their larger size and correspondingly higher velocity dispersion. Their values extend between 1 - 5 as the cloud increases in radii. More notable are the *Type C* clouds, which for similar radii to the *Type A* objects, are far less bound with α_{vir} values extending from 1 to 70 in a reverse trend where the smaller objects are the least gravitationally bound. This implies the *Type C* clouds are less compact than the other two populations of GMCs, explaining why they follow the lower trend in Figure 2.8(a).

In the final panel (d) in Figure 2.8, we show the variation of the cloud's angular momentum vector with cloud type. There is no correlation between θ and cloud radius, with clouds at any radii potentially having the full range of spin orientations. However, the massive *Type B* clouds have a smaller spread of orientations, with most of the clouds clustered around $\theta \sim 90^\circ$. *Type C* clouds meanwhile, appear to have no preferred direction, forming a spread over the full angular range. The *Type A* clouds cluster between $\theta = 0 - 90^\circ$, indicating that these clouds may change their orientation during their lifetime.

Cloud lifetime and merger rate

Whether there is time during the cloud's life for such a orientation change is considered in Figure 2.9 where the cloud lifetime distribution (left) and the merger rate distribution are plotted for each of the cloud types. Since the initial fragmentation of the disc is not a realistic environment for the cloud, only clouds that form between $t = 200 - 280$ Myrs are included in the distributions. Although our model does not have stellar feedback which is believed to aid cloud destruction, clouds can die in our simulation through merger events, tidal stripping leading to dissipation or simply dissipation due to the cloud being unbound and perturbed by nearby structures.

All clouds, regardless of type, have a typical lifetime of less than 20 Myr. While the age of GMCs is a heavily debated subject, this agrees well with estimates that suggest clouds live 1-2 dynamical times with ages in the range 5-30 Myr (Blitz et al., 2007; Kawamura et al., 2009; Miura et al., 2012). The fact we get such good agreement with observational estimates of cloud lifetimes without any feedback processes is notable; this could imply that feedback has a small

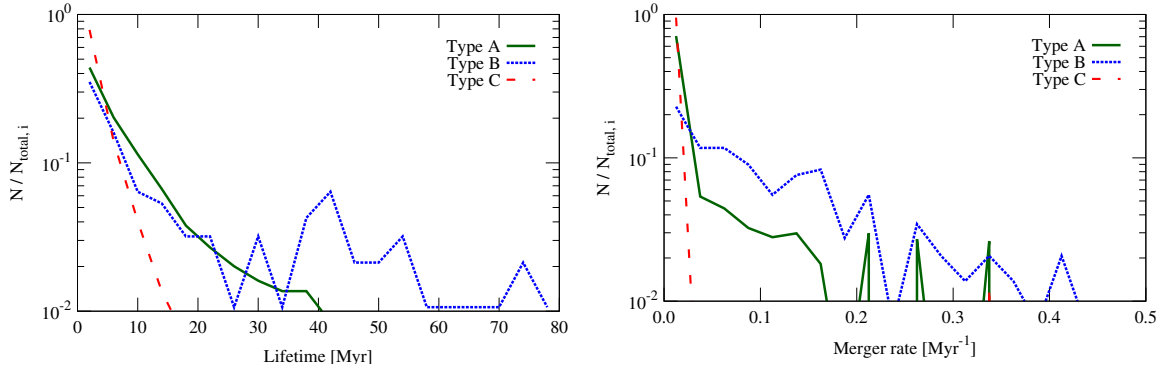


Figure 2.9. Normalised distribution of cloud lifetime (left) and the merger rate per Myr of clouds that are born between $t = 200 - 280$ Myr.

impact on the majority of the cloud’s evolution. A possible reason for why this could be was noted by Renaud et al. (2013), who found that in simulations of the Milky Way, the stars have moved out of the gas cloud before they go supernovae, resulting in minimal impact on their host GMC.

While the typical value for cloud lifetime is shorter than 10 Myr, the range in the distribution differs greatly between the cloud types. *Type A* clouds agree most closely with the observed lifetimes, ranging up to 50 Myr, with 95% living for less than 20 Myr. By contrast, *Type B* consist of far more long lived clouds, with over 20% living longer than 40 Myr. Note that the true maximum lifetime of *Type B* clouds is unknown, since they extend up to 80 Myr, the maximum possible lifetime in our analysis period. We will see in the next section that this cloud type is very hard to destroy in our simulation. The smallest range of lifetimes is for *Type C* clouds, the vast majority of which have a lifetime of only a few Myr. These clouds are therefore low density, transient objects that die in a short period of time.

A measure of the interaction between the clouds during their lifetime can be seen deduced from the lower panel in Figure 2.9, which plots the merger rate between clouds. As discussed in section 2.2.3, a merger is defined where a single cloud appears close to the predicted position of two or more clouds that existed 1 Myr previously. It is a lower estimate of the true interaction rate, since it does not include tidal shredding where two identifiable objects exist at the end of the encounter.

The massive *Type B* clouds have the highest merger rate, extending up to 1 merger every 2-3 Myr. This means that these clouds undergo many mergers during their lifetime, accounting for their large mass and size. The transient *Type C* clouds have the lowest merger rate, in keeping with their very short lifetimes. Shortly after their birth, they either merge or their low density causes them to dissipate.

Type A clouds also experience mergers (although less than for *Type B*), with the majority of clouds experiencing 1-2 mergers during their lifetime. This likely accounts for the range in the angular momentum angle distribution, θ , see in Figure 2.8(d), where clouds were found predominately between $\theta \sim 0$ and 90° . *Type A* clouds are therefore born prograde but gain the higher θ value through cloud collisions. This is not true for *Type B* who, while undergoing many mergers, are too massive to have their angular momentum greatly affected. The transient *Type Cs* appear to have no preferred direction and do not live long enough to undergo mergers, suggesting they can be born at any orientation.

The effect of galactic environment on cloud formation

The final confirmation of the origin of the properties of the three cloud types comes from visual inspection of the disc. Figure 2.10 shows 2 kpc patches of the gas surface density taken in the bar region and disc region. The image is overlaid with markers showing the centre of mass of

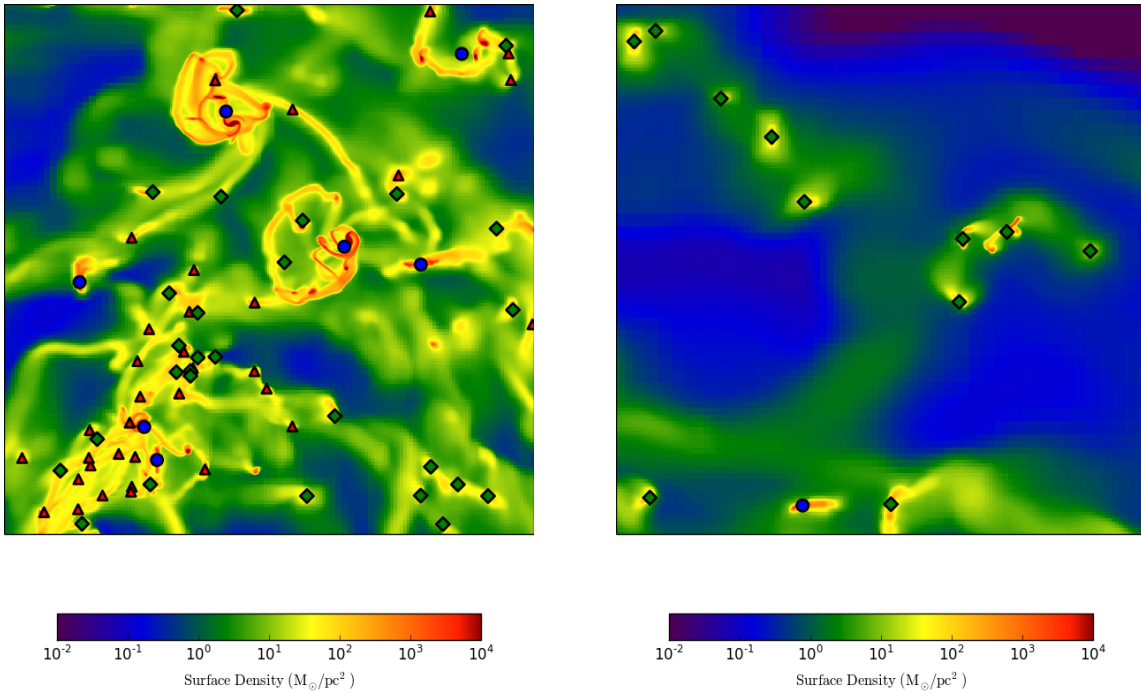


Figure 2.10. 2 kpc gas surface density images of regions in the bar 1.5 kpc from the galactic centre (left) and disc, 8 kpc from the galactic centre. The position of these two sections is shown on Figure 2.5. Markers show the location of the three different cloud types. Green diamonds label *Type A* clouds, blue circles mark *Type B* and red triangles are *Type C*.

the clouds, with *Type A* clouds denoted by green diamonds, *Type B* clouds shown with blue circles and *Type C* with red triangles.

In the left-hand image, we see a section of the bar with a large number of *Type A*, *B* and *C* clouds visible. The massive *Type B* are the most obvious, forming giant molecular associations that drag in surrounding gas and clouds to produce the high merger rate. The bigger mergers are with *Type A* clouds that form the gaseous spiral tidal tails as they pass by or merge with the GMA *Type Bs*. In these tidal tails sit the *Type C* clouds. These objects form briefly in the dense filaments, but are swiftly swallowed or dispersed by the plethora of interaction around them.

This myriad of action occurs in the bar region due to the high density of material gathered by the stellar bar potential and the constrained elliptical motions, bringing clouds into regular contact with one another. These interactions increase the number of tidal tail filaments formed, birthing a high number of *Type C* clouds. Without a source of destruction, *Type B* clouds continue to collect matter and grow for an indefinite period. While their size would make them difficult to destroy with internal feedback, including such a mechanism would likely reduce the maximum size the GMAs reached.

On the other hand, the disc region shows a far more quiescent environment. The clouds are more widely spaced, leading to fewer interactions which slows the creation of the massive GMA *Type Bs*, explaining the 6% population shown in Table 2.1. The vast majority of the clouds are *Type A* which, with less interactions, lack filaments to produce the transient *Type C* population. This low merger rate is due to the lack of the grand design potential to gather gas and gravitationally confine it to the region.

The spiral region forms a mid-point between the inactivity in the disc region and the intense interactions in the bar. It therefore has an intermediate population of clouds in each of the three types.

In our model, therefore, gas typically fragments into a *Type A* GMC. These have properties in good agreements with the typical average observed in many galaxies. However, interactions between clouds produce the tails of these properties in the form of *Type B* and *Type C* clouds. The role of the galactic environment is therefore to drive these interactions, causing these additional populations of clouds to form.

2.3.4 Star formation

Despite not including an active star formation recipe in our simulation, we can estimate the galaxy's star formation rate based on the properties of the gas. Even while restricting star formation to the inner regions of GMCs, the exact conditions that control when a star is born remains an area of active research. We therefore consider three different star formation models which make different assumptions about the parameters controlling the star formation rate.

Standard star formation model

Since the actual collapse of gas into a star cluster is still below our resolution limit, it is reasonable to assume that all GMCs contain Jeans unstable regions that will collapse to form stars. This first star formation model is the simplest product of this assumption, with the star formation rate depending only on the cloud mass and its free-fall time,

$$\text{SFR}_c = \epsilon \frac{M_c}{t_{\text{ff},c}} = \epsilon \frac{M_c}{\sqrt{\frac{3\pi}{32G\rho_c}}} \quad (2.14)$$

where $\epsilon = 0.014$, the star formation efficiency per free-fall time Krumholz and McKee (2005), and $\bar{\rho}_{\text{cloud}}$ is the mean density of the cloud.

The top panel in Figure 2.11 shows the Kennicutt-Schmidt relation (Equation 2.1) using this model. Each point on the graph marks the value for a cylindrical region with radius 500 pc in the galactic plane. This region size was chosen to be comparable to the observational data in nearby galaxies, which finds a near linear relationship between the gas surface density, Σ_{gas} , and the surface star formation density, Σ_{SFR} , for densities higher than $10 M_{\odot}/\text{pc}^2$ (Bigiel et al., 2008). Since multiple GMCs exist within these regions, the star formation rate is calculated as the sum for each cloud within the cylinder.

In agreement with observations, the gas and star formation rate surface densities follow a nearly linear trend in all three galactic environments. There is a small deviation towards a steeper gradient at densities below $\sim 10 M_{\odot}/\text{pc}^2$ and also an increased scatter due to the smaller number of clouds found within our measured region. Note this change has a different origin to the observational results, where the break at the same threshold is due to the transition between atomic and molecular hydrogen. In our simulations, only atomic gas is followed, so we do not expect to observe such a split. It is more likely that clouds in low density regions are less centrally concentrated, due to fewer interactions resulting in tidal stripping.

The overall star formation rate is approximately a factor of 10 higher than that observed. Such elevation in simulations is usually put down to the absence of localised feedback, which would be expected to dissipate the densest parts of the cloud and thereby reduce the star formation rate regardless of whether the cloud itself was also destroyed (Tasker, 2011). In our case, we also lack an actual star formation recipe, meaning that our densest gas is allowed to accumulate inside the cloud without being removed to create a star particle. This adds to the cloud mass and raises the expected star formation rate.

While there is an overall agreement in the gradient, the difference in the star formation rate in the bar, spiral and disc is also apparent. The bar region contains the highest density of clouds, as well as a larger fraction of the massive *Type B* clouds. This produces the upper end of the gas and star formation rate surface densities. The sparser, smaller clouds of the disc region result in correspondingly lower values and the spiral region sits in between.

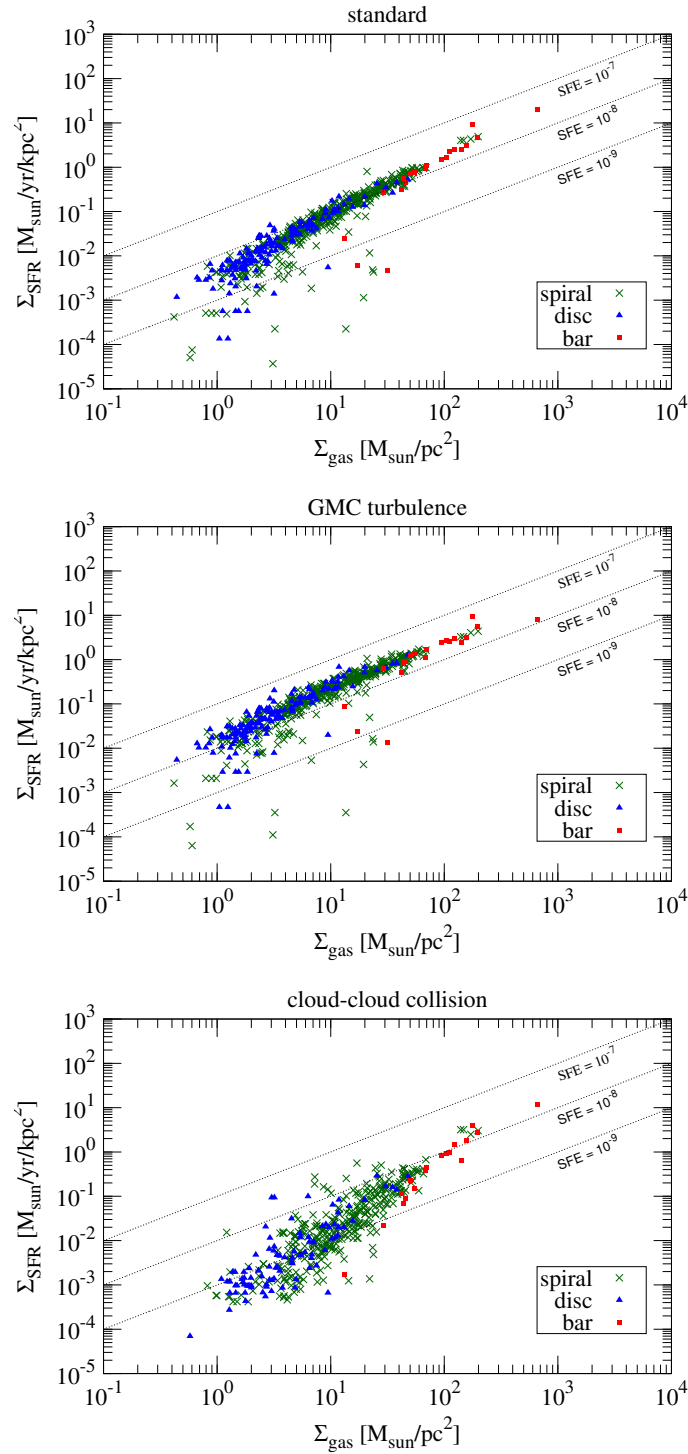


Figure 2.11. The Kennicutt-Schmidt relation for three different star formation models. The surface area is calculated in the x-y plane (face-on disc) and the data is averaged over a cylindrical region with radius 500 pc and 5 kpc height. Top panel shows the results from our *standard star formation model*, section 2.3.4, where the star formation depends only on the mass and free-fall time of the cloud. Middle panel shows the Krumholz and McKee (2005) *GMC turbulence model*, section 2.3.4, where the turbulent motion of the GMCs is considered. The bottom panel is the *cloud-cloud collision model* in section 2.3.4, proposed by Tan (2000), where star formation is regulated by GMC interactions. The black dotted lines show constant star formation efficiency: $\text{SFE} = 10^{-7}$, 10^{-8} , 10^{-9} $[\text{yr}^{-1}]$.

GMC turbulence star formation model

We can compare the results of the straightforward free-fall collapse with a star formation model that also considers the importance of turbulent motions within the GMCs. Proposed by Krumholz and McKee (2005), this power-law model assumes that the clouds are supersonically turbulent, producing a log-normal density distribution. By demanding that gas collapses when the gravitational energy exceeds the turbulent energy within a cloud, they find the modified relation,

$$\text{SFR}_c = \epsilon \left(\frac{\alpha_{\text{vir}}}{1.3} \right)^{-0.68} \left(\frac{\mathcal{M}}{100} \right)^{-0.32} \frac{M_c}{\sqrt{\frac{3\pi}{32G\rho_c}}} \quad (2.15)$$

where $\epsilon = 0.014$ is again the star formation efficiency per free-fall time and α_{vir} is the virial parameter as defined in Equation 2.13. \mathcal{M} is the Mach number, defined as the ratio between the cloud's 1D velocity dispersion and sound speed, $\mathcal{M} \equiv v_c/c_s$.

The results from this model are shown in the middle panel of Figure 2.11. The surface area and surface star formation rate was calculated as before over a cylindrical region with radius 500 pc. The addition of turbulence regulation to the star formation rate makes only a small difference to the result, due to the addition terms in Equation 2.15 typically multiplying the result by only a factor of 1-2. Clouds in the low density region are affected the most, since these correspond to disc clouds with a lower velocity dispersion. This produces an overall tighter relation throughout the disc, with the gradient of unity.

The overall trends between the three environments remain unchanged from those observed in section 2.3.4. However, the tightening in the Kennicutt-Schmidt relation when environmentally dependent properties such as α_{vir} and the velocity dispersion are included emphasises the importance of the galactic structure in GMC evolution.

Cloud-cloud collision star formation model

Our final model moves away from a Jeans unstable cloud to a scheme motivated by triggered star formation. In his paper, Tan (2000) suggested that star formation could be initiated by collisions between GMCs, providing a natural connection between the local star formation collapse and the global environment of the disc. Using this method, the star formation rate per unit area becomes,

$$\Sigma_{\text{SFR}} = \frac{\epsilon f_{\text{sf}} N_A M_c}{t_{\text{coll}}} \quad (2.16)$$

where $\epsilon = 0.2$, that is the total star formation efficiency, f_{sf} is the fraction of cloud collisions which lead to star formation, N_A is the surface number density of clouds and t_{coll} is the time between collision events. The exact value of f_{sf} is not known, so we select $f_{\text{sf}} = 0.5$, corresponding to 50% of collisions leading to star formation.

The Kennicutt-Schmidt relation from using this triggered star formation scheme is plotted in the bottom panel of Figure 2.11. As with the previous two models, each point represents an average within a 500 pc region, with the star formation rate calculated from the values of N_A and t_{coll} within this volume.

The gradient of the Kennicutt-Schmidt relation is now steeper than unity (index, $N \sim 2$), with a significantly lower star formation rate in the lower density regions. On the one hand, this difference is not surprising, since high density gas leads to many more cloud collisions. However, it is worth noting that taking a constant value for f_{sf} may skew this result; in the bar region, many collisions involve the small *Type C* clouds which are unlikely to trigger significant star formation. A value that reflected the differences between cloud types in merger events would lower the surface star formation rate in the bar region more than in the disc, where the majority of cloud mergers are between *Type A* clouds and likely more productive. Such

	standard	turbulence	cloud collision
$\text{SFE}_{\text{bar}}/\text{SFE}_{\text{disc}}$	2.60	1.05	4.34
$\text{SFE}_{\text{spiral}}/\text{SFE}_{\text{disc}}$	1.42	1.05	1.73

Table 2.2. Ration of the star formation efficiency (SFE) in the bar and spiral environments compared to that in the disc. Results from the three star formation models discussed in section 2.3.4 are shown.

a change would support M83 observations by Hirota et al. (2014), who finds that the star formation rate is elevated in the bar and spiral regions compared to the inter-arm gas, but that the bar region shows a lower star formation rate than the spiral arms. This result is found despite the molecular gas surface density being approximately constant through both the bar and spiral. If collisions drive star formation but are less productive in the bar, this would explain such a result. Additionally, observations of cloud-cloud collisions that result in star formation activity typically have a high relative velocity of 10-20 km/s (Furukawa et al., 2009; Ohama et al., 2010), a result supported in simulations by Takahira et al. (2014) who found that both cloud size and relative velocity were important factors in the formation of stellar cores. Therefore, while Tan (2000)’s model is successful in producing a clear correlation between the surface star formation rate and gas surface density, a more detailed scheme which takes into account cloud differences might yield an even stronger result.

The star formation efficiency ($\text{SFE} = \Sigma_{\text{gas}}/\Sigma_{\text{SFR}}$) from each of these three methods is compared in Table 2.2 with respect to the value in the disc. The SFE that is based simply on gas density (standard model, section 2.3.4) increases by a factor of 1.5 in the spiral region and 2.6 in the disc. On the other hand, the interaction based SFE (cloud collision, section 2.3.4) shows an increase of 1.73 in the spiral and 4.34 in the disc. This simple calculation dramatically shows the main difference between the bar, spiral and disc environments: while the gas density is higher in the bar and spiral and plays a role in shaping the cloud properties, a more major difference is the frequency of the cloud interactions. Notably, when turbulence is included as with the Krumholz and McKee (2005) model (section 2.3.4), there is no difference in SFE between regions. However, it is unlikely we are resolving the full effect of the cloud interactions on the cloud’s internal structure, which is likely to lead to higher compressible turbulent motion.

Since the star formation rate is too high compared to observations, the SFE is likewise above the observed values. Hirota et al. (2014) finds a SFE for M83 between $0.2 - 2 \text{ Gyr}^{-1}$ for the bar and spiral region. The standard star formation model and turbulent model in sections 2.3.4 and 2.3.4 have a SFE almost a factor of 10 too high (in agreement with their star formation rates), with absolute values of 6.1, 8.7 and 16.0 Gyr^{-1} for the disc, spiral and bar regions respectively in the standard model and roughly 20 Gyr^{-1} for the turbulent model. The cloud collision model agrees well with Hirota et al. (2014)’s observations in the spiral, with a $\text{SFE} = 2.7 \text{ Gyr}^{-1}$. However, it is markedly too high in the bar region at 4.34 Gyr^{-1} , due to the reasons discussed above regarding the likely productivity of small cloud collisions.

2.4 Numerical dependences

2.4.1 The effect of resolution

The results presented in section 2.3 show the existence of three types of GMCs: the regular *Type A* clouds, the *Type B* giant molecular associations and the transient *Type C* clouds. A key question therefore is whether these three different types can be observed in real galaxies.

One of the controlling factors in both observational and simulation results is that of resolution. We therefore compared the cloud properties presented in section 2.3 with those found in two simulations performed at lower resolution. The comparison of the cloud property distributions at the three resolution limits is shown in Figure 2.12. The distributions are plotted for all the clouds in the galaxy with the three lines indicating the limiting resolution (smallest cell

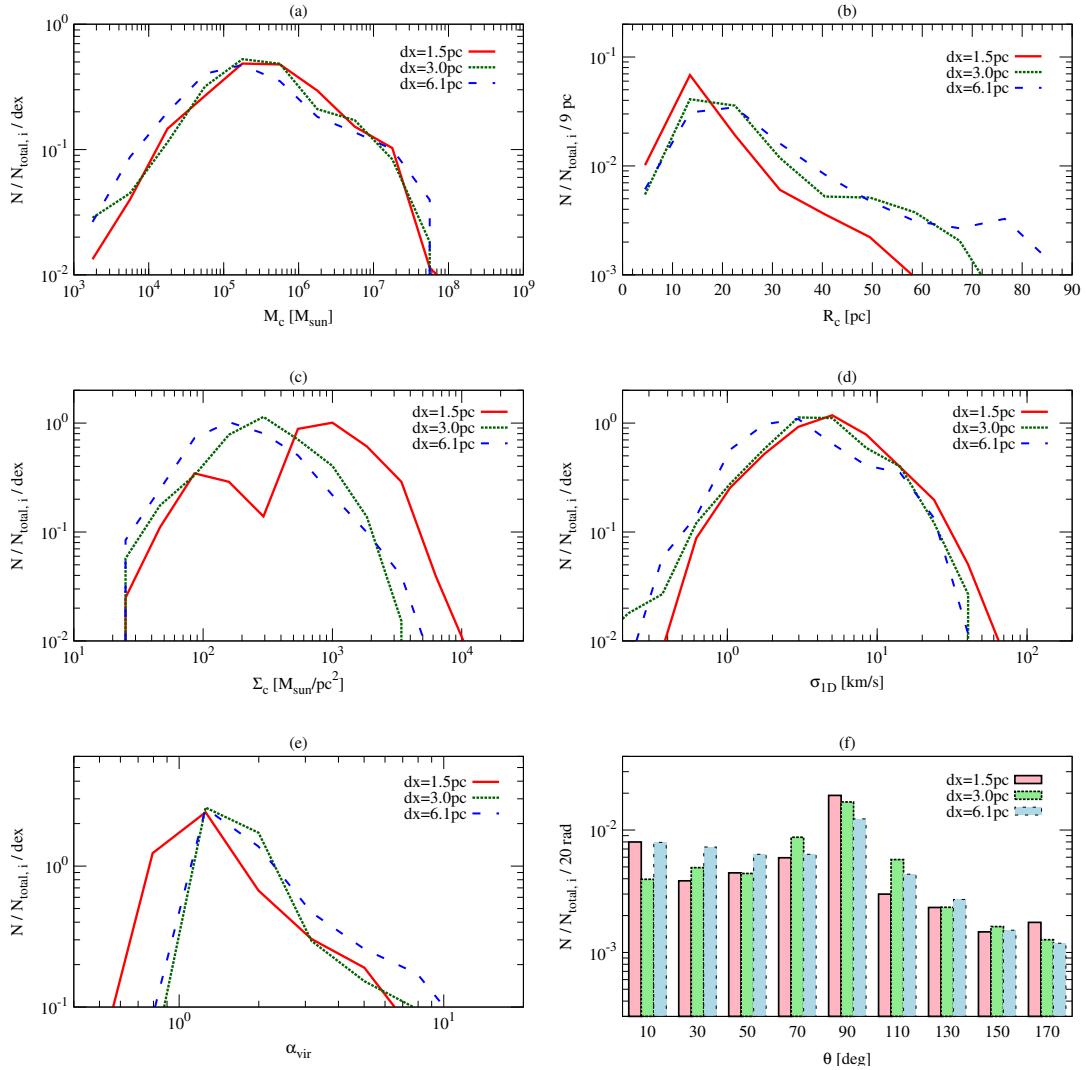


Figure 2.12. Comparison of the cloud property distributions at three different resolutions. For each case, the smallest cell size in the simulation is $\Delta x = 1.5$ pc (red solid line), $\Delta x = 3.0$ pc (green dotted line) and $\Delta x = 6.1$ pc (blue dashed line). The distributions shown are (a) cloud mass, (b) average cloud radius, (c) cloud surface density, (d) cloud 1D velocity dispersion, (e) the virial parameter and (d) the angle of the cloud's angular momentum vector with respect to that of the disc. All properties are calculated as they were for Figure 2.6.

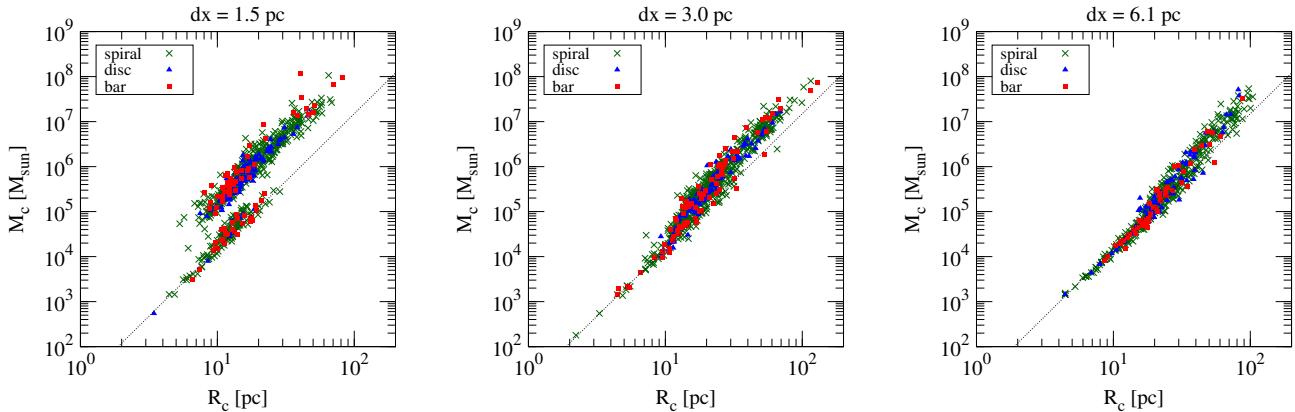


Figure 2.13. Mass versus radius scaling relation for simulations performed at different resolutions. From left to right, the smallest cell in the simulation volume is $\Delta x = 1.5$ pc, $\Delta x = 3.0$ pc and $\Delta x = 6.1$ pc. The markers designate the same galactic regions as in Figure 2.7, with red squares showing bar clouds, blue triangles marking disc clouds and green ‘x’ labelling spiral clouds. The dotted line is the fit ($M_c = 15 \times R_c^3$) for *Type C* clouds which form the lower sequence at our highest resolution ($\Delta x = 1.5$ pc).

size in the volume) of the simulation. The red solid line is our main simulation, with a limiting resolution of $\Delta x = 1.5$ pc. The green dashed line shows the results for a run with one less level of AMR, giving a limiting resolution of $\Delta x = 3.0$ pc. The blue dashed line marks our lowest resolution simulation with $\Delta x = 6.1$ pc.

The cloud mass (Figure 2.12(a)) and cloud velocity dispersion (Figure 2.12(d)) distributions show very little difference between the three resolutions. This is true even at low masses, where the clouds become more difficult to resolve. However, there is a difference at low cloud radii, where our main highest resolution simulation produces a greater proportion of clouds with $3 < R_c < 15$ pc. At lower resolutions, the clouds blend to become extended structures with radii out past 60 pc. This has a very notable effect on the cloud surface density (Figure 2.12(c)), where the second population of clouds with $\Sigma_c > 230 M_\odot/\text{pc}^2$ is entirely missing at the two lower resolutions, removing the bimodality. The larger radii also impacts the virial parameter (Figure 2.12(e)), with cloud typical value moving from $1.0 \rightarrow 1.5$ for the two lower resolution cases. The effect on the angular momentum angle, θ , in Figure 2.12(f) is small overall, showing similar proportions of prograde and retrograde clouds at all resolutions.

The removal of the bimodality in the surface density profile at lower resolutions can be seen clearly in the mass-radius relation. Figure 2.13 shows the same plot at the three different resolution limits. Only in our highest resolution case (left) is the upper and lower trend clearly visible. As we progress to lower resolution, the *Type A* and *Type B* clouds in the upper trend increase in radius, pushing their relation to the right on the plot. The result is a continuous sequence for all cloud types with a more uniform surface density around $\sim \Sigma_c = 200 M_\odot/\text{pc}^2$. This effect could mean that observations are unable to differentiate between *Type A* and the transient *Type C* clouds unless they are at very high resolution.

2.4.2 Comparison between cloud identification methods

The exact definition of a GMC is unclear both in theory and observation. Generally, cloud identification schemes use a density threshold to arbitrate where the edge of a cloud should be, but even here there are multiple permeations. Observers cloud find in surface density space or using position-position-velocity data while theorists prefer to use volume density, rather than selecting a viewing angle for their simulation. There is then the question of when an extended body should be considered multiple clouds, with the answer depending both on resolution and the researcher’s choice.

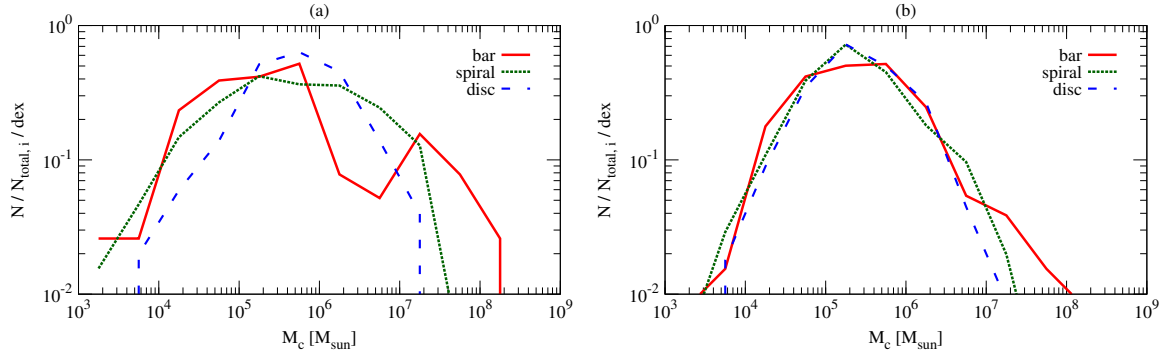


Figure 2.14. The cloud mass distribution as calculated by the two different cloud identification schemes mentioned in section 2.2.3. Left figure shows our original *contour method* where clouds are identified as continuous structures within a density contour at $n_{\text{H},c} = 100 \text{ cm}^{-3}$. Right figure shows the results from the *peak method* where clouds are formed by assigning neighbouring cells to a central peak to build a continuous structure of density above $n_{\text{H},c} > 100 \text{ cm}^{-3}$.

To assess the impact of the choice of cloud definition on our results, we compared cloud properties found using the two identification schemes described in section 2.2.3. The main difference between the two methods is how peaks within a continuous density structure are treated. Our main *contour method* treats these as single cloud, while the *peaks method* divides the cloud if the peaks are more than 20 pc apart (the typical size for a GMC).

This difference in methodology produces a large variation in the number of clouds. When using the *contour method*, we find 77 clouds in the bar region, 515 in the spiral and 102 in the disc at 240 Myr. The *peak method* run on the same output locates 336 clouds in the bar, 1538 in the spiral and 229 in the disc. Unsurprisingly, it is the bar and spiral regions that display the biggest differences in cloud number, with the tidal interactions around the giant *Type B* clouds being subdivided by the *peak method* into multiple bodies.

Despite the difference in cloud number, most features in the cloud properties closely coincide. The peak values for the quantities shown in Figure 2.6 are the same with an overall comparable range of values. The bimodality of the mass-radius scaling relation is also seen with the *peak method*, although the number of smaller clouds within a larger body increases the scatter. However, the distinct population of *Type B* GMAs is not seen in the mass distribution when using the *peak method*. Figure 2.14 shows the mass distribution for the *contour method* (left) and *peak method*. As mentioned above, the peak mass for the clouds is the same in both cases and the range in values is similar, but the bar clouds show no bimodality in the lower distribution. The fact these *Type B* GMAs exist in the data is visually seen in Figure 2.10, but their irregular tidal tails produce a multitude of peaks that are broken up into separate smaller clouds by the *peak method*.

While neither technique is ‘right’ or ‘wrong’ (since there is no established way to define a GMC), it is harder to discern the environmental differences when using the *peak method*, since it tends to produce a more uniformly sized cloud populations in regions of intense interaction. This is also felt to a smaller extent in the comparison of the mass range in the bar and spiral. For the *peak method*, the distributions show only a small difference at the high mass end, but the *contour method* shows more clearly that the spiral region has a wider spread of cloud masses.

This comparison suggests that the choice in cloud identification scheme may not be important in determining the broad cloud properties but may make a significant difference when exploring the finer details such as the difference between environmental regions.

2.5 Conclusions

We performed three-dimensional hydrodynamical simulations of a barred spiral galaxy down to a limiting resolution of 1.5 pc and compared the properties of the GMCs forming in the bar, spiral and disc environments. Our main results are as follows:

1. The typical (peak) value of the cloud properties such as mass, radius and velocity dispersion, is independent of galactic environment. The values found agree well the GMC observation in the Milky Way and nearby galaxies, having a typical mass of $5 \times 10^5 M_{\odot}$ and radius 11 pc (Figure 2.6). This is despite having no active star formation or feedback in the simulation.
2. The high-end tail in the mass, radius, surface density, velocity dispersion and virial parameter shows a clear relation to the galactic environment, with the pattern being bar \rightarrow spiral \rightarrow disc for the regions most likely to host clouds with extended structures.
3. Clouds in the bar region display a bimodality in the mass, radius and velocity dispersion distributions that is not visible in the spiral or disc regions. This is due to the formation of GMAs, which build mass $> 10^7 M_{\odot}$ through multiple mergers with other clouds. Since the bar is a densely packed region of clouds in close-passing elliptical orbits, the fraction of GMAs is greatest in this environment, producing the bimodal distributions.
4. All environments show a bimodal surface density distribution. This corresponds to two parallel trends on the mass-radius scaling relation. The lower trend is formed of transient, unbound clouds that are created in the tidal tails and filaments surrounding more massive clouds. (Figures 2.6, 2.8, 2.10).
5. Based on the distribution results above, clouds can be classified into three types: *Type A* are the most common cloud, forming the largest population in all three environments. Their properties agree well with GMCs observed in other galaxies. *Type B* are massive GMAs, formed via mergers with smaller clouds and most prominent in high interaction environments. *Type C* clouds are unbound, transient objects formed in the dense filaments and tidal tails surrounding other clouds. They usually merge or dissipate within a few Myr, although can live for longer if unperturbed. (Figures 2.8, 2.9)
6. The main difference between galactic environments is not the properties of a typical cloud born in each region, but the ratio of the above three cloud types. The determining factor in this ratio is the level of interactions between the GMCs. *Type B* and *C* clouds are formed during cloud collisions, with *Type B* being the product of multiple mergers and *Type C* forming most frequently in the dense filamentary structures that surround such encounters. The bar region has the highest rate of cloud mergers and also the largest number of *Type B* and *C* clouds. The spiral region is the next most interactive while the disc is the most quiescent, leading to a cloud population that is predominantly *Type A*. (Table 2.1, Figure 2.9).
7. Lower resolution simulations blur the distinction between the three cloud types, due to *Type A* and *Type B* clouds having larger radii at lower resolutions. Linked with this, the cloud identification scheme can also affect separating cloud types. The cloud peak properties and range of values are preserved between two different cloud finding algorithms run on our simulation, but the scheme which splits density peaks in close proximity to one another fails to identify the *Type B* GMAs. This needs to be considered when comparing populations of clouds in observational and simulation data.

Although we successfully reproduce many of the properties of observed GMCs, the question of impact from stellar feedback is not addressed in our simulations. On our limited resolution

scale of 1.5 pc, the effect of feedback is especially interesting (with the outcome of feedback affecting our results or not both being of equal importance). This topic will be the subject of future work.

Chapter 3

Environmental dependence of star formation induced by cloud collisions in a barred galaxy

Cloud collision have been proposed as a way to link the small-scale star formation process with the observed global relation between the surface star formation rate and gas surface density. We suggest that this model can be improved further by allowing the productivity of such collisions to depend on the relative velocity of the two clouds. Our adjustment implements a simple step function that results in the most successful collisions being at the observed velocities for triggered star formation. By applying this to a high resolution simulation of a barred galaxy, we successfully reproduce the observational result that the star formation efficiency (SFE) in the bar is lower than that in the spiral arms. This is not possible when we use an efficiency dependent on the internal turbulence properties of the clouds. Our results suggest that high velocity collisions driven by the gravitational pull of the clouds are responsible for the low bar SFE.

3.1 Introduction

Recent studies of galactic-scale star formation have revealed that the rate at which stars are produced depends on the galactic environment. Global structures within a galaxy result in changes to the star formation rates (SFR), even when the gas surface density is almost the same. In observations of disc galaxies, the star formation efficiency ($SFE = \Sigma_{\text{SFR}}/\Sigma_{\text{gas}}$) is found to vary between the nucleus and disc region (Muraoka et al., 2007), and between the arm and inter-arm (Muraoka et al., 2009b; Hirota et al., 2014).

High resolution (~ 250 pc) $^{12}\text{CO}(J = 1 - 0)$ observations of the barred galaxy M61 (NGC 4303) by Momose et al. (2010), showed that the SFE in the bar is 50 % of that in the spiral arms. Previous studies have suggested that this drop is due to strong shear along the bar that provides a turbulence injection to support the giant molecular clouds (GMCs) (Tubbs, 1982; Athanassoula, 1992; Downes et al., 1996; Reynaud and Downes, 1998; Sorai et al., 2012; Meidt et al., 2013). However, there is counter evidence suggesting that the role of shear is too small to be consequential to the evolution of the GMCs. For clouds in our own Galaxy, Dib et al. (2012) found that shear is consistently a fraction of the value needed to disrupt a density perturbation, and thereby does not affect star formation.

A way to resolve this disparage is to use simulations, yet here too there is disagreement. In two-dimensional models of the barred galaxy M83, Nimori et al. (2013) found that the SFE in the bar region was 60 percent of the spiral arm due to the strong internal turbulence of the clouds. Conversely, more recent 3D models of the same galaxy performed by Fujimoto et al. (2014a), found that the typical internal cloud velocity dispersion showed little variation

between clouds forming in the bar, spiral arm and disc. This implied shear might not be the key to understanding the varying star formation rate. Yet, the situation is complicated by the SFE being highly dependent on the stellar model used.

Fujimoto et al. (2014a) did not include active star formation, but estimated the SFE based on the gas properties. There are multiple methods for doing this, each based on assumptions as to what governs the production of stars. Two methods used by Fujimoto et al. (2014a) compared a scheme utilising the internal properties of the cloud with one that considered star formation driven by cloud interactions. The former was proposed by Krumholz and McKee (2005) and assumed that clouds are supersonically turbulent with a log-normal density distribution. By demanding that gas collapses when the gravitational energy within a cloud exceeds its turbulent energy, they find the SFR per cloud is:

$$\text{SFR}_c = \epsilon_{\text{ff}} \left(\frac{\alpha_{\text{vir}}}{1.3} \right)^{-0.68} \left(\frac{\mathcal{M}}{100} \right)^{-0.32} \frac{M_c}{t_{\text{ff}}} \quad (3.1)$$

where the star formation efficiency per free-fall time, $\epsilon_{\text{ff}} = 0.014$, the virial parameter $\alpha_{\text{vir}} = 5\sigma_c^2 R_c / GM_c$, properties R_c , M_c and σ_c are the cloud radius, mass and 1D velocity dispersion, the Mach number is the ratio between the cloud's velocity dispersion and the sound speed, $\mathcal{M} \equiv \sigma_c / c_s$, and t_{ff} is the cloud free-fall time.

The second scheme assumes that star formation is initiated by collisions between clouds. Such interactions can trigger a shock at the collision interface which fragments into stars. This has been suggested as a way to unite the local star formation process with the globally observed Kennicutt-Schmidt relation (Tan, 2000; Tasker and Tan, 2009; Kennicutt, 1998) and also as a mechanism to create massive stars and super star clusters (Takahira et al., 2014; Fukui et al., 2014; Dib et al., 2013; Furukawa et al., 2009; Ohama et al., 2010; Habe and Ohta, 1992). Since there is evidence that clouds may be gravitationally unbound (Heyer et al., 2009; Dobbs et al., 2011a), cloud collisions could be the best candidate to create the dense regions where stars are formed. In the shock-generating model proposed by Tan (2000), the surface density of the SFR becomes:

$$\Sigma_{\text{SFR}} = \frac{\epsilon f_{\text{sf}} N_A M_c}{t_{\text{coll}}} \quad (3.2)$$

where $\epsilon = 0.2$ is the total fraction of cloud gas converted to stars during a star-forming collision, f_{sf} is the fraction of cloud collisions which successfully lead to star formation, N_A is the surface number density of clouds, M_c is the cloud mass and t_{coll} , the typical time between collisions.

Fujimoto et al. (2014a) found that neither of these models produced the observed lower SFE in the bar region. With the turbulence model in Eq. 3.1, the SFE was equal in the bar and spiral arms, while the cloud collision model in Eq. 3.2 gave a higher SFE in the bar than the arms. The first of these was consistent with the result that the typical cloud properties were not dependent on cloud environment. The cloud collision model reflected the fact that the collision rate was highest in the densely packed bar environment, leading to a higher star formation rate. In this case, the difference in the galactic environment produced the opposite effect to that in observations, but this might have been due to a simplification made in Eq. 3.2.

The cloud collision model assumes that all collisions are equally likely to produce star formation. The fractional success rate, f_{sf} , is taken to be constant whose value was selected to be 0.5 in Fujimoto et al. (2014a). This approximation is known to be inaccurate. In observations of triggered star formation in cloud collisions by Fukui et al. (2014); Ohama et al. (2010); Furukawa et al. (2009), the formation of super star clusters was found to be associated with collisional velocities around 20 km/s. This was investigated in simulations by Takahira et al. (2014), who found that the production of star-forming cores in a collision strongly depended on the relative velocity of the two clouds. A slow collision would not produce a shock strong enough to create a dense region at the cloud interface while too fast a collision would result

in the shock front exiting the cloud before a core had time to form. The value of f_{sf} should therefore depend on the relative velocity of the colliding clouds.

To be strictly accurate, the values for f_{sf} and ϵ are not independent. If f_{sf} depends on velocity, then a prime velocity for production of stars is going to produce a higher efficiency. However, for the sake of simplicity, we consider ϵ to represent the average conversion efficiency and assume only f_{sf} varies. We keep the value of ϵ suggested in Tan (2000) as 0.2.

In this chapter, we calculate the SFE in the barred galaxy model of Fujimoto et al. (2014a) using a revised version of the cloud collision star formation scheme in Eq. 3.2, accounting for variations in stellar production due to the collisional velocity of the clouds. We compare the results in different galactic regions of the simulation with those in observations.

3.2 Simulation

The simulation presented in this chapter was run using *Enzo*: a 3D adaptive mesh refinement (AMR) hydrodynamics code (Bryan et al., 2014). Our galaxy was modelled on the nearby barred spiral galaxy, M83, with the gas distribution and stellar potential taken from observational results. For the galaxy’s radial gas distribution, we assumed an initial exponential density profile based on the observations of Lundgren et al. (2004b) and used fixed-motion star particles to create a stellar potential with the observed pattern speed for M83.

The GMCs in our simulation were identified as coherent structures contained within contours at a threshold density of $n_{\text{H,c}} = 100 \text{ cm}^{-3}$, similar to the observed mean volume densities of typical galactic giant molecular clouds. The simulation outputs were analysed every 1 Myr and the clouds mapped between consecutive times. This cloud tracking algorithm is described in Tasker and Tan (2009). A collision is said to have happened when a single cloud is at the predicted position for two other clouds after 1 Myr of evolution. It is a lower estimate of the true cloud interaction rate, since it does not include tidal shredding where two identifiable objects exist at the end of the encounter.

After 120 Myr (one pattern rotation period), the gas is fully fragmented, and between 200 Myr and 280 Myr, the galactic disc settles into a quasi-equilibrium with no large structural change. We analysed the clouds at 240 Myr.

We assigned an environment group based on the cloud’s physical location within the disc. If a cloud is found within the galactic radii $2.5 < r < 7.0 \text{ kpc}$, it is recognised as a spiral cloud. Outside $r = 7.0 \text{ kpc}$, clouds are designated disc clouds. Bar clouds form in a box-like region at the galactic centre, with a length of 5.0 kpc and width 1.2 kpc. The nucleus region inside 600 pc is excluded due to the difficulty in accurately tracking clouds in such a high density area. The boundaries of these three regions are shown in Figure 5 of Fujimoto et al. (2014a), along with a more thorough description of the simulation.

3.3 Results

3.3.1 Environmental dependence of collision velocity

In order to determine whether collision velocity is likely to play a role in the productiveness of triggered star formation, we looked at the range of values present in the simulation. Figure 3.1 shows the collision velocity distribution in each of our three galactic region. This was calculated from the relative velocity of the clouds 1 Myr prior to their merger, $v_{\text{coll}} = |\vec{v}_1 - \vec{v}_2|$, where \vec{v}_1 and \vec{v}_2 are the bulk velocities of the clouds. Since the number of collisions occurring in a 1 Myr output interval is small, we included all collisions occurring between $t = 230 - 240 \text{ Myr}$, during the quiescent period of the disc’s evolution.

The collision velocity shows a clear dependence on the galactic environment. The bar region has the widest range, extending out to 120 km/s with only a small peak in the distribution around 35 km/s. By contrast, the spiral region has a steeped profile with a typical collision

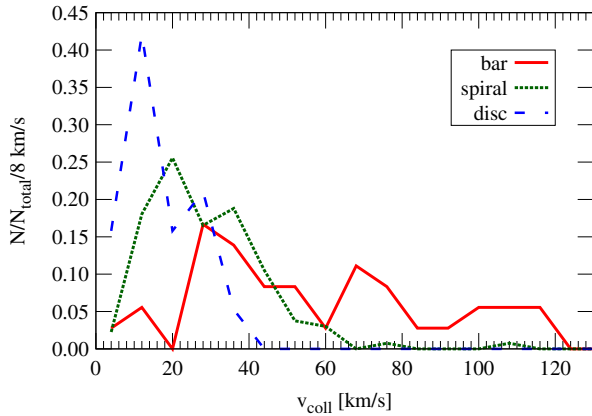


Figure 3.1. Distribution of the collision velocity of clouds colliding in the bar region (solid red line), spiral region (dotted green line) and disc region (dashed blue line). The collision events are counted for 10 Myrs from $t = 230$ Myr to 240 Myr.

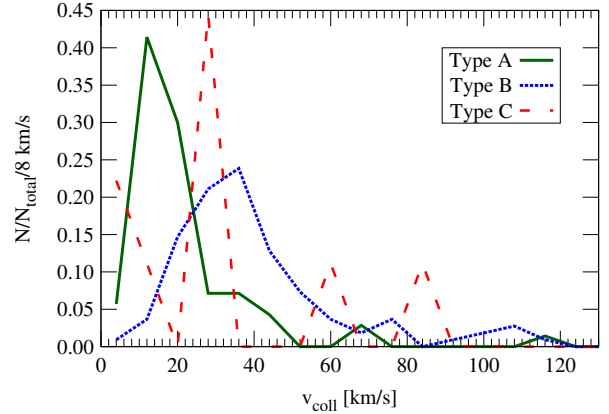


Figure 3.2. Distribution of the collision velocity for three cloud categorisations: *Type A* (solid green line) are the most common clouds with properties typical of observed GMCs, *Type B* (dotted blue line) are massive associations and *Type C* (dashed red line) are unbound, transient clouds. The cloud type plotted is that of the most massive cloud involved in the collision.

speed of 20 km/s and clouds rarely colliding faster than 60 km/s. In the disc region, interactions are more gentle with a collision speed peaking at only 15 km/s and a maximum of 40 km/s.

By virtue of its area, the total number of cloud collisions is highest in the spiral region. However, the fraction of clouds undergoing a collision event is higher in the bar, due to the constrained elliptical motion. This bolstered rate of interaction alters the properties of the clouds, allowing much larger structures to be built through successive mergers. The result is a group of Giant Molecular Associations (GMAs) that dominate the local gravitational field, pulling clouds onto a collision course that increases their relative velocity.

That the collision velocity can be attributed to properties of the cloud population can be seen clearly in Figure 3.2. The collision velocity is now plotted for three different types of cloud, categorised by their mass and radius. *Type A* clouds form the main population in the disc. Their properties are consistent with observed GMCs with masses $\sim 5 \times 10^5 M_\odot$ and radii ~ 11 pc. *Type B* clouds are the giant GMAs with masses above $10^6 M_\odot$. *Type C* clouds are unbound objects that have short lives in filaments and the tidal tails of larger interacting clouds. The cloud type was determined using the mass-radius relation described in detail in Fujimoto et al. (2014a) and the collision cloud type is dictated by the largest object of the interacting pair, resulting in a low number of *Type C* with a noisy distribution. These distributions show that collisions involving a GMA *Type B* cloud are faster. The speed peaks around 40 km/s and extends to beyond 100 km/s. By contrast, a typical collisions with a *Type A* cloud occurs at half the speed of those with *Type B*. This fast interaction speed for the *Type B* is consistent with their escape velocity, which ranges between 17 – 100 km/s for the clouds with masses between $10^6 - 10^8 M_\odot$ and radii 30 – 100 pc. The *Type B* clouds form a dominant population in the bar as shown in Table 3.1. Half the clouds in the bar are either *Type B* or the small *Type C* forming in the interaction tails of the *Type B*. The spiral and disc region have a stronger population of *Type A* clouds, with the disc having less than 6% *Type B*. The *Type B* clouds therefore govern the interactions in the bar, producing a higher collision speed than either the spiral or the disc. This supports the idea that the variation in SFE with galactic region might be due to a variation in the efficiency of triggered star formation.

3.3.2 Environmental dependence of SFE

To equate the cloud collision rate to a star formation rate, we used the model proposed by Tan (2000) in Eq. 3.2 to plot the observed Kennicutt-Schmidt relation between the surface star

	Bar	Spiral	Disc
Type A	49.4% (38/77)	64.1% (330/515)	83.3% (85/102)
Type B	13.0% (10/77)	12.8% (66/515)	5.9% (6/102)
Type C	37.7% (29/77)	23.1% (119/515)	10.8% (11/102)

Table 3.1. The percentage of each cloud type in each galactic region at $t = 240$ Myr. Bracketed numbers show the actual number of clouds of that type divided by the total cloud number in the region.

v_{coll}	$0 \sim 10$ km/s	$10 \sim 40$ km/s	40 km/s \sim
f_{sf}	0.05	0.5	0.05

Table 3.2. The fraction of collisions that result in star formation, f_{sf} , for different collision velocities, v_{coll} .

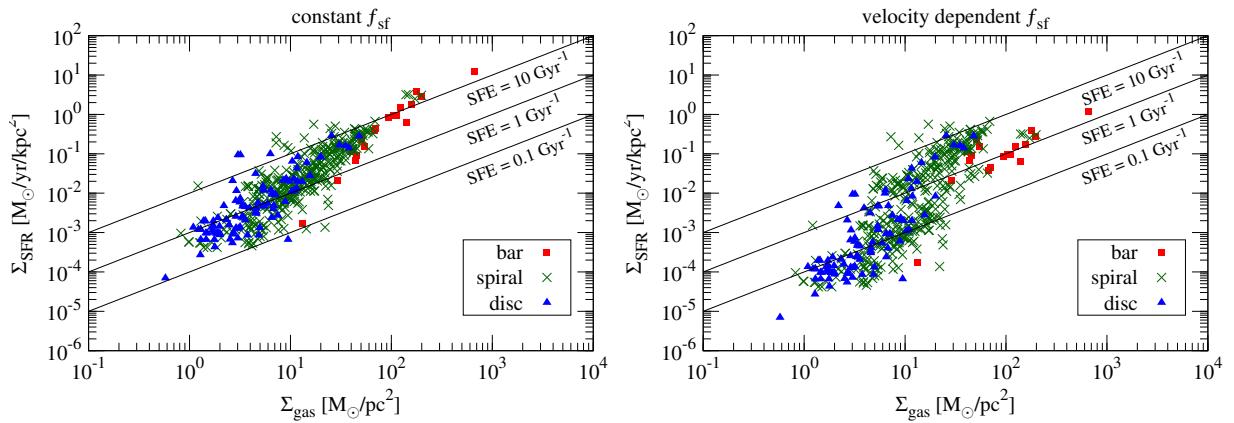


Figure 3.3. Relation between gas surface density and SFR surface density. The SFR is estimated by the cloud collision model depending on the average collision velocity in $500 \text{ pc} \times 5 \text{ kpc}$ cylindrical regions. The left panel uses a constant f_{sf} while the right panel uses the collision velocity dependent f_{sf} , as described in Table 3.2. The coloured markers denotes different galactic regions: red squares are clouds in the bar region, green \times are for the spiral region and blue triangles are those in the disc region. The black dotted lines show constant SFEs = 10, 1, 0.1 Gyr^{-1} .

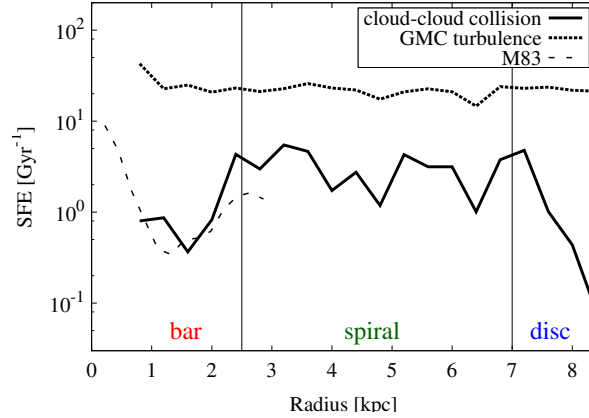


Figure 3.4. Azimuthally averaged (bin size 400 pc) radial distributions of the SFE estimated by the velocity dependent cloud collision model (solid line), the cloud turbulence model (dashed line) and from observations of M83 by Hirota et al. (2014) (wide dashes). The vertical lines show the borders of galactic regions: $600\text{pc} < r < 2.5\text{ kpc}$ marks the bar region, $2.5 < r < 7.0\text{ kpc}$ is the spiral region, and $r > 7.0\text{ kpc}$ is the disc region.

formation rate density and surface gas density. We calculated the surface area in the $x - y$ plane (face-on disc) and averaged the data over cylindrical regions with height 5 kpc and radii 500 pc, in keeping with the typical observational resolution. If we assume a constant fraction of all collisions lead to star formation with $f_{\text{sf}} = 0.5$ in Eq. 3.2, we get the Kennicutt-Schmidt relation in the left-hand panel of Figure 3.3. The SFE is proportional to the frequency of collisions, with the bar having the highest number of cloud collisions and therefore the highest efficiency.

In order to take into account the dependence of f_{sf} on the collision velocity, we use the step function described in Table 3.2. Since observations of triggered star formation found a collision velocity around $\sim 20\text{ km/s}$ (Fukui et al., 2014; Furukawa et al., 2009; Ohama et al., 2010), we assume that collisions between $10 - 40\text{ km/s}$ are ideally suited to creating stars and set $f_{\text{sf}} = 0.5$ in this range. This is consistent with the majority of our collisions in Figure 3.1; a necessity since the average SFR is in good agreement with observations (Bigiel et al., 2008). Outside this region, we assume that a collision velocity less than 10 km/s is too slow to form the compressed shock front that leads to efficient star formation while velocities higher than 40 km/s produce interaction times between clouds that are too short to form a high number of stars. Within these ranges, we therefore lower the value of f_{sf} by a factor of 10. Exactly where these cut-off should be and the correct value for f_{sf} requires a further exploration of shock speed and cloud structure, so here we select values that lie within our observed range of velocities and agreed with the observations available.

The result of including this collision velocity dependence is shown in the right-hand panel of Figure 3.3. With a significant fraction of the bar clouds colliding at high velocities with a low success rate, the SFE in this region drops. This produces a lower SFE in the bar than a large fraction of the spiral regions, in agreement with the observations of Momose et al. (2010), where the bar SFE lies in the lower-half of the SFE spread in the spiral. The spiral region shows an increased range of efficiencies due to its broad profile of collision velocities in Figure 3.1 having tails in both our low efficiency regions. Conversely most of the disc clouds collide too slowly for strong star formation, decreasing the efficiency of the majority of these points. This demonstrates that while the cloud collision model for star formation can successfully reproduce the Kennicutt-Schmidt relation, the dependence on the velocity of the interaction introduces an environmental dependence that cannot be ignored.

A second comparison point is the radial distribution of the SFE was measured by Hirota et al. (2014) for the bar region in M83. They found a peak in the SFE at the bar end, corresponding to an efficiency of $\sim 2\text{ Gyr}^{-1}$ which drops to $\sim 0.3\text{ Gyr}^{-1}$ along the bar length. We compared

this to the radial profiles we get using the cloud collision and turbulence models for SFE in Figure 3.4. For star formation estimated from the cloud turbulence in Eq. 3.1, there is no radial dependence and we see a constant efficiency through the three galaxy environments. Using the velocity dependent collision scheme, a clear drop is seen after the bar end of the same magnitude as in the observations.

3.4 Conclusion

We investigated the variation in the relative velocity of cloud collisions in different regions of a simulated galaxy. Using this, we proposed a change to the triggered star formation model developed by Tan (2000) that varied the effectiveness of star formation from cloud collisions based on the speed at which the clouds collide. Taking the observations of triggered star formation as the most successful velocity for forming stars, we varied the fraction of collisions that would result in star formation such that collisions between 10 – 40 km/s were successful 50 % of the time, while collisions slower and faster than this range were only successful 5 % of the time. Our main results are:

- The collision velocity shows a clear dependence on galactic environment. Clouds formed in the bar region typically collide faster than those in the spiral. Clouds in the disc are involved in the gentlest collisions.
- This dependence is due to the distribution of cloud types in the three regions. A higher fraction of bar clouds are massive, creating strong gravitational interactions that increase the collision velocity.
- The unproductive collisions in the bar region lowers the SFE to put it below the maximum efficiency in the spiral region. This is despite collisions being more common in the bar region. The result is in agreement with observations of other barred galaxies.
- When plotted as a radial distribution, the drop in SFE at the bar end is also consistent with observational measurements of M83. This is not reproduced when the SFE is calculated from the cloud turbulence, which shows a constant SFE across all regions.

One area not considered is the effect of stellar feedback. The impact of feedback is a hot topic, with opinions suggesting that it does not affect the GMCs (Renaud et al., 2013) to implying it is a controlling force. In stellar wind models performed by Dib et al. (2013), the SFE in a star-forming clump decreased with clump mass. Such an effect could also explain the lower bar SFE if the larger GMAs resulted in more massive clumps. However, the authors also find that for star clusters thought to be formed in cloud collisions, the best-fit model uses an increasing SFR with time. This is likely to be controlled by the evolution of the collision-induced surface density, which Takahira et al. (2014) demonstrated depends strongly on collision speed. The two effects will therefore work in parallel and further investigation is needed to separate out their contributions.

Chapter 4

Stellar feedback effects on GMCs

We perform M83-type barred spiral galaxy simulations with a thermal stellar feedback at 1.5 pc resolution and investigate impacts of the thermal stellar feedback on interstellar medium (ISM), giant molecular clouds (GMCs) and star formation in the barred galaxy. The stellar feedback disperses some fraction of the gas of clouds into the inter-cloud region, and raises the ISM density surrounding the clouds. The high ISM density affects the GMC's formation and evolution. To understand effects of the stellar feedback on the clouds, we classify all clouds into three types via mass-radius scaling relation, which we label *A*, *B* and *C*. *Type A* clouds have the typical values of cloud properties: mass, radius, 1D velocity dispersion. *Type B* clouds are massive giant molecular associations (GMAs). *Type C* clouds are unbound, transient clouds. The stellar feedback affects a formation of the *type C* small transient clouds. Without the stellar feedback, the *type C* clouds are formed in the dense filaments and tidal tails that are induced by the *type B* massive clouds interactions. With the stellar feedback, the *type C* clouds are formed in the warm ISM, and more *type Cs* are formed compared with no feedback case. Moreover, massive clouds (especially *type B* clouds) lose their specific angular momentum due to a strong drag induced by the high density ISM. The inflows of the massive clouds towards the galactic centre supply a huge amount of the gas to the central bar region. The SFR of the central bar region gets higher when the stellar feedback is included because the high SFR massive clouds (mainly *type B* clouds) drop into the central bar region.

4.1 Introduction

Understanding where and how gas is converted into stars within galaxy is important for many fields of astrophysics. Especially, it fills a gap between a field of large scale galaxy formation and evolution from an early universe to a current era, and small scale star formation processes under molecular cloud core. It has been believed that the gas density is only the factor controlling star formation in a galaxy because observations have shown a scaling relation between the gas density (or gas surface density) and the star formation rate (SFR) (or SFR surface density) by a simple power law, which is known as Kennicutt-Schmidt relation (Schmidt, 1959; Kennicutt, 1989, 1998; Wong and Blitz, 2002; Bigiel et al., 2008; Schrubba et al., 2011). Schmidt (1959) observed solar neighbour star forming clouds and found the scaling relation between them. Kennicutt (1998) observed nearby galaxies and also found the scaling relation between galaxies. Recent observations, however, show that systematic variations exist in the relation between different galaxy types (Daddi et al., 2010b; Genzel et al., 2010; Leroy et al., 2013), the galactic grand design structures (Momose et al., 2010), super giant HII regions (Miura et al., 2014). This systematic variation indicates different star formation efficiency ($SFE = \Sigma_{\text{SFR}}/\Sigma_{\text{gas}}$) between global environments of star formation. They suggest distinct star formation from material simply being gathered to produce a higher star formation rate and imply an existence of the other factors controlling star formation in a galaxy, not only the gas density. Especially, recent observations of nearby galaxies show different SFEs between galactic structures in a galaxy; bar

and spiral arm (M61: Momose et al. 2010, M83: Hirota et al. 2014), arm and inter-arm (M61: Momose et al. 2010), nucleus and disc (M83: Muraoka et al. 2007, M61: Momose et al. 2010). It has still been under debate what physical process control the star formation in a galaxy and why SFE differs between global galactic environments of star formation.

Giant molecular clouds (GMC) are star formation spots in a galaxy, and then they are an important clue for understanding the galactic star formation. They are formed from cold phase of an interstellar medium (ISM), and densest pocket in them are birth place of stars. Properties (e.g. mass, size, and velocity dispersion) of the GMCs control formation of these gravitationally unstable dense clumps and hence determine the rate of star formation in them. Observations of the Milky Way and nearby galaxies have revealed typical GMC properties: Milky Way (Larson, 1981; Solomon et al., 1987; Lada and Blitz, 1988; Dame et al., 2001; Heyer et al., 2009; Roman-Duval et al., 2010), LMC (Fukui et al., 1999, 2001, 2008; Mizuno et al., 2001b; Kawamura et al., 2009; Hughes et al., 2010), SMC (Mizuno et al., 2001a), M31 (Vogel et al., 1987; Lada et al., 1988; Wilson and Rudolph, 1993; Rosolowsky, 2007), M33 (Wilson and Scoville, 1990; Engargiola et al., 2003; Rosolowsky et al., 2003, 2007; Miura et al., 2012; Gratier et al., 2012), M51 (Koda et al., 2009, 2012; Meidt et al., 2013, 2015; Colombo et al., 2014), M64 (Rosolowsky and Blitz, 2005), M83 (Muraoka et al., 2009b), IC 10 (Wilson and Reid, 1991; Leroy et al., 2006), IC 342 (Hirota et al., 2011), NGC 4039 (Espada et al., 2012; Wei et al., 2012), NGC 6822 (Wilson, 1994), NGC 6946 (Rebolledo et al., 2012), Local Group (Blitz et al., 2007; Bolatto et al., 2008; Hughes et al., 2013; Donovan Meyer et al., 2013; Rebolledo et al., 2015). However, it is difficult within our own disc to assess the effects of global galactic structures, and extragalactic data are limited by resolution, which makes it hard to assemble large enough samples of GMCs to explore the dependence on internal galactic structures. In theoretical works, it has become possible to investigate formation and evolution of individual GMC using hydrodynamical isolated galaxy simulations thanks to developments of super computer and effective algorithms (Dobbs et al., 2006, 2011b; Tasker and Tan, 2009; Renaud et al., 2013; Benincasa et al., 2013; Fujimoto et al., 2014a; Williamson et al., 2014; Tasker et al., 2015; Khoperskov et al., 2015).

Galactic structures affect GMC distributions and properties. Fujimoto et al. (2014a) (hereafter Paper I) performed hydrodynamical simulations of the barred galaxy M83 and found that distributions and properties of GMCs differ between galactic environments: bar, spiral arms, outer disc regions. Higher cloud density due to an elliptical gas motion caused by bar and spiral potential increases cloud interaction rates and changes GMC distributions and properties between the galactic regions. Cloud-cloud collision can form high density shocked region at the collisional interface and triggers massive star formation (Theories: Habe and Ohta 1992; Anathpindika 2010; Inoue and Fukui 2013; Takahira et al. 2014. Observations: Loren 1976; Dickel et al. 1978; Odenwald et al. 1992; Furukawa et al. 2009; Ohama et al. 2010; Fukui et al. 2014). Fujimoto et al. (2014b) pointed out that faster and more destructive cloud-cloud collisions in the bar region induce the lower SFE than that in the spiral arm region, which is consistent with observational results in the barred galaxy M61 (Momose et al., 2010). Dobbs et al. (2006) performed hydrodynamical simulations of a isolated spiral galaxy and found a dependence on GMC properties with grand design spiral arms, with clouds leaving the spiral arms to be sheared and form inter-arm feathering. Renaud et al. (2013) found more compact inter-arm spurs due to Kelvin-Helmholtz instabilities forming down the side of the spiral arms. Although there are a few observations which investigates the impact of galactic structures on GMCs, Koda et al. (2009) observed spiral galaxy M51 and found cloud assembling in the spiral arm, forming giant molecular associations and leaving smaller clouds into the inter-arm region. Meidt et al. (2013) and Colombo et al. (2014) observed the same galaxy and found that shearing flows and shocks driven by the spiral arms stabilise GMCs, and that changes the shape of the cloud mass distributions between the galactic environments. Hirota et al. (2011) observed the intermediate spiral galaxy IC342 and found GMCs that are associated with star forming regions are located downstream of the spiral arm and are more massive and closer to virial equilibrium.

Paper I missed effects of stellar feedback on GMCs. The new formed star emits UV radiation and stellar winds, and forms HII region due to ionisation of the ISM by the UV radiation from the centre star. The radiation pressure, stellar winds and thermal pressure of the HII region inputs momentum to the ISM around it. Moreover, massive star larger than $8 M_{\odot}$ ejects huge energy ($\sim 10^{51}$ ergs) into the ISM as supernova in the end of its life. The supernova remnant evolves into four stages: free expansion, adiabatic expansion, pressure driven snowplough and momentum conserving phases. In the adiabatic expansion phase, which is known as Sedov-Taylor phase, the input energy from supernova is distributed into the ISM as thermal and kinetic energy of the gas (Sedov, 1959; Taylor, 1950). These stellar feedback processes extends large range of spatial and time scales, and many fields of astrophysics investigate effects of the stellar feedback. In the galactic star formation field, Tasker et al. (2015) performed Milky Way type disc galaxy simulations with thermal energy input from supernova. They found that the feedback suppress the star formation, but they does not destroy the surrounding GMCs. Shetty and Ostriker (2008) got similar results performing two dimensional galactic disc simulations with momentum injection. Hopkins et al. (2011, 2012) also performed isolated galaxy simulations with not only supernova feedback but also stellar winds, radiation pressure from stellar photon and HII photoionization heating. They found that the stellar feedback regulates star formation rate in the galactic disc, and the star formation rate is good agreement with the observed Kennicutt-Schmidt relation with independence of numerical star formation and feedback parameters. Grand design spiral galaxy simulations performed by Dobbs et al. (2011b) with thermal and kinetic energy feedback from supernova also found the self-regulated star formation by the feedback. They also investigated the effects of the spiral arm on GMC, and still found the accumulation of massive GMCs in the spiral arms, that are similar results to no stellar feedback simulation (Dobbs et al., 2006). Whether the galactic environment effects on GMCs exist even when the stellar feedback processes are included is still unknown because few previous works investigated it.

In this chapter, we perform barred spiral galaxy simulations with thermal energy input from supernova at 1.5 pc resolution and investigate the impact of galactic structures (bar and spiral arms) and supernova feedback on the ISM, GMCs and star formation. We model the barred galaxy M83, which is a nearby face-on galaxy and a target object in ALMA projects in Cycle 0, 1, 2; we expect to compare our results with GMC observations with high spatial resolution done by ALMA. We consider only thermal energy feedback from supernova as a first step. The other stellar feedbacks remain to be done as future works. We present our study as follows; in Section 4.2, we present our simulation model of the barred galaxy, especially star formation and stellar feedback model. In Section 4.3, we show that our only thermal stellar feedback does effect on the ISM, GMC properties and star formation. In Section 4.4, we discuss the stellar feedback effects using analytical estimation of cooling time of the feedback energy. Section 4.5 presents our conclusions.

4.2 Numerical methods

4.2.1 Simulation and initial conditions

The isolated galaxy simulation presented in this chapter was run using Enzo: a 3D adaptive mesh refinement (AMR) hydrodynamics code (Bryan et al., 2014). We used a three-dimensional box of side 50 kpc with a root grid of 128^3 cells and 8 levels of refinement, giving a limiting resolution (smallest cell size) of about 1.5 pc. The cell was refined into eight cells whenever the mass included in the cell exceeded $1000 M_{\odot}$. The evolution of the gas was performed using a three-dimensional version of the ZEUS hydrodynamics algorithm (Stone and Norman, 1992). ZEUS uses an artificial viscosity as a shock-capturing technique with the variable associated with this, the quadratic artificial viscosity, set to the default value of 2.0. The gas was self-gravitating and allowed to cool radiatively down to 300 K. The radiative cooling used rates from

the analytical expression of Sarazin and White (1987) for solar metallicity down to 10^5 K, and continued to 300 K with rates provided by Rosen and Bregman (1995). An artificial pressure support is implemented to prevent unresolved collapse at the finest cell (Machacek et al., 2001). In detail, the thermal energy of the finest cell is replaced with the gravitational self-energy of the gas, which spreads the mass over a spherical region with radius of four cells. This pressure support results in a $\gamma = 2$ polytrope, $P \propto \rho^\gamma$, of the finest cell. The star formation and feedback are included, detailed in Section 4.2.2.

Our galaxy was modelled on the nearby barred spiral galaxy, M83. For a stellar potential, we used a potential model done by Hirota et al. (2014), who analysed the 2Mass K -band image of M83. The stellar potential is composed of two main parts that are an axisymmetric part and a non-axisymmetric part to produce the bar structure and the spiral arms of M83. To allow a more accurate and complex potential than a simple rotating potential, we used 10^5 fixed-motion star particles and rotated non-axisymmetric star particles at $54 \text{ km s}^{-1} \text{ kpc}^{-1}$, which is the estimated pattern speed of M83. The expressions and figures of the potential are in Paper I. To remove the discreteness effects of the star particles, we smoothed the particles' gravitational contribution by adding the mass on to the grid at AMR level 4, with a cell size of 50 pc. For a dark matter potential, we used a static dark matter halo with an NFW profile (Navarro et al., 1997).

The galactic gas evolves in the stellar and dark matter potential. For an initial galaxy's radial gas distribution, we assumed an exponential density profile based on the observations of M83 done by Lundgren et al. (2004b), which is equation (2) of Paper I. The initial gas was set in circular motion as calculated via $V_{\text{cir}}(r) = \{GM_{\text{tot}}(r)/r\}^{1/2}$, where $M_{\text{tot}}(r)$ is the enclosed mass of stars, dark matter and gas within the radius r .

4.2.2 Star formation and feedback

We included star formation and stellar feedback from $t = 120$ Myr. In order to wait for formation of the global gas structure of bar and spiral arms, we performed these simulations without star formation or feedback for first 120 Myrs. One pattern rotation period is about 120 Myr, and the gas in galaxy is fully fragmented at that point.

We used a star formation and feedback algorithm based on Cen and Ostriker (1992). It assumes that stars form in dense gas. Star particles are allowed to form in a cell when the following five criteria are met. (1) The cell's gas density exceeds $n_{\text{threshold}} = 1.3 \times 10^4 \text{ cm}^{-3}$ ($n_{\text{cell}} > n_{\text{threshold}}$). Star formation actually is observed to occur around that density (Lada et al., 2010; Ginsburg et al., 2012; Padoan et al., 2014). (2) $\nabla \cdot \mathbf{v}_{\text{cell}} < 0$, that shows the gas around the cell are converging on it. (3) The cooling time is less than the dynamical time ($t_{\text{cool}} < t_{\text{dyn}} \equiv \sqrt{3\pi/32G\rho_{\text{tot}}}$) or the temperature is less than 11,000 K. (4) The star particle mass is greater than $m_{\text{min}} = 500 M_{\odot}$. We impose this condition in order to avoid the creation of an excessive number of star particles, that makes simulation slow. Moreover, a star particle must have larger than about $200 M_{\odot}$ in order that one star particle has at least one massive star which will explode as an SN Type II at the end of its lifetime. That is because approximately $200 M_{\odot}$ of gas produces on average one massive star ($> 8 M_{\odot}$) according to a conventional stellar initial mass function (e.g. Salpeter 1955). Our condition of minimum star particle mass, $m_{\text{min}} = 500 M_{\odot}$, is close to the limit of star particle mass. (5) The cell does not have finer refinement underneath it.

If all of these criteria are met, a star particle is created at the centre of the cell which has $m_{\text{star}} = m_{\text{cell}}(\Delta t/t_{\text{dyn}})f_{\text{SFE}}$, where f_{SFE} is the star formation efficiency parameter, and the same velocity as the removed gas. An amount of gas corresponding to the new particles's mass is removed from the cell. We used $f_{\text{SFE}} = 0.002$. This efficiency is 10 times lower than the observed GMC averaged star formation efficiency (Krumholz and Tan, 2007), however we used it to make SFR of our simulated galaxy corresponds to that of M83 (Fig. 4.7). Each routine keeps a global sum of unfulfilled star formation that were not previously formed because the star particle masses were under m_{min} . When this running sum exceeds the minimum mass, it

Simulation	Star formation	SNe heating
NoSF	No	No
SFOnly	Yes	No
SNeHeat	Yes	Yes

Table 4.1. Summary of the simulations compared in this chapter. Star formation or stellar feedback are included from $t = 120$ Myr.

forms a star particle. This is known for stochastic star formation. In fact, all star particles in our simulation are formed by this stochastic star formation having $500 M_{\odot}$. That is because our $f_{\text{SFE}} = 0.002$ means no cell ever fulfills the minimum mass criteria immediately.

The star formation algorithm creates each star particle instantaneously. However, stellar feedback should take place over a significant timescale because all stars contained within the star particle would be formed over a substantial period of time. Therefore, our algorithm assumes that the mass of stars formed in each star particle is distributed as $m_{\text{star}} \cdot \tau e^{-\tau}$, where $\tau = (t - t_{\text{form}})/t_{\text{dyn}}$ and t_{form} is the formation time of the star particle. The mass of stars formed at a time t with time step Δt is,

$$\begin{aligned}
 \Delta m_{\text{sf}} &= M(t + \Delta t) - M(t) \\
 &= \int_t^{t+\Delta t} \frac{dM}{dt} dt \\
 &= \int_{\tau_0}^{\tau_1} m_{\text{star}} \cdot \tau e^{-\tau} d\tau \\
 &= m_{\text{star}} [(1 + \tau_0)e^{-\tau_0} - (1 + \tau_1)e^{-\tau_1}]
 \end{aligned} \tag{4.1}$$

where $M(t)$ is the total stellar mass formed between t_{form} and t , $\tau_0 = (t - t_{\text{form}})/t_{\text{dyn}}$, and $\tau_1 = (t + \Delta t - t_{\text{form}})/t_{\text{dyn}}$.

During the timestep Δt , the star particle adds thermal energy feedback from supernovae and stellar winds to the neighboring cells until 12 dynamical times after its creation. This algorithm assumes that there is a feedback of same fraction f_{SN} of the rest-mass energy from the stars into the gas, such that $E_{\text{add}} = f_{\text{SN}}(\Delta m_{\text{sf}} c^2)$. We used $f_{\text{SN}} = 3 \times 10^{-6}$, which is equivalent to about three supernovae for every $500 M_{\odot}$ star particle formed assuming one supernova ejects 10^{44} J. We distributed the stellar feedback over the neighboring 19 ($= 3^3 - 8$) cells, so that the thermal energy added to each cell is $\Delta E_{\text{cell}} = E_{\text{add}}/19$. To model a spherical explosion of the stellar feedback, the eight corner cells in a 3^3 cube are removed. Finally, $m_{\text{ej}} = f_{\text{ej}} \Delta m_{\text{sf}}$ is removed from the star particle mass m_{star} and returned to the grid cell, and $m_{\text{ej}} \mathbf{v}_{\text{gas}}$ of momentum is added to the cell in order to simulate the mass ejection from all stars. We used $f_{\text{ej}} = 0.25$.

Table 4.1 shows all simulations we performed. To compare the effects of the star formation and thermal stellar feedback, we performed three different runs: no star formation or feedback run (NoSF), only star formation run (SFOnly) and thermal feedback run (SNeHeat). NoSF was published in Paper I.

4.2.3 Cloud analysis

The GMCs in our simulation were identified as coherent structures contained within contours at a threshold density of $n_{\text{gas}} = 100 \text{ cm}^{-3}$, similar to the observed mean volume densities of typical galactic GMCs. Note that we do not include formation or destruction of molecules, so that the gas is purely atomic. We expect that the cloud would consist of both a molecular core and atomic envelope.

We assigned an environment group based on the cloud's physical location within the disc. If a cloud is found within the galactic radii $2.5 < r < 7.0$ kpc, it is recognised as a spiral cloud. Bar clouds form in a box-like region at the galactic centre, with a length of 5.0 kpc and width

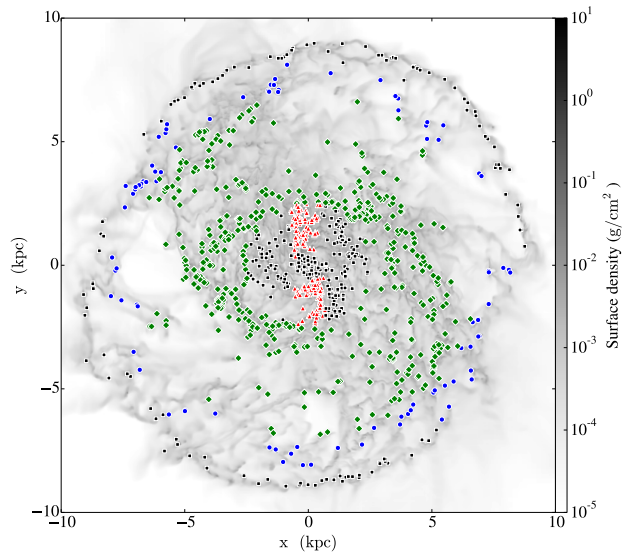


Figure 4.1. The three different galactic environments: bar, spiral and disc. The markers denote the cloud types; red triangles, green diamonds and blue circles show clouds in the bar, spiral and disc, respectively. The black squares shows clouds not included in cloud analysis. The background image shows the gas surface density of SNeHeat run at $t = 200$ Myr.

1.2 kpc. The nucleus region inside 600 pc is excluded from cloud analysis due to the difficulty in accurately tracking clouds in such a high density area. Outside $r = 7.0$ kpc, clouds are designated disc clouds. The most outer ring which is formed from Toomre instability is also excluded from cloud analysis because they are formed during the disc's initial fragmentation and not a realistic environment for cloud formation. In detail, we locate a radial position, r_{\max} , of the cloud who is the furthest from the galactic centre, and we ignore the all clouds who is in the ring region of $(r_{\max} - 1.5 \text{ kpc}) < r < r_{\max}$. These three regions are shown in Fig. 4.1, which shows the three different cloud types based on their location: bar, spiral and disc region. The background image is the surface density of the gas of SNeHeat run at $t = 200$ Myr. Figure 5 of Paper I also shows the three galactic regions though the image shows NoSF run at $t = 240$ Myr.

There are two differences between this work and previous works (Paper I). The first is star formation and feedback. In this work, we performed simulations included the star formation and thermal stellar feedback (see Section 4.2.2). The second is the analyzation time of the clouds. In this simulation, we analysed the properties of clouds at $t = 200$ Myr. On the other hand, in previous work, we analysed the properties of clouds at 240 Myr. That is because the grand design spiral disperse after $t = 220$ Myr in SNeHeat run, and the global gas distribution differs from the actual gas distribution of M83. For future comparison with high resolved observation of M83 (e.g. ALMA), we value the similarity of the gas distribution rather than the stability of the galactic disc.

4.3 Results

4.3.1 The stellar feedback effects on the ISM

Fig. 4.2 shows the gas distribution of the whole galactic disc of the three runs. Each image is 20 kpc across, whereas the simulation box size is 50 kpc. The colour shows the gas surface density; red and yellow show high density regions, and blue and purple show low density regions. The non-axisymmetric pattern rotates anticlockwise.

In NoSF and SFOnly, the galactic disc settles into quasi-equilibrium with no large structure

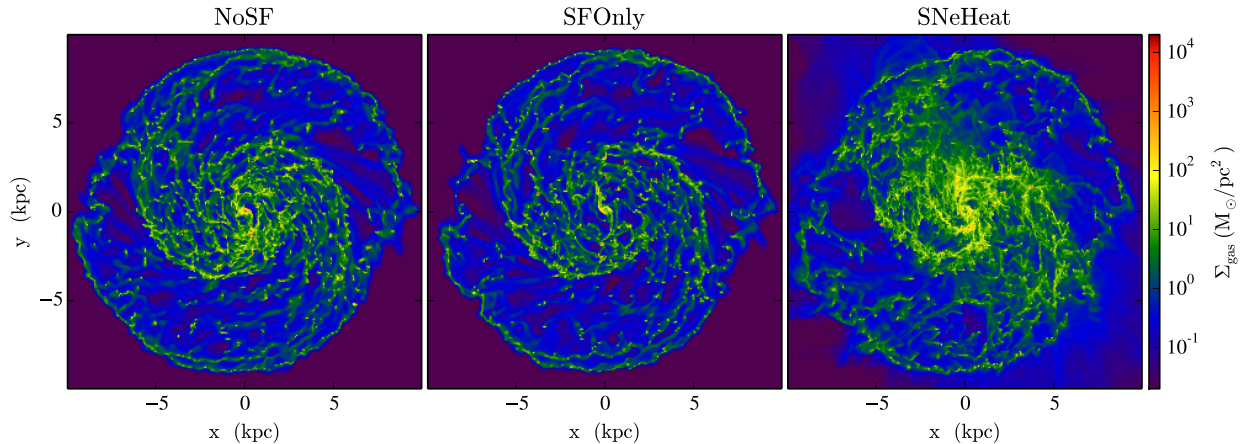


Figure 4.2. The gas distribution of the galactic disc of the three runs: the left is NoSF, the middle is SFOnly, and the right is SNeHeat. Images show the gas surface density of the face-on disc at $t = 200$ Myr. Each image is 20 kpc across. The galactic disc rotates anticlockwise.

change at this time period ($t = 200$ Myr), and grand design of the bar and spiral arms can be clearly seen in each panel. The gas distribution is roughly similar to that comes from CO observation of M83 (Lundgren et al., 2004b), though our gas distribution is finer than the observation because the resolution is quite different; the resolution of our simulation is 1.5 pc, whereas that of the observation is 980 pc. The slight difference between the two runs is the lower surface density in the bar and spiral regions in SFOnly than that in NoSF. That is because the star formation rate is higher in the bar and spiral regions than the other regions due to their high gas density. The star formation converts the high density gas into star particles, and then the amount of the gas gets low especially in the high star formation rate regions of the bar and spiral. Therefore, we see the different gas surface density especially in the bar and spiral regions.

In SNeHeat, the bar and spiral arms can be also seen, but the green and yellow mediate density regions ($10^1 \sim 10^2 \text{ M}_\odot \text{pc}^{-2}$) are largely distributed not only in the bar and spiral regions but also in the other regions, especially in the inter-arm regions. That is because the thermal stellar feedback injects huge energy into the interstellar gas around star particles causing expansion of the gas, and then a lot of gas are scattered around dense star forming clouds. Moreover, the thermal feedback slightly changes the shape of the bar and spiral arms compared with NoSF and SFOnly; the bar and spiral arms seem to shrink into the galactic centre compared to NoSF and SFOnly. Because of the lack of the resolution of the CO observation, it is hard to know whether the galactic structures in the three runs exactly correspond to the actual gas distribution of the M83. However, the galactic disc of all three runs roughly look similar to the gas distribution of M83 in Lundgren et al. (2004b); we can see the bar and grand design spiral structures, that are the typical features of M83.

Fig. 4.3 shows the zoom up face-on disc ($5 \text{ kpc} \times 5 \text{ kpc}$) on the upper side of the bar-end region at $t = 200$ Myr. The colour shows surface density (top row), density at the middle plane of the disc (middle row), and temperature at the middle plane of the disc (bottom row) of the gas, respectively.

In NoSF (left column), in gas surface density figure, we can see a lot of clouds, which has a density peak at its centre. We also see many tidal filament structures around them. In the bar region, many large massive clouds are produced, and interactions between them form the tidal filaments (Paper I). In SFOnly (middle column), there are less tidal filaments. That is because less massive and less extended clouds due to star formation make it hard to pull gas away from their compact bodies and to interact with each other clouds, and then we see less tidal filaments.

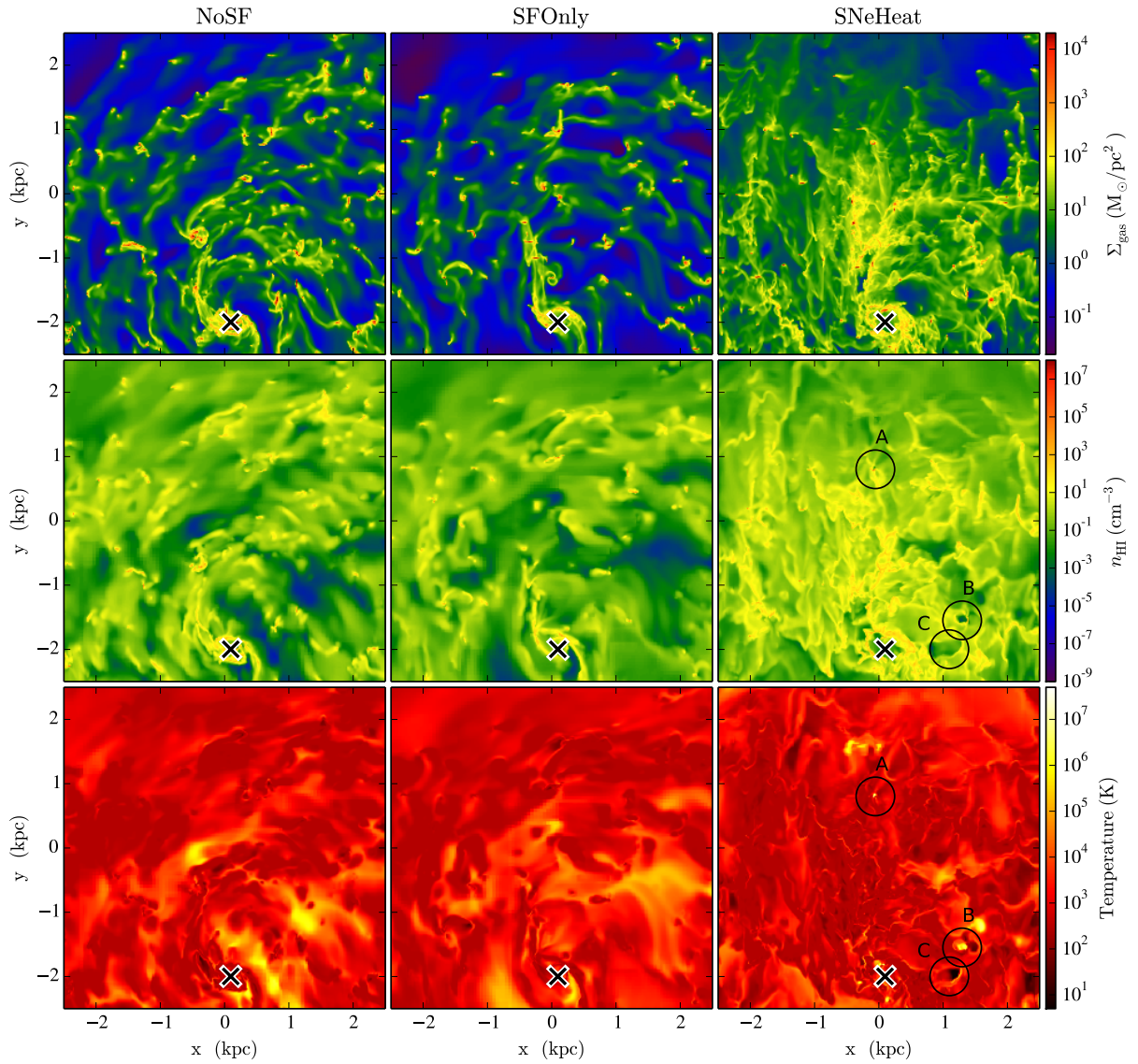


Figure 4.3. Zoom up images on the bar-end region of the galactic disc at $t = 200$ Myr of the three runs; the left column is NoSF, the middle column is SFOnly, and the right column is SNeHeat. Each image is 5 kpc across. From top to bottom, the colour images show the gas surface density, the gas density at the middle plane of the disc ($z = 0$) and the gas temperature at the middle plane of the disc. x mark at the bottom of the image shows the galactic centre. The galactic disc rotates anticlockwise.

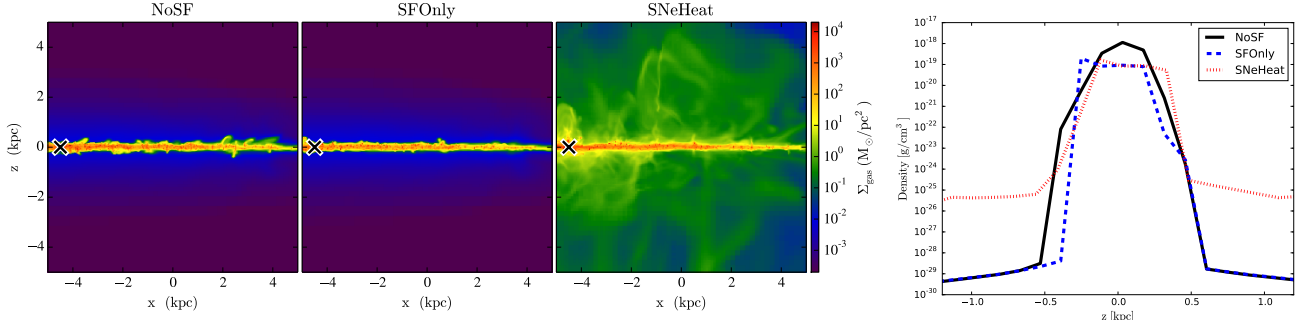


Figure 4.4. Left: Edge-on images of the galactic disc at $t = 200$ Myr of the three runs: the left is NoSF, the middle is SFOnly, and the right is SNeHeat. The images show the gas surface density. Each image is 10 kpc across. x mark at the left side of the image shows the galactic centre. Right: 1D profile of the scale height of the galactic disc at $t = 200$ Myr. The y-axis is the mass weighted average density as a function of the position z . The black solid line is NoSF, the blue dashed line is SFOnly, and the red dotted line is SNeHeat.

In SNeHeat (right column), the gas distribution is quite different from those of NoSF and SFOnly. In the gas surface density figure, we see a dispersed gas around clouds, and the surface densities in the inter-cloud regions are high. Although star formation reduces the number of massive clouds and tidal filaments, the stellar feedback disperse gas of clouds and form new filament structures. Circle A, B and C show early, middle and late phase of the stellar feedback sites, respectively. In the centre of the circle A, we see a high density and high temperature compact region, where the stellar feedback has just been injected into the dense gas region. The dense region which has high thermal energy induced by the feedback expand into the surrounding gas, making a cavity in the ISM as seen in Circle B. In the end, as seen in Circle C, the thermal energy decreases due to a radiative cooling although there is still high dense and high temperature rim. Moreover, a higher volume fraction of gas is in colder phase than NoSF and SFOnly because the gas density in the inter-cloud region gets high due to the gas dispersion by the stellar feedback.

Fig. 4.4 shows the edge-on galactic disc and the scale height of the galactic disc. Compared with SFOnly, NoSF has some tidal filaments induced by cloud-cloud interactions. As shown in Fig. 4.3, SFOnly has a few massive cloud, which causes strong cloud interactions, because of a lack of cloud gas by star formation. That is why SFOnly has almost no tidal filaments, and the scale height of the disc is sight smaller than that of NoSF.

In SNeHeat, the vertical gas distribution of the disc is quite different from NoSF and SFOnly. We see galactic fountains induced by the thermal stellar feedback, and the gas density of outside of the disc ($|z| > 0.5$ pc) is 3 order of magnitude greater than that of NoSF and SFOnly. Interestingly, the scale height of the galactic disc (~ 400 pc) is almost same as NoSF and SFOnly. That means that the thermal stellar feedback changes the medium density gas, but not the dense gas distribution, and then does not affect the thickness of the galactic disc.

The scale height of our simulated disc is about 400 pc in all runs. Though it is impossible to compare it with observation of the face-on galaxy M83, our scale height of the gas is in agreement with those of other galaxies; e.g. 100 \sim 500 pc in Milky Way (Lockman, 1984; Sanders et al., 1984), 180 pc in LMC (Padoan et al., 2001), 200 pc in NGC 891 (Scoville et al., 1993).

Fig. 4.5 is the ISM mass distribution in temperature versus density. NoSF and SFOnly show almost same distribution; high mass fraction of gas in low temperature and high density phase. The cut-off temperature at 300 K is a lower limit of cooling function we use. We also see a warm ISM distribution, which has higher temperature than 10^3 K and lower density than 10^0 cm^{-3} in both runs. Moreover, we see a spread of low temperature and low density ISM ($T < 300$ K). They are an adiabatic expansion of the gas expanding to outside of the galactic disc. As shown in Fig. 4.4, cloud-cloud interactions cause the expansion to a vertical direction of the

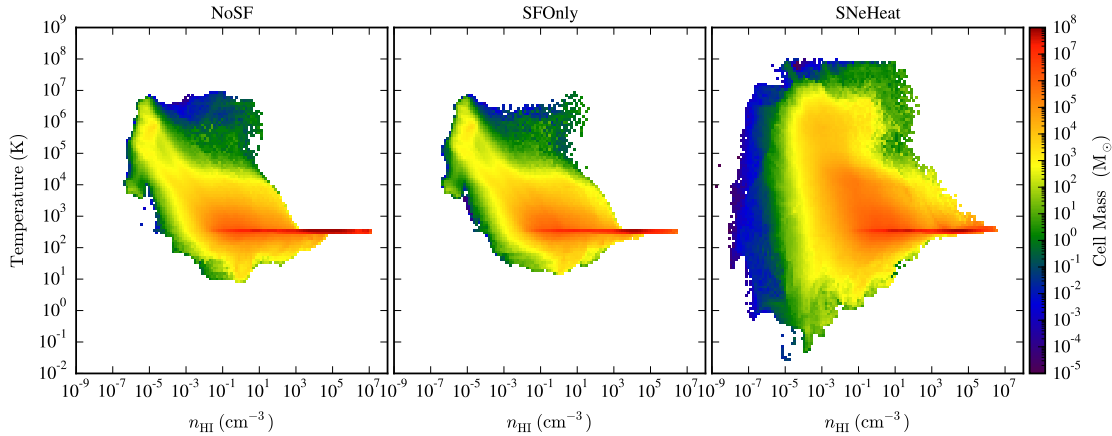


Figure 4.5. The ISM mass distribution in temperature versus number density at 200 Myr. Left is NoSF, middle is SFOnly, and right is SNeHeat.

galactic disc. That is why the spread of the low temperature low density gas is slight larger in NoSF than that of SFOnly where the cloud interaction is rare. There is another difference between NoSF and SFOnly; the maximum density of SFOnly is lower than that of NoSF. That is because star formation converts high density gas into star particle, and the maximum density of gas slightly gets lower in SFOnly run.

Compared to NoSF and SFOnly, the distribution in SNeHeat is quite different. Thermal stellar feedback is injected into the densest star forming regions, so that we see hotter dense gas than 300 K at densities $> 10^3 \text{ cm}^{-3}$. However, the main difference is to the gas with densities outside the clouds ($10^{-3} \sim 10^2 \text{ cm}^{-3}$). The warm ISM distribution is more spread compared with the other runs, which does not include the stellar feedback. This agrees with Fig. 4.2 and 4.3, where we saw the most difference to the inter-cloud gas. Moreover, we see a spread of low density ISM ($< 10^{-4} \text{ cm}^{-3}$), which covers a wide range of temperature. They are an adiabatic expansion of galactic fountain induced by thermal energy inputs of stellar feedback as shown in Fig. 4.4.

The top panels of Fig. 4.6 shows the time evolution of radial profiles of the gas surface density. NoSF shows a time independence of the profile. SFOnly shows a decrease of the gas surface density with time because of the gas conversion into stars. We see the gas decrease especially in the galactic centre region ($r < 3 \text{ kpc}$) because the star formation time scale is shorter in the region due to the higher gas density than the outer region. SNeHeat shows a slight decrease of the gas surface density, but it keeps high near the state at $t = 120 \text{ Myr}$, especially in the galactic centre region ($r < 1.5 \text{ kpc}$). That suggests two possibilities. First is a gas inflow into the galactic centre as suggested by Fig. 4.2. We see not only a high gas surface density in the galactic centre region, but also a large drop in the gas surface density in the outer region ($r > 4 \text{ kpc}$). Second is a suppressed star formation activity in SNeHeat due to the stellar feedback.

The middle and bottom panels of Fig. 4.6 shows the radial profiles of the circular velocity and the velocity dispersion of the gas, respectively. NoSF shows no time change of the profiles. The high velocity dispersion in the galaxy centre region ($r < 2 \text{ kpc}$) comes from the elongated elliptical motion of the gas due to the bar potential. Moreover, high rate of the cloud-cloud interaction also increase the velocity dispersion in the bar region.

SFOnly shows almost no time dependence of the circular velocity profile and a slight increase of the velocity dispersion with time because cold dense gas is converted into stars, leaving the warmer, higher velocity dispersion gas. On the other hand, SNeHeat shows a decrease of the circular velocity and an increase of the velocity dispersion except galaxy centre. These suggest a transition of the gas motion from circular to radial due to a driving of turbulence of the ISM by a stellar feedback.

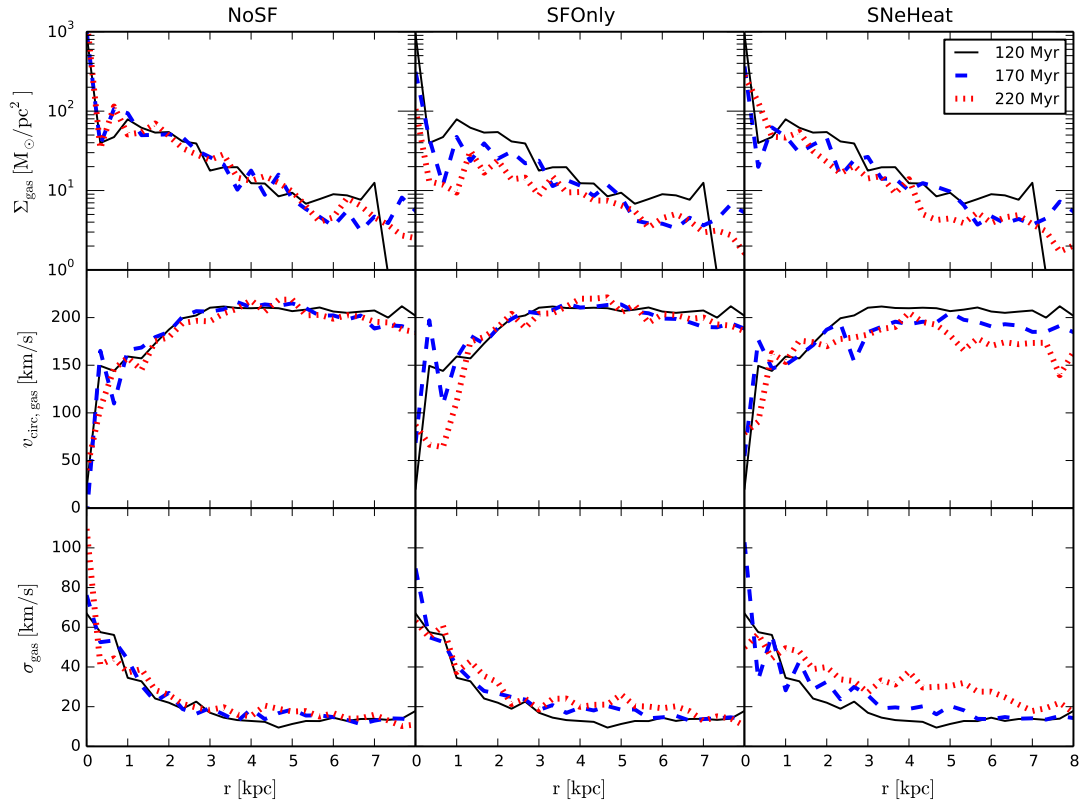


Figure 4.6. Azimuthally averaged (bin size 333 pc) radial gas profiles for the galactic disc at $t = 120, 170$ and 220 Myr. From top to bottom row: (1) gas surface density, $\Sigma_{\text{gas}} = \int_{-1\text{kpc}}^{+1\text{kpc}} \rho(z) dz$, (2) gas circular velocity (mass-weighted average over $-1\text{ kpc} < z < 1\text{ kpc}$) and (3) 1D gas velocity dispersion defined by $\sigma_{\text{gas}} = \sqrt{(\mathbf{v} - \mathbf{v}_{\text{cir}})^2/3}$ (also mass-weighted average over $-1\text{ kpc} < z < 1\text{ kpc}$). We included the star formation and feedback from $t = 120$ Myr, so that the profiles of the three runs at 120 Myr are the same.

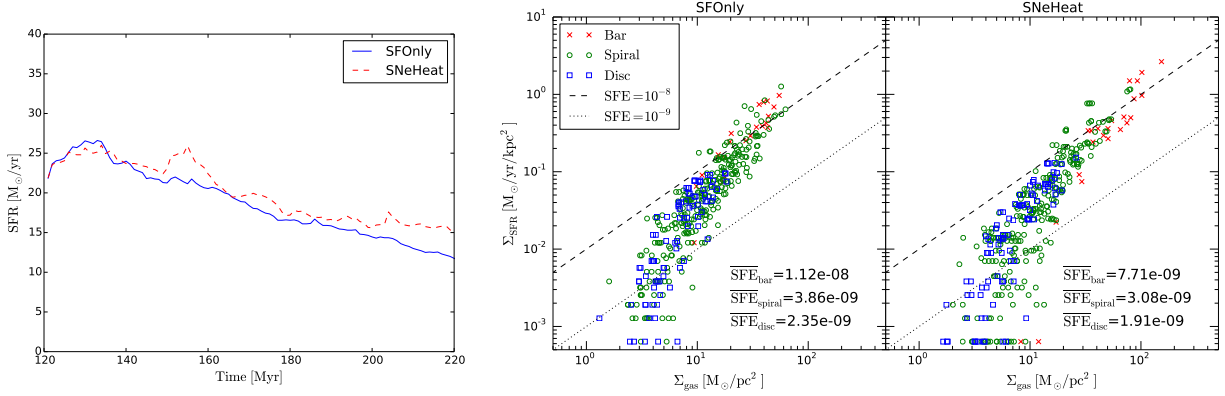


Figure 4.7. Star formation rate (SFR) in our simulated galaxy. Left; time evolution of SFR of SFOnly (blue solid line) and SNeHeat (red dashed line). We included the star formation and feedback from $t = 120$ Myr in both runs. Right; the Kennicutt-Schmidt relation for SFOnly and SNeHeat runs at $t = 200$ Myr. The red x, the green circle and the blue square show bar, spiral and disc region, respectively. The surface area is calculated in the x - y plane (face-on disc) and the data are averaged over a cylindrical region with radius 500 pc and height 5 kpc. The black lines show constant star formation efficiency (SFE): 10^{-8} and 10^{-9} (yr^{-1}).

4.3.2 The stellar feedback effects on star formation

Star formation and feedback are included from $t = 120$ Myr as shown in Section 4.2.2. We estimated the star formation rate (SFR) of our simulated galaxy using formation rate of star particles.

Left panel of Fig. 4.7 is the time evolution of SFR of whole galaxy in SFOnly (blue solid line) and SNeHeat (red dashed line). In the first 10 Myrs, SFRs in the both runs increase, and they reach over $25 M_{\odot}\text{yr}^{-1}$ because dense gas regions are already formed at $t = 120$ Myr, and they are transformed into star particles all at once. After the star burst, they gradually decrease because the amount of the dense gas in clouds are eaten up by the star formation converting dense gas into star particles. Trends of the two runs are similar, and the SFR at $t = 200$ Myr of the both runs are about $15 M_{\odot}\text{yr}^{-1}$. It is roughly corresponds to observed SFR ($5 \sim 20 M_{\odot}\text{yr}^{-1}$) of M83 (Hirota et al., 2014). In order to make the SFR of our simulated galaxy have the same order of magnitude as the observed SFR, we set $f_{\text{SFE}} = 0.002$ as shown in Section 4.2.2.

The SFR in SNeHeat is not lower than that in SFOnly, and the trends are similar. That suggests that the thermal stellar feedback we performed has weak effects on star forming dense gas although it affects on warm ISM as shown in the previous section. This result supports the idea of a gas inflow into the galactic centre in SNeHeat run as discussed in Fig. 4.6, not the idea of a low SFR. On the contrary, we see a constant higher SFR after 150 Myr in SNeHeat than that in SFOnly. That suggests four possibilities; one is that a lot of gas inflow into the galactic centre feeds material for star formation and keeps SFR high. Second is a triggered star formation induced by a compression of the ISM due to SN explosion. Third is that the remain gas of the first star burst feeds material; SFR in SNeHeat at $t = 130$ Myr is slightly lower than that in SFOnly. Fourth is that the mass ejection from star particles feeds the gas to the star formation region again. These processes would keep and raise the SFR of the whole galaxy in SNeHeat. These four possibilities do not conflict with each other, and they can perform at the same time. Although it is hard to distinguish the four processes and to make clear which process dominates, we prefer the gas inflow toward the galactic central region because we apparently see the gas increase in the central region as seen in Fig. 4.2 and Fig. 4.6. Moreover, we see inflows of star forming clouds due to a hydrodynamical drag force as discussed in the following sections.

Right panel of Fig. 4.7 shows the SFR surface density (Σ_{SFR}) and the gas surface density (Σ_{gas}) averaging over a cylindrical region with radius 500 pc and height 5 kpc. The colours

indicate the galactic regions: bar, spiral and disc. There is a correlation between them in both SFOnly and SNeHeat, which is the same as well known empirical relation of Kennicutt-Schmidt law ($\Sigma_{\text{SFR}} \propto (\Sigma_{\text{gas}})^N$: Kennicutt 1998). That is a super-linear relation, and the index N of our relation is ~ 1.7 . We do not include H_2 formation, and our gas indicate total gas ($= \text{HI} + \text{H}_2$). In observation, the Kennicutt-Schmidt relation between Σ_{SFR} and $\Sigma_{\text{HI}+\text{H}_2}$ also shows a super-linear relation, and the index is between 1 and 2 (e.g. $N = 1.4$ (Kennicutt, 1998)). This correspondence indicate that our star formation recipe is reliable (This is not self-evident although our star formation recipe uses $\dot{\rho}_{\text{star}} \propto \rho_{\text{gas}}/t_{\text{ff}} \propto (\rho_{\text{gas}})^{1.5}$. That is because the ρ_{gas} is the volume density of the gas, not the surface density of the gas (Σ_{gas}) used in the Kennicutt-Schmidt relation.)

There are features of the galactic regions; the bar region has the highest SFR and gas surface density on average, and, on the other hand, the disc region has the lowest SFR and gas surface density. Moreover, because of $N > 1$, the SFE in the bar region is higher than the other regions. The average features are the same in both SFOnly and SNeHeat. However, only in SNeHeat, some bar region have quite high gas surface density ($> 10^2 \text{ M}_{\odot}\text{pc}^{-2}$) and SFR ($> 10^0 \text{ M}_{\odot}\text{yr}^{-1}\text{kpc}^{-2}$). This result also supports the idea of gas inflow into the galactic centre region. Because the gas inflow keeps both the gas mass and the SFR high in the bar region, SFEs of them in SNeHeat are the same as those in SFOnly.

Some observations of a barred galaxy show a lower SFE in the bar region than that in the spiral arm region (Momose et al., 2010; Hirota et al., 2014). Fujimoto et al. (2014b) showed that a cloud-cloud collision star formation model of Tan (2000) adding a dependence of the collision velocity can explain the lower SFE in the bar region; cloud interactions in the bar region are the most violent due to a elliptical global gas motion induced by the stellar bar potential, and the fast cloud-cloud collision reduces the massive cloud core formation. Our results, however, do not show the lower SFE in the bar region. This is because we do not consider the star formation induced by the cloud-cloud collision in our star formation recipe, and we just use a standard star formation model depending on the local gas density. Our result of high SFE in the bar region is consistent with Paper I result which used only the gas density of cloud for estimating SFR for each cloud (see Section 3.4.1 and Figure 11 in Paper I). It is difficult to resolve each process of a formation of shocked dense region and massive cloud core induced by a cloud-cloud collision because of a lack of resolution in our current simulation ($\Delta x = 1.5\text{pc}$). If we get sub parsec resolution, processes of the dense core formation due to the gas compression by the cloud collision and the destruction of the core due to too fast collisions could be resolved, and we would get the lower SFE in the bar region due to a stabilization of cloud cores by a internal gas energy input from violent cloud interactions there.

4.3.3 The stellar feedback effects on cloud properties

Clouds in our simulations were defined as coherent structures contained within contours at a threshold density of $n_{\text{gas}} = 100 \text{ cm}^{-3}$ as shown in Section 4.2.3. In this section, we discuss effects of star formation and stellar feedback on the cloud properties.

In Paper I, we introduced three cloud types using cloud mass-radius scaling relation; *type A* clouds are normal clouds that have typical values of cloud properties: mass, radius and 1D velocity dispersion. *Type B* clouds are massive giant molecular associations (GMAs). *Type C* clouds are transient clouds that are gravitationally unbound and have short lifetime than 1 Myr. They are formed in dense filaments and tidal tails caused by cloud-cloud interactions of *Type A* and *B* clouds. We clarified an environmental dependence of clouds between galactic regions using the three cloud types; percentages of the three cloud types depend on the galactic regions. Top panels of Fig. 4.8 shows the scaling relations of cloud mass-radius for the three runs. The cloud mass, M_c , is a sum of cell mass which composes the cloud, and the cloud radius is defined as $R_c = \sqrt{(A_{xy} + A_{yz} + A_{zx})/3\pi}$, where A_{xy} is the projected area of the cloud in the x - y plane, A_{yz} is that in the y - z plane, and A_{zx} is in the z - x plane. We categorised all clouds into the three types in the same way as Paper I; *type A* clouds exist on upper trend of bimodal

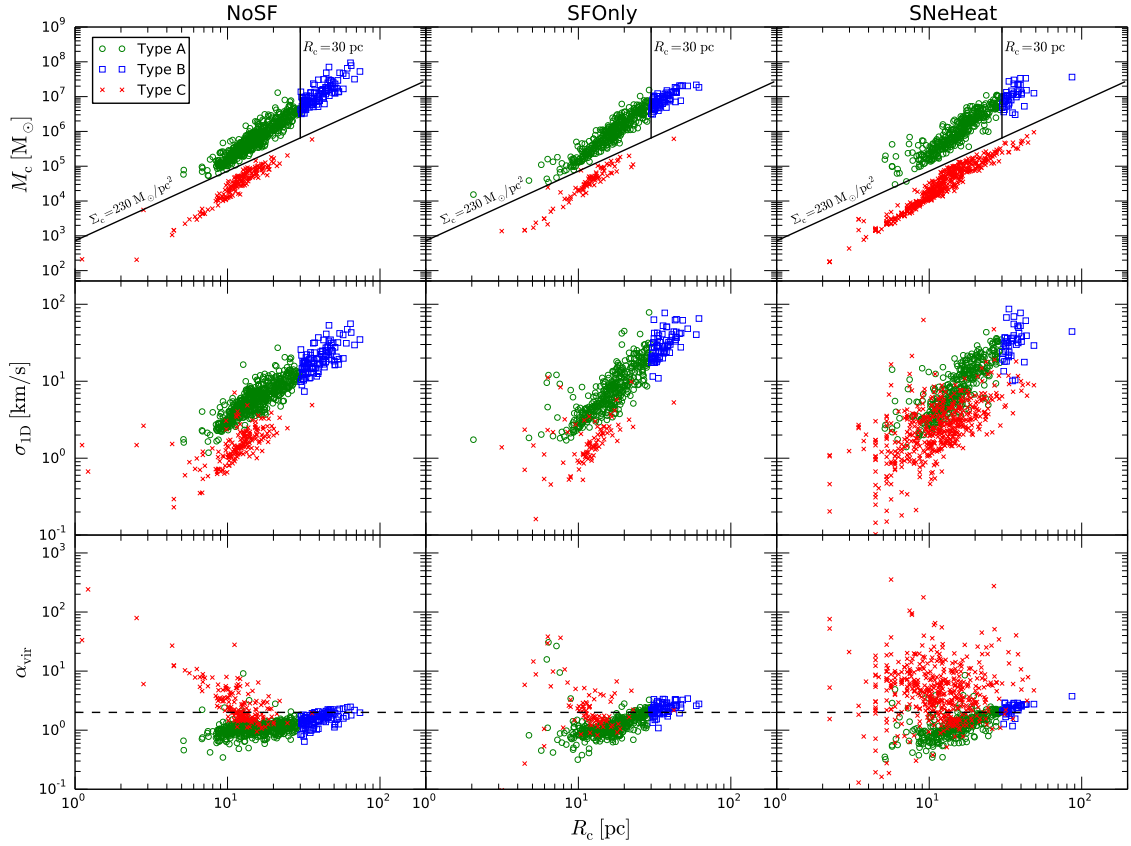


Figure 4.8. Scaling relations for our three cloud type categorisations. Top panels show the cloud mass, M_c , versus the average cloud radius, $R_c = \sqrt{(A_{xy} + A_{yz} + A_{zx})/3\pi}$, where A_{xy} is the projected area of the cloud in the x - y plane, A_{yz} is that in the y - z plane, and A_{zx} is in the z - x plane. They define the three cloud types: *type A* clouds exist on the upper trend of the bimodal split, with surface densities greater than $230 M_\odot \text{pc}^{-2}$. *Type B* clouds sit at the high end of the same sequence, with radii greater than 30 pc. *Type C* cloud follow the lower trend and have surface densities less than $230 M_\odot \text{pc}^{-2}$. The middle panels show the 1D velocity dispersion versus cloud radius; $\sigma_{1D} = \sqrt{[(v_x - v_{c,x})^2 + (v_y - v_{c,y})^2 + (v_z - v_{c,z})^2]/3}$, where (v_x, v_y, v_z) is the velocity of the gas and $(v_{c,x}, v_{c,y}, v_{c,z})$ is the cloud's centre of mass velocity. The bottom panels show the virial parameter versus cloud radius; $\alpha_{vir} = 5(\sigma_{1D}^2 + c_s^2)R_c / \{G(M_c + M_s)\}$, where c_s is a sound speed. The virial parameter is a measure of gravitational binding; a value greater than 1 indicates that the cloud is gravitationally unbound.

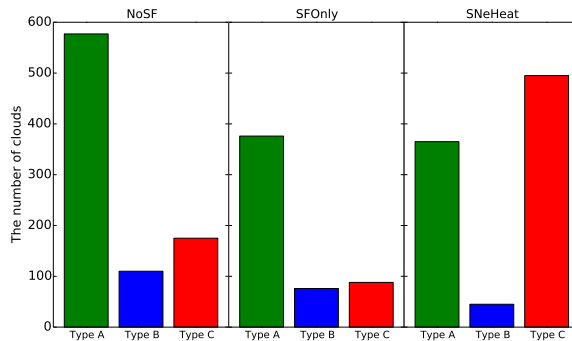


Figure 4.9. The number of clouds of each cloud type in each simulations at $t = 200$ Myr.

split, with surface densities greater than $230 \text{ M}_\odot \text{pc}^{-2}$. *Type B* clouds sit at the high end of the same sequence, with radii greater than 30 pc. *Type C* clouds follow the lower trend and have surface densities less than $230 \text{ M}_\odot \text{pc}^{-2}$. In all three runs, there are clear bimodal splits in the relation and enough larger radius clouds than 30 pc, so that it is still possible to categorise the three cloud types. Therefore, the three cloud types are still good tracers for explaining an environmental dependence of cloud properties between galactic regions.

The distributions of the three cloud types are slightly different between the three runs, so that we can discuss not only the environmental dependence of clouds between galactic regions in one run, but also effects of star formation and stellar feedback on clouds comparing the three different runs using the three cloud types. The typical mass of *Type A* clouds are $5 \times 10^5 M_\odot$ for NoSF, $1 \times 10^6 M_\odot$ for SFOnly and $1 \times 10^6 M_\odot$ for SNeHeat. There are at most factor 2 difference. The mass range is between $10^4 \sim 10^6 M_\odot$ in the all runs. The typical radius of *Type A* clouds are 13 pc for NoSF, 17 pc for SFOnly and 13 pc for SNeHeat. There are almost no difference between the three runs. The radius range is between $5 \sim 30$ pc in the all runs. Therefore, the mass and radius of *Type A* clouds do not change so much when star formation and stellar feedback are included. On the other hand, *Type B* distributions are slightly different between the three runs; the maximums of the mass and radius are different. In NoSF, the maximums reach at $10^8 M_\odot$ and 80 pc. In SFOnly, these are at $2 \times 10^7 M_\odot$ and 60 pc; they are lower than those in NoSF. That is because the star formation reduces cloud gas mass especially in *Type B* clouds due to a high star formation rate in them (see Fig. 4.12). In SNeHeat, the maximums reach at $3 \times 10^7 M_\odot$ and 50 pc except one cloud; compared with SFOnly, the maximum mass slightly increases, but the maximum radius decreases. The dense and compact clouds are mostly in the central bar region. That might be because the high density gas in the central bar region due to gas inflows forms massive and high density clouds, and the stellar feedback exploded at the edge of the cloud disperses some fraction of the cloud gas, which makes cloud size smaller.

The most prominent difference of the cloud mass-radius distribution is the number of *type C* clouds; there are fewer *type C* clouds in SFOnly, and, on the other hand, there are more *type C* clouds in SNeHeat. Fig. 4.9 clearly shows the difference of the number of three cloud types between the three runs. In NoSF, the *type A* clouds are the most dominant clouds, and the *type B* and *type C* are minorities. In SFOnly, although *type A* cloud is still the most dominant cloud, the total number of clouds decreases. That is because star formation converts dense parts of clouds into star particles, and then the total amount of dense gas for cloud formation decreases. Moreover, a decrease of *type C* in SFOnly is slightly larger than that of *type B*. That is because the *type C* clouds are formed in dense filaments and tidal tails, that are caused by *type B* cloud interactions as discussed in Paper I. As shown in Fig 4.3, the formation of massive clouds (= *type B*) would be weak when star formation is included. Therefore, the decrease of *type B* clouds strongly affects the formation of *type C* clouds, and the number of *type C* decreases more than that of the *type B* clouds.

In SNeHeat, dominant typical clouds are not *type A*, but *type C* clouds although the number of *type B* cloud is the least in the three runs. This suggest that the formation mechanism of the *type C* clouds in SNeHeat is different from that of NoSF or SFOnly in which *type C* clouds are formed in dense filaments and tidal tails, those are caused by *type B* cloud interactions. The thermal stellar feedback forms not only warm ISM as discussed in Section 4.3.1, but also *type C* clouds; they are formed in the warm ISM. That is why the *type C* clouds in SNeHeat tend to have larger radius than in NoSF and SFOnly as seen in Fig. 4.8. In NoSF and SFOnly, the *type C* clouds are formed in filaments, so that the size of them is limited to the width of the filament. On the other hand, the size of the *type C* in SNeHeat is not strongly limited because they are formed in the extended warm ISM. The number of *type B* cloud is the least in the three runs because the formation of *type B* cloud is suppressed by the high star formation rate and strong feedback (see Fig. 4.12), and some of them change into smaller *type A* clouds due to the gas dispersion at the edge of the clouds by the feedback. Some *type A* clouds are also dispersed and destroyed by the stellar feedback, but new *type A* clouds are supplied from the

downsizing of the *type B* clouds. That is why the number of the *type A* is the almost same between SFOnly and SNeHeat.

We compared our simulated cloud properties with observational GMC catalogues from the Milky Way (Roman-Duval et al., 2010) and M33 (Rosolowsky et al., 2003). The typical masses of *type A* clouds for our three runs ($5 \times 10^5 \sim 1 \times 10^6 M_\odot$) are larger than those in the Milky Way and M33 ($5.0 \times 10^4 M_\odot$ and $1.0 \times 10^5 M_\odot$). The typical radius of *type A* clouds for our three runs (13 ~ 17 pc) are slightly larger than those in Milky Way and M33 (9 and 10 pc). Note that these comparisons have limits because GMC populations between galaxies have systematic differences and the surveys have been performed at different resolutions (Hughes et al., 2013). Although there is no survey of GMCs in M83 due to the low resolution at present, we expect that higher resolution observations would be done by ALMA and possible to compare them with our results. In the meantime, the observations from the Milky Way and M33 provide a guide to assess our results. Because the mass and radius ranges of *type A* clouds ($10^4 \sim 10^7 M_\odot$ and 4 ~ 30 pc) include the typical values of the Milky Way and M33, we argue that our simulated clouds are similar to observed GMCs.

Middle and bottom panels of Fig. 4.8 show scaling relations of 1D velocity dispersion versus radius and virial parameter versus radius, respectively. The mass weighted 1D velocity dispersion of cloud is defined as

$$\sigma_{1D} = \sqrt{\frac{(v_x - v_{c,x})^2 + (v_y - v_{c,y})^2 + (v_z - v_{c,z})^2}{3}}, \quad (4.2)$$

where (v_x, v_y, v_z) is the velocity of the gas, and $(v_{c,x}, v_{c,y}, v_{c,z})$ is the cloud's centre of mass velocity. The virial parameter is defined as

$$\alpha_{\text{vir}} = 5 \frac{(\sigma_{1D}^2 + c_s^2) R_c}{G(M_c + M_s)}, \quad (4.3)$$

where c_s is a sound speed, M_c is total gas mass of cloud, and M_s is total mass of star particles that are in the cloud's boundary. The α_{vir} is a measure of gravitational binding; a value less than 2 indicates that the cloud is gravitationally bound, and vice versa (Bertoldi and McKee, 1992).

Typical features of the $\sigma_{1D}-R_c$ and $\alpha_{\text{vir}}-R_c$ of the three cloud types are roughly the same in the all three runs; *type A* and *type B* clouds show clear correlations both $\sigma_{1D}-R_c$ and $\alpha_{\text{vir}}-R_c$, and *type C* clouds are not on the correlations and have lower σ_{1D} and higher α_{vir} than the correlations. However, the slopes of the $\sigma_{1D}-R_c$ correlations in SFOnly and SNeHeat are slightly steeper than that in NoSF, and the average σ_{1D} of *type B* clouds gets higher in SFOnly and SNeHeat than NoSF. That is because the densest parts in cloud where the velocity dispersion of the gas is low are converted into star particles, and then the average σ_{1D} gets high when star formation is included. The typical values of σ_{1D} is 6 km/s in NoSF, and those are 10 km/s in SFOnly and SNeHeat. This increase of the σ_{1D} also affects α_{vir} ; the slopes of the $\alpha_{\text{vir}}-R_c$ correlations in SFOnly and SNeHeat get slightly steeper than that in NoSF.

As same as M_c-R_c relations, the distributions of *type C* cloud in $\sigma_{1D}-R_c$ and $\alpha_{\text{vir}}-R_c$ relations considerably change between the three runs. As discussed in Fig. 4.9, the number of *type C* cloud increases in SNeHeat. Moreover, the distributions have large dispersions. That is because the formation process of the *type C* cloud in SNeHeat is different from those in NoSF and SFOnly. Without stellar feedback, the *type C* clouds are formed in dense tidal filaments induced by massive cloud's interactions, and therefore the size of them is limited by a width of the filament. On the other hand, with stellar feedback, they are formed not only in the tidal filaments but also in turbulent warm ISM that is formed from cloud gas dispersions by the stellar feedback. Some *type C* clouds formed in the warm ISM might be more turbulent than those are formed in dense tidal filaments, and then, they have large dispersions in distributions of σ_{1D} and α_{vir} .

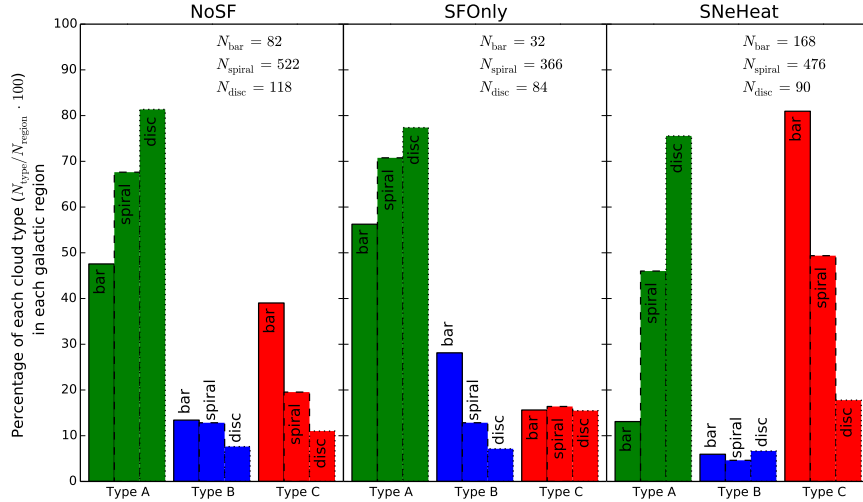


Figure 4.10. The percentages of each cloud type in each galactic region ($= N_{\text{type}}/N_{\text{region}} \times 100$) at $t = 200$ Myr.

The typical values of σ_{1D} of *type A* clouds are 6 km/s in NoSF, 10 km/s in SFOnly and 10 km/s in SNeHeat. This is comparable to 6 km/s characteristic velocity dispersion of the M33 and slightly higher than the Milky Way’s 1 km/s. The typical values of α_{vir} of *type A* clouds are ~ 1 in all three runs, indicating that the majority of the clouds are virialized but only marginally bound. Clouds in the Milky Way are observed to have a slightly lower value of 0.46.

The differences of cloud properties between the three galactic regions are also clarified by using the three cloud types. Fig. 4.10 shows percentages of each cloud type in each galactic region in each simulation at 200 Myr. In NoSF, the percentages of the *type B* and *type C* clouds in the bar region are higher than those in the other regions due to the high cloud density from elliptical gas motion boosting the interaction rate between clouds in the central bar region. In the spiral region, there is the next high fraction of *type B* and *type C* clouds due to the spiral potential encouraging interactions. In the disc region, there is a large population of *type A* clouds due to the lack of the grand design potential to gather gas (see Paper I).

In SFOnly, the main features of the percentages are the same as NoSF; highest fraction of *type B* cloud in the bar region, and highest fraction of *type A* cloud in the disc region. However, there is no difference in the percentages of *type C* cloud between the three regions. As discussed in Fig. 4.9, that is because the total number of *type B* cloud in SFOnly is less than that in NoSF due to gas conversion by star formation. Without stellar feedback, cloud interactions caused by *type B* clouds is the only way to form *type C* clouds. Therefore, although there is a clear difference in the percentages of *type B* cloud in SFOnly, the few *type B* clouds makes their interactions small, and then, the formation of *type C* clouds are suppressed especially in the bar region even though the percentages of the *type B* cloud is highest there.

Also in SNeHeat, the main features of the percentages are the same. However, the difference of the *type C* percentages between the three region is prominent, on the other hand, there is little difference in the *type B* percentages. As discussed in Fig. 4.9, the stellar feedback has strong effect on the formation of the *type C* cloud without formations of dense filaments and tidal tails due to cloud-cloud interactions by *type B* clouds. Therefore, a formation rate of the *type C* clouds is the highest in the bar region where the SFR is highest. The little difference in the *type B* percentages between regions also comes from the high SFRs in the bar and spiral regions; a suppression of the *type B* formation due to a strong star formation and feedback. Moreover, the quite high percentages of the *type C* clouds make it hard to see the difference of the *type B* percentages between the three regions. That is why the *type A* percentages between SFOnly and SNeHeat drastically change with the drastic increases of the *type C* percentages.

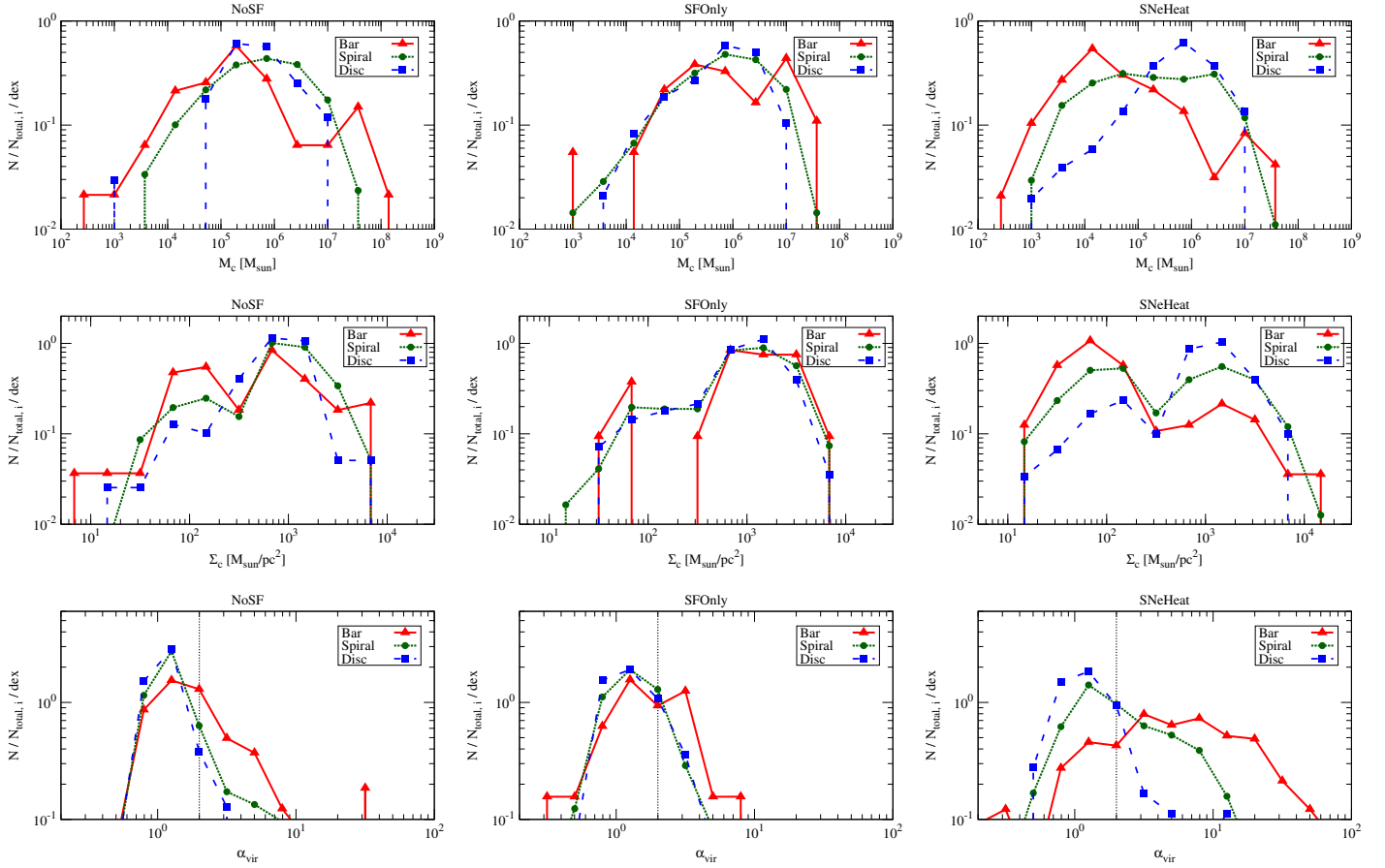


Figure 4.11. Normalised distributions of the cloud properties in the bar region (triangle solid lines), spiral region (circle dotted lines) and disc region (square dashed line) at $t = 200$ Myr. From top to bottom, each row shows the cloud mass, the cloud surface density, $\Sigma_c = M_c/(\pi R_c^2)$ and the virial parameter. From left to right, each column shows NoSF, SFOnly and SNeHeat.

Top panels of Fig. 4.11 show the distributions of cloud mass. The distributions of the bar region considerably change between three runs because of the strong effects of star formation and stellar feedback, while the distributions of the disc region are almost similar where they are least affected by the star formation and stellar feedback. In NoSF, because of the high fraction of *type B* cloud in the bar region, the mass distribution has a bimodal distribution in the bar region. The drop point around $M_c = 5 \times 10^6 M_\odot$ corresponds to $R_c = 30$ pc, which is a borderline between *type A* and *type B* (see Fig. 4.8). Moreover, there is a high mass end tail in the bar region. The bar region also has a low mass end tail because of the high fraction of *type C* cloud. On the other hand, the disc region has a smaller distribution because of the high fraction of *type A* clouds. In SFOnly, because of the star formation, the high mass end tail becomes smaller. Moreover, the low mass end tail also becomes smaller especially in the bar region because of a decrease of the *type C* cloud formation. However, there is still a bimodal distribution in the bar region. In SNeHeat, we see a drastic increase in the low mass part especially in the bar and spiral region where the increase of the *type C* clouds by the stellar feedback is prominent.

Middle panels of Fig. 4.11 show the distributions of cloud surface density. In NoSF, there is a clear bimodal distribution in all regions. The drop points corresponds to $\Sigma_c = 230 M_\odot \text{pc}^{-2}$, which is a borderline between two sequences of the scaling relation of mass versus radius (see Fig. 4.8). Because of the highest fraction of the *type C* in the bar region, the lower surface density part is larger than that of the spiral and disc region. In SFOnly, because of little difference of the percentages of the *type C* cloud in the three regions, bimodality is obscure except the bar region. In SNeHeat, however, the high fraction of *type C* boosted by the stellar feedback makes the bimodality clear. Especially in the bar region, the lower surface density part becomes larger than the higher surface density part. On the other hand, the distribution of the disc region is almost same as that in NoSF because of the low increase of the *type C* cloud.

Bottom panels of Fig. 4.11 show the distributions of virial parameter. In NoSF, almost all clouds in all regions are gravitationally bound (the peak is around $\alpha_{\text{vir}} \sim 1$). The bar region has the high end tail because of the high fraction of *type C* cloud. Also in SFOnly, almost all clouds in all regions are gravitationally bound. However, the width of the distributions slightly gets larger, and the fractions of high α_{vir} increases in all regions because of the increase of the velocity dispersion of clouds as discussed in Fig. 4.8. In SNeHeat, the drastic increase of *type C* cloud makes the distribution different from NoSF or SFOnly; the peak of the bar region is not 1, but 3. Again, that is because of the high fraction of *type C* boosted by the stellar feedback.

4.3.4 The effects of the warm ISM and *type C* clouds on star formation

In this section, using the three cloud types introduced in the previous section, we discuss physical processes of the high SFR in the central bar region induced by the gas inflow in SNeHeat run.

Fig. 4.12 shows relations between the cloud SFR versus mass for SFOnly and SNeHeat. To estimate the SFR for each cloud, we use new formed star particles in previous 1 Myr which is in the cloud's boundary. Features are quite similar between SFOnly and SNeHeat, and we see a clear relation in both runs. Because *type B* clouds are the most massive in the three cloud types, they have the highest SFR. On the other hand, *type C* clouds have no star formation because their mass and density is lowest. To summarize, the *type B* clouds are massive star forming clouds, and the *type C* clouds are no star forming clouds. We see a systematic difference between *type A* and *type B* clouds around $3 \times 10^6 \sim 8 \times 10^6 M_\odot$; *type A* clouds have higher SFR than *type B* clouds even though the cloud mass is comparable. That is come from our definition of the three cloud types; the *type A* and *type B* clouds are separated using cloud radius at $R_c = 30$ pc, not cloud mass. The clouds that sit around the border have similar cloud mass, but they are separated between *type A* and *type B* by the cloud radius. The larger radius clouds are defined as *type B*, and their densities are lower than the *type A* cloud which has similar mass but smaller radius. The denser clouds are, the higher SFR they have, so that

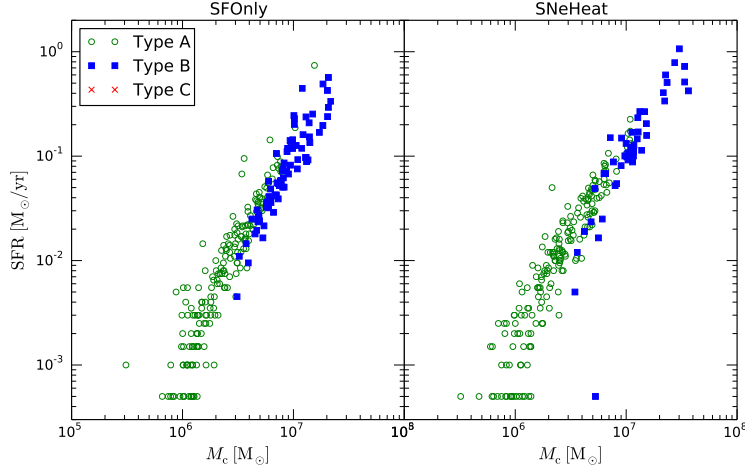


Figure 4.12. Cloud SFR versus cloud mass at $t = 200$ Myr. We counted the total mass of new formed stars in previous 1 Myr.

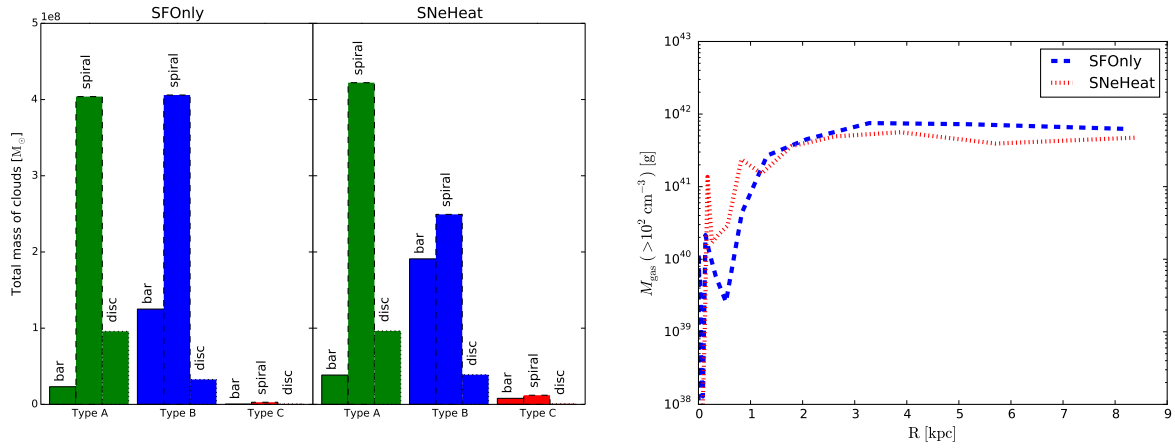


Figure 4.13. Left: total cloud mass of each cloud type in each galactic region at $t = 200$ Myr. Right: radial profile of total gas mass denser than 10^2 cm^{-3} .

type A clouds have higher SFR than *type B* clouds around the mediate mass range. That is why we see the systematic difference between *type A* and *type B* around the same mass range. Finally, we state a slight difference between SFOnly and SNeHeat. In SNeHeat, there are some clouds which have higher SFR and more massive than SFOnly, that is consistent with the massive clouds emerged when the stellar feedback is included as shown in Fig. 4.8. They are located at the central bar region where the gas density gets high and massive cloud's formation is boosted due to the stellar feedback.

Left panel of Fig. 4.13 shows total cloud masses of each cloud type in each galactic region. Compared SNeHeat with SFOnly, the total masses of the *type A* are the almost same in all regions, that is consistent with Fig. 4.9. The total mass of the *type C* slightly increases in the bar and spiral regions because of the high warm ISM formation due to the cloud's gas dispersion by the stellar feedback in the high SFR regions. The total masses of the *type B* changes strangely; the total mass in the spiral region decreases with adding the stellar feedback, however, that in the bar region increases. The sum of the total *type B* cloud mass in all regions slightly decreases with adding the stellar feedback, that is consistent with the slight decrease of the total number of the *type B* clouds when we add the stellar feedback because of cloud destruction due to the feedback as shown in Fig. 4.9. That suggests that the total mass of *type B* clouds decreases especially in the high SFR bar region. However, we get an inverse results; we see the increase of

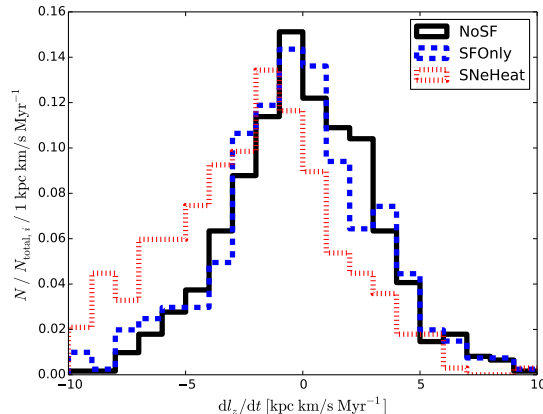


Figure 4.14. Normalised histogram of dl_z/dt , where l_z is a z component of a specific angular momentum of cloud around the galactic centre. Technically, we compared between $t = 199$ and 201 Myr, for example, $dl_z/dt = \{l_z(201 \text{ Myr}) - l_z(199 \text{ Myr})\}/2 \text{ Myr}$. We exclude the *type C* clouds from this distribution.

the total mass of *type B* clouds in the bar region. This suggests that the massive star forming clouds (= *type B* clouds) move from galactic outer region to inner bar region, and then the total mass of the *type B* cloud increases in the bar region. The effect of this inflow of massive *type B* cloud might be stronger than the destruction of them due to the stellar feedback in the central bar region. This cloud inflow was suggested in Section 4.3.1 and 4.3.2.

Right panel of Fig. 4.13 shows radial profile of total gas mass denser than 10^2 cm^{-3} . As same as the left panel, we see a large amount of dense cloud gas in the central bar region ($R < 1 \text{ kpc}$) and, on the other hand, a decrease of the dense gas in outer spiral region ($R > 3 \text{ kpc}$). This panel also suggests the inflows of the massive star forming *type B* clouds toward the galactic central region.

To confirm the inflows of the massive clouds, we analysed an angular momentum loss of *type A* and *type B* clouds. Fig. 4.14 shows a normalised histogram of dl_z/dt , where l_z is a z component of a specific angular momentum of the cloud around the galactic centre. For the calculation, we compared specific angular momenta between $t = 199$ and 201 Myr for each cloud, $dl_z/dt = \{l_z(201 \text{ Myr}) - l_z(199 \text{ Myr})\}/2 \text{ Myr}$. In this distribution, *type A* and *type B* clouds are used, and *type C* clouds are excluded. That is because the cloud's inflow might be occurred only for massive clouds. Actually, Fig. 4.13 shows the cloud inflow of only *type B* clouds. In NoSF and SFOnly, the peak is at $dl_z/dt = 0$. That shows no angular momentum loss of the clouds. On the other hand, in SNeHeat, the peak is slightly shifted to the left, and the minus part is larger than the plus part. It indicates that the clouds tend to lose their specific angular momentum when the stellar feedback is included. This results clearly shows the inflows of the massive star forming clouds into the galactic centre in SNeHeat.

A plausible physical process of the specific angular momentum loss is a drag (or fluid resistance), which acts opposite to the cloud motion with respect to the surrounding ISM. The drag force, \mathbf{F}_{drag} , is defined as,

$$\mathbf{F}_{\text{drag}} = \frac{1}{2} D \rho (\mathbf{v} - \mathbf{v}_c)^2 A \frac{\mathbf{v} - \mathbf{v}_c}{|\mathbf{v} - \mathbf{v}_c|}, \quad (4.4)$$

where D is a drag coefficient, ρ is the density of the surrounding ISM of the cloud, \mathbf{v} is the velocity of the ISM, \mathbf{v}_c is the cloud velocity, and A is a cross sectional area of the cloud. As discussed in the previous sections, the prominent difference between with and without the stellar feedback is formations of the warm ISM and *type C* clouds; the ISM density and the formation rate of the *type C* clouds get high when the stellar feedback is included. Therefore, the drag is the strongest candidate for a physical process of the specific angular momentum loss in SNeHeat; the higher density the ISM has, the stronger drag acts on the clouds, and then the larger angular momentum they lose.

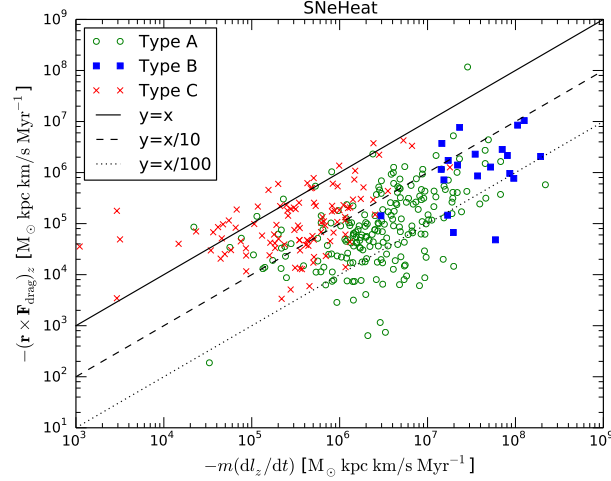


Figure 4.15. Relation of $-(\mathbf{r} \times \mathbf{F}_{\text{drag}})_z$ versus $-m(dl_z/dt)$ for each cloud. The green circles are the *type A* clouds, the blue squares are the *type B* clouds, and the red x are the *type C* clouds.

We estimated the drag force for each cloud and compared them with the angular momentum loss for each clouds. In the estimation of the drag force for each cloud, the cross sectional area is calculated as $A = \pi R_c^2$. For rigid bodies, Newton's second law for rotation is,

$$\begin{aligned}
 \mathbf{r} \times \mathbf{F}_{\text{drag}} &= \frac{d}{dt} \mathbf{L} \\
 &= \frac{d}{dt} (m\mathbf{l}) \\
 &= m \frac{d\mathbf{l}}{dt} + \mathbf{l} \frac{dm}{dt},
 \end{aligned} \tag{4.5}$$

where \mathbf{r} is a radial position of the cloud, \mathbf{L} is a angular momentum ($\mathbf{L} = m \mathbf{r} \times \mathbf{v}$), and \mathbf{l} is a specific angular momentum ($\mathbf{l} = \mathbf{r} \times \mathbf{v}$). The clouds are not rigid bodies because the stellar feedback may blow a part of the gas away, or the star formation eats their gas, or the drag force would shave the surface of the cloud. We checked normalised histogram of mass loss rate of clouds, $dm/dt = \{M_c(201 \text{ Myr}) - M_c(199 \text{ Myr})\}/2 \text{ Myr}$. In the NoSF and SFOnly, the peak is at $dm/dt = 0$, but SNeHeat shows the peak is at $dm/dt \sim -10^4 M_\odot$, which indicates that clouds lose their mass when the stellar feedback is included. Therefore, we could not ignore the mass loss term, $\mathbf{l}(dm/dt)$. In fact, the typical absolute value of the $l_z(dm/dt)$ is about one order of magnitude greater than that of the $m(dl_z/dt)$.

In order to make sure whether the specific angular momentum loss is induced by the drag, we made a relation plot between $-(\mathbf{r} \times \mathbf{F}_{\text{drag}})_z$ and $-m(dl_z/dt)$ for each cloud without the mass loss term, $l_z(dm/dt)$, as shown in Fig. 4.15. The two values are less than 0, so that we multiplied minus by them. Although $-(\mathbf{r} \times \mathbf{F}_{\text{drag}})_z$ is about one order of magnitude less than $-m(dl_z/dt)$, there is a clear scaling relation in *type A* and *type B* clouds. The estimation of the drag force might have some error. For example, the actual cross sectional area, A , may have larger than that we used, but it is hard to decide it because the actual clouds do not have a clear boundary. Moreover, we do not know the exact value of the drag coefficient, D . However, we argue that the *type A* and *type B* clouds lose their angular momentum due to a drag because there is a clear scaling relation. With regard to *type C* clouds, they are not on the relation, which indicate that the angular momentum loss by a drag does not apply to them. That is consistent with Fig. 4.13, which shows the cloud inflow of only massive *type B* clouds.

Although previous works have investigated effects of stellar feedback on GMCs, this process of cloud's inflow have never been reported. That might be because Dobbs et al. (2006, 2011b); Williamson et al. (2014) used SPH (smoothed particle hydrodynamics), which algorithm has a

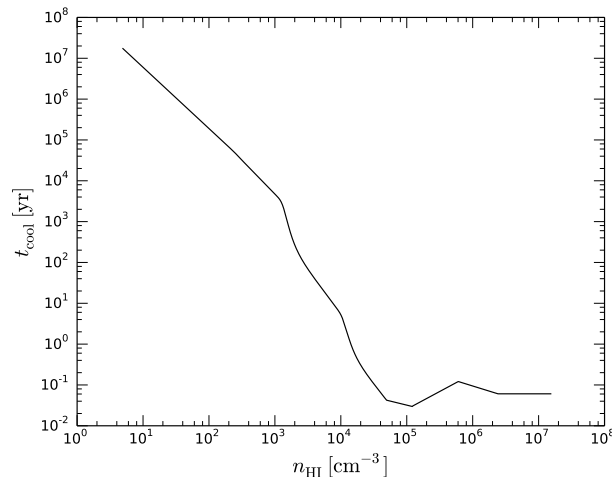


Figure 4.16. Cooling time of a cell which is injected thermal energy from stellar feedback depending on the gas density of the cell.

difficulty to trace a low density gas motion. In the process of the cloud’s inflow, the low density ISM surrounding clouds acts on increase of the drag force, so that it is important to trace the low density gas motion.

Clouds could lose their angular momentum through another physical process. Zasov and Khoperskov (2015) showed that clouds could drop toward the galactic central region through dynamical friction between clouds, but they stated that lifetime of the clouds must be greater than 100 Myr, that is inconsistent with observational estimate ($5 \sim 30$ Myr. e.g. Kawamura et al. 2009; Miura et al. 2012) and our results (typically less than 10 Myr).

To summarise, the stellar feedback raises the density of the ISM, and massive clouds (especially *type B* clouds) lose their specific angular momentum due to a strong drag induced by the high density of ISM. The inflows of the massive clouds supply a huge amount of the gas to the galactic central region, and the high SFRs of the massive clouds raise the SFR in the bar region.

4.4 Discussions

4.4.1 Estimation of the feedback effects

We showed the stellar feedback effects on the ISM, the giant molecular clouds and star formation in the previous sections. In this section, we discuss them using the cooling time estimation of the injected feedback energy.

Fig. 4.16 shows the estimation of a cooling time of a cell which is injected thermal energy from stellar feedback depending on the density of the cell. The cooling time for the density of 10^4 cm^{-3} , which is the threshold density for star formation of our recipe, is only a few years. It is shorter than time step of our simulation ($dt \sim 10^5$ year). Therefore, our stellar feedback seems to cool immediately and not to affect on the ISM. However, we include the thermal energy into not only the star forming cell but also surrounding cells, which might have lower density than the star forming cells. If the surrounding cells have 10^2 cm^{-3} , the cooling time is several 10^5 years, which is comparable to the time step of this simulation. Some fraction of the feedback energy seems to keep in the surrounding cells. In fact, the stellar feedback affects on the ISM, the giant molecular clouds and the star formation as we showed in the previous section.

The overcooling is a well-known problem in galaxy simulations (e.g. Stinson et al. 2006). Also in this simulation, the feedback energy overcools in the cells which have the density larger than 10^3 cm^{-3} . That means that the effects of our stellar feedback is a lower limit. However,

our main results would not change so much. With more stronger feedback, the density of the ISM and the formation of the *type C* clouds might increase. Although large fraction of the *type B* clouds would be destroyed by the strong feedback, there might still be inflows of the massive clouds into the galactic centre because of the high density of the ISM.

4.5 Conclusions

We performed a M83-type barred spiral galaxy simulations with thermal stellar feedback and investigated the impact of the thermal stellar feedback on the ISM, the giant molecular clouds and the star formation. To understand effects of the stellar feedback on cloud properties, we classified all clouds into three types via mass-radius scaling relation, which we label *A*, *B* and *C*. *Type A* clouds have the typical values of cloud properties: mass, radius, 1D velocity dispersion. *Type B* clouds are massive giant molecular associations (GMAs). *Type C* clouds are unbound, transient clouds. Our main results are as follows.

1. The stellar feedback disperses some fraction of the gas of the clouds into the inter-cloud region, and raises the density of the ISM.
2. The stellar feedback affects the formation of the *type C* small transient clouds. Without the stellar feedback, the *type C* clouds are formed in the dense filaments and tidal tails that are induced by the *type B* massive clouds interactions. With the stellar feedback, the *type C* clouds are formed in the warm ISM, and more *type Cs* are formed compared with no feedback case.
3. Massive clouds (especially *type B* clouds) lose their specific angular momentum due to a strong drag induced by the high density ISM. The inflows of the massive clouds towards the galactic centre supply a huge amount of the gas to the central bar region.
4. The SFR of the bar region gets higher when the stellar feedback is included because the high SFR massive clouds (mainly *type B* clouds) drop into the central bar region.

Chapter 5

Conclusion

Understanding where and how gas is converted into stars in a galaxy is important for understanding a galaxy's formation and evolution through each epoch of the universe. Which physical processes control the star formation in a galaxy is heavily debated.

Recent observations have shown the star formation activity changing between galactic-scale environments. The star formation efficiencies (SFEs) have systematic variations larger than one order of magnitude between different galaxy types and between different regions within a galaxy. This means that the gas density is not the only factor that determines the star formation activity in a galaxy. In particular, observations of barred galaxies showed that a central bar region has a lower SFE than that in the spiral arm regions even when the gas surface densities are almost the same.

Why does the star formation activity differ depending on the galactic structure's different environments? To understand this, it is important to investigate how the formation and evolution of GMCs is affected by the galactic structures. This is because the GMCs are the star formation spots in a galaxy; their densest pockets are the birth place of stars.

We performed three-dimensional hydrodynamical simulations of a barred spiral galaxy, and investigated GMC formation and evolution. The main conclusions are as follows.

1. The GMC distributions and properties are different between the three galactic regions, primarily due to different cloud interaction rates. In the central bar region, massive giant molecular associations are formed due to a high cloud number density from the elliptical motion boosting interactions between clouds. The violent cloud-cloud interactions form dense tidal filamentary structures around them, which produce gravitationally unbound transient clouds in the filaments. In the outer-disc regions, clouds are more widely spaced and lack filament structures due to the absence of the grand design potential to gather gas and produce less cloud-cloud interactions. Spiral regions have intermediate features.
2. The collision velocity shows a clear dependence on galactic environment. Clouds formed in the bar region typically collide faster than those in the spiral. Such speeds can be unproductive for star formation, as the collision is over too quickly for gas to collapse. The unproductive collisions in the bar region lower the SFE to put it below the maximum efficiency in the spiral region, as seen in observations.
3. The stellar feedback disperses part of the cloud gas, and the ISM density in the inter-cloud region increases. The high inter-cloud density causes angular momentum loss of clouds due to hydrodynamical drag. Massive clouds lose their angular momentum due to the torque from the hydrodynamical drag. They inflow toward the galactic centre, and then the total gas density in the central bar region rises. This gas supply would be important for evolution of the galaxy centre.

We clarified that galactic environments and stellar feedbacks affect GMC formation and evolution, and that could explain the different star formation activities in a barred spiral galaxy.

Chapter 6

Future Prospects

My main research interests are in galactic-scale star formation. Understanding where and how gas is converted into stars affects every scale in astrophysics. In particular, it fills the gap between cosmological-scale galaxy formation and small-scale star formation in molecular cloud cores.

What is the physical process that control a galaxy's star formation? Recent observations have shown that the star formation activity changes between galactic-scale environments: different galaxy types and different regions within a galaxy (e.g. Daddi et al. 2010b; Genzel et al. 2010; Leroy et al. 2013). This is key to understanding massive core formation because the galactic-scale star formation rates almost entirely come from the activity of massive stars.

In particular, cloud-cloud collisions are strong candidates for triggering the massive cloud core formation; the compressed region made in the collision can form the massive cloud core that could collapse to massive stars. Recent observations of our galaxy and simulations have shown the massive core and star formations via collisions (e.g. Fukui et al. 2014; Takahira et al. 2014)

I think that the features of the cloud-cloud collisions, e.g. collision rates, cloud masses, and collision velocities, could be different between the galactic environments, and the difference would cause the star formation activities to change between galactic-scale environments.

In my Ph.D. projects, I have investigated the formation and evolution of the giant molecular cloud (GMC) in a barred spiral galaxy, performing three-dimensional hydrodynamical simulations of an M83-type galaxy (Fujimoto et al. 2014a,b; Fujimoto et al. 2015). The simulation code I used was *Enzo* (Bryan et al., 2014), a 3D hydrodynamics code that uses adaptive mesh refinement (AMR). I have shown that the GMC formation and evolution are different between the galactic regions (bar, spiral arms, disc), and the difference in the cloud-cloud collisions can explain the observational result of different star formation activity between the bar and spiral regions.

In my future research, I would like to investigate two things: [1] the stellar feedback effects on the GMC evolution and [2] the galactic environmental effects on the GMC evolution. The details are as follows.

6.1 Stellar feedback effects on the GMC evolution

In my previous work in Fujimoto et al. (2015), we included only thermal stellar feedback. I would like to upgrade the feedback model. Many other works have been tackling the stellar feedback effects on the ISM and unresolved star formation. My particular interest is to focus on the GMC formation and evolution. The GMCs are the star formation spots, and they are the key to understanding galactic scale star formation. Moreover, cloud-cloud collisions are a strong candidate for massive star formation, and therefore to investigate the statistical GMC evolution is a fundamental way to understand the initial mass function (IMF). The detailed plans are as follows.

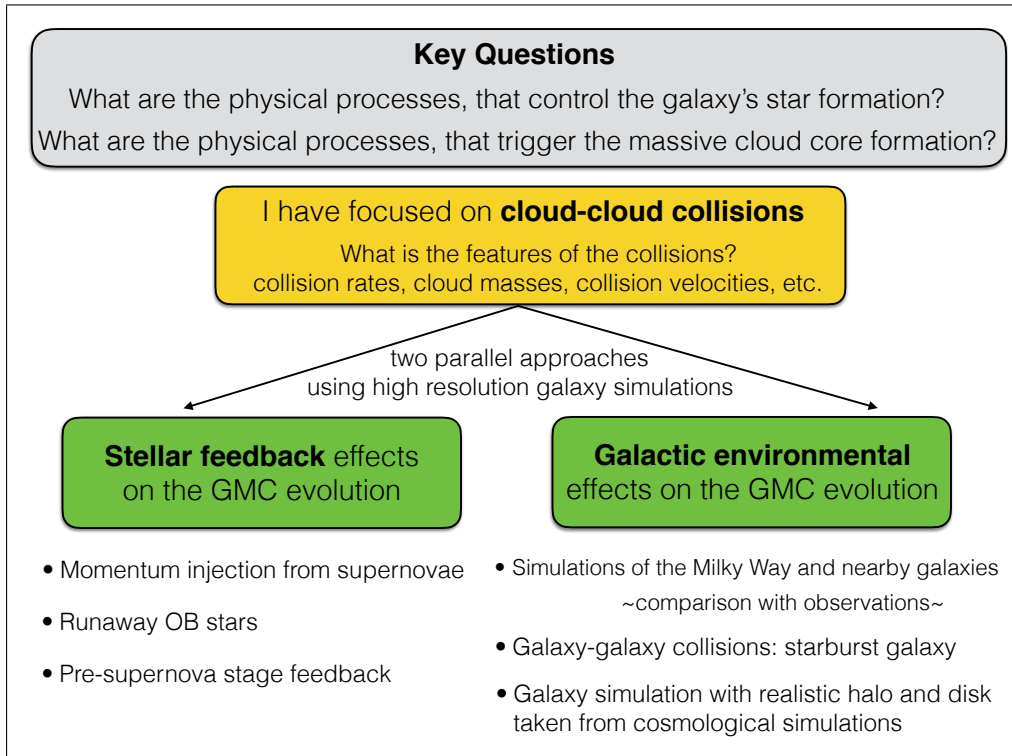


Figure 6.1. Schematic diagram of my research plan

(1) Momentum injection from supernova explosions

The physical process of supernova feedback is mediated by the evolution of the supernova remnant. The supernova remnant evolves via four stages: free expansion, adiabatic expansion, pressure driven snowplough and the momentum conserving phase. In the adiabatic expansion phase, also known as the Sedov-Taylor phase, the input energy from the supernova is eventually distributed into the ISM as thermal and kinetic energy of the gas, with an energy ratio of about 7 : 3. After the adiabatic expansion phase, the thermal energy drops and is almost entirely lost due to radiative cooling, as the post-shocked region is very dense. On the other hand, the overall fraction of kinetic energy does not decrease. Therefore, it is important to include not only thermal energy but also momentum injection into our stellar feedback model; Fujimoto et al. (2015) included only thermal supernovae feedback. Simpson et al. (2015) developed a new routine for the momentum injection in *Enzo*. Using this routine, I would like to investigate GMC evolutions in our simulated barred galaxy with the effective stellar feedback.

(2) Runaway OB stars effects

Type II supernova progenitors are massive OB stars. Although most of the OB stars have low space velocities with which they can only travel several tens of parsecs away from their birth cloud, 5-30 % of OB stars in the Milky Way are runaway stars, which have large velocity enough to escape their birth clouds. Therefore, these runaway massive stars explode in the diffuse ISM, rather than the densest gas. Gatto et al. (2015) showed that the supernova explosion in the diffuse gas strongly affects the surrounding ISM due to ineffective radiative cooling compared with the case where the supernovae explosion occurs only in the dense cloud core. I would like to develop the star formation routine to make a fraction of star particles have a large velocity, and investigate the effects on GMCs evolutions in the galaxy.

(3) Pre-supernova stage feedback

The pre-supernova stellar feedback also affects the ISM in a galaxy (Hopkins et al., 2011, 2012; Agertz et al., 2013). The newly formed star emits UV radiation and stellar winds, and forms HII regions due to the ionisation of the ISM by the UV radiation from the central star. The

radiation pressure, stellar winds and thermal pressure of the HII region inputs momentum to the ISM around it. These processes should be included into my model as well as the supernovae-driven stellar feedback.

6.2 Galactic environmental effects on the GMC evolution

In our current works, we modelled the barred spiral galaxy, M83, and investigated features of the GMCs between galactic regions in the galaxy. Another area I would be interested in is to simulate other types of galaxies, and compare the galactic environmental effects of GMC and star formation. Such differences have been seen in observational results showing different star formation activities between different galaxy types (e.g. Daddi et al. 2010b; Genzel et al. 2010; Leroy et al. 2013).

(1) Milky Way

An obvious candidate is to perform a Milky Way-type galaxy simulation and investigate GMC formation and evolution. The Milky Way is our nearest galaxy, so that we have excellent data resolving down to the cloud core scale. Therefore, the Milky Way is one of the best target to investigate star formation and GMC properties. In our galaxy, candidates for cloud-cloud collisions have been observed, which is still impossible in nearby galaxies (e.g., Fukui et al. 2014). However the number is low because of a difficulty in identifying the collisions in observations. Moreover, it is also hard to identify in which galactic structure the observed region is located because we are in the disc of our galaxy. My simulation studies could statistically investigate the features of the cloud evolutions between galactic regions comparing with the well-resolved observations. For the galaxy modelling, I will use a stellar potential developed in Pettitt et al. (2014), who investigated the morphology of the Milky Way comparing longitude-velocity maps with observations. The stellar potential has realistic galactic structures, i.e. four strong spiral arms and central multi-bar structure, so that we could investigate the effects of the galactic structures on GMC evolution, which are hard to investigate in observations.

(2) Nearby galaxies

M51 is a grand design spiral galaxy, which has strong spiral arms. This object is good for investigating the strong spiral arm effects on GMCs. M51 has been observed with many instruments at multiple wavelengths, and there is good data for setting the initial conditions for a galactic model and for comparing with our simulation results (e.g. Koda et al. 2009; Meidt et al. 2013).

M33 is a spiral galaxy with weak spiral arms. This galaxy has also been extensively observed, including properties of the GMC population that can be compared with simulations (e.g. Rosolowsky et al. 2003; Rosolowsky 2007; Miura et al. 2012; Gratier et al. 2012). In combination with the M51 simulation and high resolution observations, I will try to understand the spiral arm effects on GMCs and star formation in detail.

(3) Starburst galaxies: galaxy-galaxy collision

Why do starburst galaxies at high redshift have one order of magnitude higher SFRs than that of normal galaxies? They are expected to be merging galaxies, creating compressed regions of high star formation activity at the site of the galaxy mergers. However, the detail of the physical process has been debated. I would like to perform merging galaxy simulation, and investigate how the cloud-cloud collisions could be excited at the shocked front.

(4) Realistic galaxy model: with a dark matter halo and stellar distributions clipped from cosmological simulations

Galaxy evolution is not quiescent but consists of a violent history of mergers and interactions. It would be interesting to investigate the GMC formation and evolution with more realistic dark matter and stellar distributions. I would like to perform cosmological simulations or to use a galaxy catalogue performed by other projects, and then I would like to perform higher

resolution simulations with the realistic dark matter and stellar distributions, clipped from the cosmological simulations.

Bibliography

- O. Agertz, A. V. Kravtsov, S. N. Leitner, and N. Y. Gnedin. Toward a Complete Accounting of Energy and Momentum from Stellar Feedback in Galaxy Formation Simulations. *ApJ*, 770:25, June 2013. doi: 10.1088/0004-637X/770/1/25.
- S. V. Anathpindika. Collision between dissimilar clouds: stability of the bow-shock, and the formation of pre-stellar cores. *MNRAS*, 405:1431–1443, July 2010. doi: 10.1111/j.1365-2966.2010.16541.x.
- E. Athanassoula. The existence and shapes of dust lanes in galactic bars. *MNRAS*, 259:345–364, Nov. 1992.
- J. Baba. Short-term dynamical evolution of grand-design spirals in barred galaxies. *MNRAS*, 454:2954–2964, Dec. 2015. doi: 10.1093/mnras/stv2220.
- J. Baba, Y. Asaki, J. Makino, M. Miyoshi, T. R. Saitoh, and K. Wada. The Origin of Large Peculiar Motions of Star-Forming Regions and Spiral Structures of Our Galaxy. *ApJ*, 706:471–481, Nov. 2009. doi: 10.1088/0004-637X/706/1/471.
- J. Baba, T. R. Saitoh, and K. Wada. Dynamics of Non-steady Spiral Arms in Disk Galaxies. *ApJ*, 763:46, Jan. 2013. doi: 10.1088/0004-637X/763/1/46.
- J. Ballesteros-Paredes, A. Gazol, J. Kim, R. S. Klessen, A.-K. Jappsen, and E. Tejero. The Mass Spectra of Cores in Turbulent Molecular Clouds and Implications for the Initial Mass Function. *ApJ*, 637:384–391, Jan. 2006. doi: 10.1086/498228.
- N. Bastian, A. Adamo, M. Gieles, E. Silva-Villa, H. J. G. L. M. Lamers, S. S. Larsen, L. J. Smith, I. S. Konstantopoulos, and E. Zackrisson. Stellar clusters in M83: formation, evolution, disruption and the influence of the environment. *MNRAS*, 419:2606–2622, Jan. 2012. doi: 10.1111/j.1365-2966.2011.19909.x.
- S. M. Benincasa, E. J. Tasker, R. E. Pudritz, and J. Wadsley. Giant Molecular Cloud Formation in Disk Galaxies: Characterizing Simulated versus Observed Cloud Catalogs. *ApJ*, 776:23, Oct. 2013. doi: 10.1088/0004-637X/776/1/23.
- G. Bertin and C. C. Lin. *Spiral structure in galaxies a density wave theory*. 1996.
- F. Bertoldi and C. F. McKee. Pressure-confined clumps in magnetized molecular clouds. *ApJ*, 395:140–157, Aug. 1992. doi: 10.1086/171638.
- F. Bigiel, A. Leroy, F. Walter, E. Brinks, W. J. G. de Blok, B. Madore, and M. D. Thornley. The Star Formation Law in Nearby Galaxies on Sub-Kpc Scales. *AJ*, 136:2846–2871, Dec. 2008. doi: 10.1088/0004-6256/136/6/2846.
- J. Binney and S. Tremaine. *Galactic Dynamics: Second Edition*. Princeton University Press, 2008.
- W. P. Blair, P. F. Winkler, and K. S. Long. The Magellan/IMACS Catalog of Optical Supernova Remnant Candidates in M83. *ApJS*, 203:8, Nov. 2012. doi: 10.1088/0067-0049/203/1/8.
- L. Blitz, Y. Fukui, A. Kawamura, A. Leroy, N. Mizuno, and E. Rosolowsky. Giant Molecular Clouds in Local Group Galaxies. *Protostars and Planets V*, pages 81–96, 2007.
- R. C. Bohlin, R. H. Cornett, J. K. Hill, A. M. Smith, and T. P. Stecher. Images in the rocket ultraviolet - The starburst in the nucleus of M83. *ApJL*, 274:L53–L56, Nov. 1983. doi: 10.1086/184149.
- A. D. Bolatto, A. K. Leroy, E. Rosolowsky, F. Walter, and L. Blitz. The Resolved Properties of Extragalactic Giant Molecular Clouds. *ApJ*, 686:948–965, Oct. 2008. doi: 10.1086/591513.
- W. B. Bonnor. Boyle’s Law and gravitational instability. *MNRAS*, 116:351, 1956. doi: 10.1093/mnras/116.3.351.
- M. S. Bothwell, R. C. Kennicutt, and J. C. Lee. On the interstellar medium and star formation demographics of galaxies in the local universe. *MNRAS*, 400:154–167, Nov. 2009. doi: 10.1111/j.1365-2966.2009.15471.x.
- N. Bouché, G. Cresci, R. Davies, F. Eisenhauer, N. M. Förster Schreiber, R. Genzel, S. Gillessen, M. Lehnert, D. Lutz, N. Nesvadba, K. L. Shapiro, A. Sternberg, L. J. Tacconi, A. Verma, A. Cimatti, E. Daddi, A. Renzini,

- D. K. Erb, A. Shapley, and C. C. Steidel. Dynamical Properties of $z \sim 2$ Star-forming Galaxies and a Universal Star Formation Relation. *ApJ*, 671:303–309, Dec. 2007. doi: 10.1086/522221.
- G. L. Bryan, M. L. Norman, B. W. O’Shea, T. Abel, J. H. Wise, M. J. Turk, D. R. Reynolds, D. C. Collins, P. Wang, S. W. Skillman, B. Smith, R. P. Harkness, J. Bordner, J.-h. Kim, M. Kuhlen, H. Xu, N. Goldbaum, C. Hummels, A. G. Kritsuk, E. Tasker, S. Skory, C. M. Simpson, O. Hahn, J. S. Oishi, G. C. So, F. Zhao, R. Cen, Y. Li, and Enzo Collaboration. ENZO: An Adaptive Mesh Refinement Code for Astrophysics. *ApJS*, 211:19, Apr. 2014. doi: 10.1088/0067-0049/211/2/19.
- R. Cen and J. P. Ostriker. Galaxy formation and physical bias. *ApJL*, 399:L113–L116, Nov. 1992. doi: 10.1086/186620.
- G. Chabrier. The Galactic Disk Mass Function: Reconciliation of the Hubble Space Telescope and Nearby Determinations. *ApJL*, 586:L133–L136, Apr. 2003. doi: 10.1086/374879.
- R. Chandar, B. C. Whitmore, H. Kim, C. Kaleida, M. Mutchler, D. Calzetti, A. Saha, R. O’Connell, B. Balick, H. Bond, M. Carollo, M. Disney, M. A. Dopita, J. A. Frogel, D. Hall, J. A. Holtzman, R. A. Kimble, P. McCarthy, F. Paresce, J. Silk, J. Trauger, A. R. Walker, R. A. Windhorst, and E. Young. The Luminosity, Mass, and Age Distributions of Compact Star Clusters in M83 Based on Hubble Space Telescope/Wide Field Camera 3 Observations. *ApJ*, 719:966–978, Aug. 2010. doi: 10.1088/0004-637X/719/1/966.
- D. Colombo, A. Hughes, E. Schinnerer, S. E. Meidt, A. K. Leroy, J. Pety, C. L. Dobbs, S. García-Burillo, G. Dumas, T. A. Thompson, K. F. Schuster, and C. Kramer. The PdBI Arcsecond Whirlpool Survey (PAWS): Environmental Dependence of Giant Molecular Cloud Properties in M51. *ApJ*, 784:3, Mar. 2014. doi: 10.1088/0004-637X/784/1/3.
- F. Combes, F. Debbasch, D. Friedli, and D. Pfenniger. Box and peanut shapes generated by stellar bars. *A&A*, 233:82–95, July 1990.
- L. P. Crosthwaite, J. L. Turner, L. Buchholz, P. T. P. Ho, and R. N. Martin. CO in the Disk of the Barred Spiral Galaxy M83: CO (1-0), CO (2-1), and Neutral Gas. *AJ*, 123:1892–1912, Apr. 2002. doi: 10.1086/339479.
- E. Daddi, F. Bournaud, F. Walter, H. Dannerbauer, C. L. Carilli, M. Dickinson, D. Elbaz, G. E. Morrison, D. Riechers, M. Onodera, F. Salmi, M. Krips, and D. Stern. Very High Gas Fractions and Extended Gas Reservoirs in $z = 1.5$ Disk Galaxies. *ApJ*, 713:686–707, Apr. 2010a. doi: 10.1088/0004-637X/713/1/686.
- E. Daddi, D. Elbaz, F. Walter, F. Bournaud, F. Salmi, C. Carilli, H. Dannerbauer, M. Dickinson, P. Monaco, and D. Riechers. Different Star Formation Laws for Disks Versus Starbursts at Low and High Redshifts. *ApJL*, 714:L118–L122, May 2010b. doi: 10.1088/2041-8205/714/1/L118.
- A. Dalgarno and R. A. McCray. Heating and Ionization of HI Regions. *ARA&A*, 10:375, 1972. doi: 10.1146/annurev.aa.10.090172.002111.
- T. M. Dame, D. Hartmann, and P. Thaddeus. The Milky Way in Molecular Clouds: A New Complete CO Survey. *ApJ*, 547:792–813, Feb. 2001. doi: 10.1086/318388.
- S. Dib, G. Helou, T. J. T. Moore, J. S. Urquhart, and A. Dariush. The Lesser Role of Shear in Galactic Star Formation: Insight from the Galactic Ring Survey. *ApJ*, 758:125, Oct. 2012. doi: 10.1088/0004-637X/758/2/125.
- S. Dib, J. Gutkin, W. Brandner, and S. Basu. Feedback-regulated star formation - II. Dual constraints on the SFE and the age spread of stars in massive clusters. *MNRAS*, 436:3727–3740, Dec. 2013. doi: 10.1093/mnras/stt1857.
- J. R. Dickel, H. R. Dickel, and W. J. Wilson. The detailed structure of CO in molecular cloud complexes. II - The W75-DR 21 region. *ApJ*, 223:840–853, Aug. 1978. doi: 10.1086/156317.
- C. L. Dobbs and I. A. Bonnell. Spurs and feathering in spiral galaxies. *MNRAS*, 367:873–878, Apr. 2006. doi: 10.1111/j.1365-2966.2006.10146.x.
- C. L. Dobbs and J. E. Pringle. The exciting lives of giant molecular clouds. *MNRAS*, 432:653–667, June 2013. doi: 10.1093/mnras/stt508.
- C. L. Dobbs, I. A. Bonnell, and J. E. Pringle. The formation of molecular clouds in spiral galaxies. *MNRAS*, 371:1663–1674, Oct. 2006. doi: 10.1111/j.1365-2966.2006.10794.x.
- C. L. Dobbs, C. Theis, J. E. Pringle, and M. R. Bate. Simulations of the grand design galaxy M51: a case study for analysing tidally induced spiral structure. *MNRAS*, 403:625–645, Apr. 2010. doi: 10.1111/j.1365-2966.2009.16161.x.
- C. L. Dobbs, A. Burkert, and J. E. Pringle. Why are most molecular clouds not gravitationally bound? *MNRAS*, 413:2935–2942, June 2011a. doi: 10.1111/j.1365-2966.2011.18371.x.
- C. L. Dobbs, A. Burkert, and J. E. Pringle. The properties of the interstellar medium in disc galaxies with stellar feedback. *MNRAS*, 417:1318–1334, Oct. 2011b. doi: 10.1111/j.1365-2966.2011.19346.x.

- J. Donovan Meyer, J. Koda, R. Momose, T. Mooney, F. Egusa, M. Carty, R. Kennicutt, N. Kuno, D. Rebolledo, T. Sawada, N. Scoville, and T. Wong. Resolved Giant Molecular Clouds in Nearby Spiral Galaxies: Insights from the CANON CO (1-0) Survey. *ApJ*, 772:107, Aug. 2013. doi: 10.1088/0004-637X/772/2/107.
- M. A. Dopita, W. P. Blair, K. S. Long, M. Mutchler, B. C. Whitmore, K. D. Kuntz, B. Balick, H. E. Bond, D. Calzetti, M. Carollo, M. Disney, J. A. Frogel, R. O’Connell, D. Hall, J. A. Holtzman, R. A. Kimble, J. MacKenty, P. McCarthy, F. Paresce, A. Saha, J. Silk, M. Sirianni, J. Trauger, A. R. Walker, R. Windhorst, and E. Young. Supernova Remnants and the Interstellar Medium of M83: Imaging and Photometry with the Wide Field Camera 3 on the Hubble Space Telescope. *ApJ*, 710:964–978, Feb. 2010. doi: 10.1088/0004-637X/710/2/964.
- D. Downes, D. Reynaud, P. M. Solomon, and S. J. E. Radford. CO in the Barred Galaxy NGC 1530. *ApJ*, 461:186, Apr. 1996. doi: 10.1086/177046.
- R. Ebert. Über die Verdichtung von H I-Gebieten. Mit 5 Textabbildungen. *ZAp*, 37:217, 1955.
- G. Engargiola, R. L. Plambeck, E. Rosolowsky, and L. Blitz. Giant Molecular Clouds in M33. I. BIMA All-Disk Survey. *ApJS*, 149:343–363, Dec. 2003. doi: 10.1086/379165.
- D. Espada, S. Komugi, E. Muller, K. Nakanishi, M. Saito, K. Tatematsu, S. Iguchi, T. Hasegawa, N. Mizuno, D. Iono, S. Matsushita, A. Trejo, E. Chapillon, S. Takahashi, Y. N. Su, A. Kawamura, E. Akiyama, M. Hiramatsu, H. Nagai, R. E. Miura, Y. Kurono, T. Sawada, A. E. Higuchi, K. Tachihara, K. Saigo, and T. Kamazaki. Giant Molecular Clouds and Star Formation in the Tidal Molecular Arm of NGC 4039. *ApJL*, 760:L25, Dec. 2012. doi: 10.1088/2041-8205/760/2/L25.
- K. Fathi, J. E. Beckman, A. A. Lundgren, C. Carignan, O. Hernandez, P. Amram, P. Balard, J. Boulesteix, J.-L. Gach, J. H. Knapen, and M. Relaño. Spiral Inflow Feeding the Nuclear Starburst in M83, Observed in H α Emission with the GH α FaS Fabry-Perot Interferometer. *ApJL*, 675:L17–L20, Mar. 2008. doi: 10.1086/527473.
- G. B. Field. Thermal Instability. *ApJ*, 142:531, Aug. 1965. doi: 10.1086/148317.
- G. B. Field, D. W. Goldsmith, and H. J. Habing. Cosmic-Ray Heating of the Interstellar Gas. *ApJL*, 155:L149, Mar. 1969. doi: 10.1086/180324.
- N. M. Förster Schreiber, R. Genzel, N. Bouché, G. Cresci, R. Davies, P. Buschkamp, K. Shapiro, L. J. Tacconi, E. K. S. Hicks, S. Genel, A. E. Shapley, D. K. Erb, C. C. Steidel, D. Lutz, F. Eisenhauer, S. Gillessen, A. Sternberg, A. Renzini, A. Cimatti, E. Daddi, J. Kurk, S. Lilly, X. Kong, M. D. Lehnert, N. Nesvadba, A. Verma, H. McCracken, N. Arimoto, M. Mignoli, and M. Onodera. The SINS Survey: SINFONI Integral Field Spectroscopy of $z \sim 2$ Star-forming Galaxies. *ApJ*, 706:1364–1428, Dec. 2009. doi: 10.1088/0004-637X/706/2/1364.
- K. Foyle, G. Natale, C. D. Wilson, C. C. Popescu, M. Baes, G. J. Bendo, M. Boquien, A. Boselli, A. Cooray, D. Cormier, I. De Looze, J. Fischera, O. L. Karczewski, V. Lebouteiller, S. Madden, M. Pereira-Santaella, M. W. L. Smith, L. Spinoglio, and R. J. Tuffs. Star formation and dust heating in the FIR bright sources of M83. *MNRAS*, 432:2182–2207, July 2013. doi: 10.1093/mnras/stt618.
- M. Fujimoto. Motion of Gas and Spiral Structure. *ApJ*, 152:391, May 1968. doi: 10.1086/149556.
- Y. Fujimoto, E. J. Tasker, M. Wakayama, and A. Habe. Do giant molecular clouds care about the galactic structure? *MNRAS*, 439:936–953, Mar. 2014a. doi: 10.1093/mnras/stu014.
- Y. Fujimoto, E. J. Tasker, and A. Habe. Environmental dependence of star formation induced by cloud collisions in a barred galaxy. *MNRAS*, 445:L65–L69, Nov. 2014b. doi: 10.1093/mnrasl/slu138.
- Y. Fukui, N. Mizuno, R. Yamaguchi, A. Mizuno, T. Onishi, H. Ogawa, Y. Yonekura, A. Kawamura, K. Tachihara, K. Xiao, N. Yamaguchi, A. Hara, T. Hayakawa, S. Kato, R. Abe, H. Saito, S. Mano, K. Matsunaga, Y. Mine, Y. Moriguchi, H. Aoyama, S.-i. Asayama, N. Yoshikawa, and M. Rubio. First Results of a CO Survey of the Large Magellanic Cloud with NANTEN; Giant Molecular Clouds as Formation Sites of Populous Clusters. *PASJ*, 51:745–749, Dec. 1999. doi: 10.1093/pasj/51.6.745.
- Y. Fukui, N. Mizuno, R. Yamaguchi, A. Mizuno, and T. Onishi. On the Mass Spectrum of Giant Molecular Clouds in the Large Magellanic Cloud. *PASJ*, 53:L41–L44, Dec. 2001. doi: 10.1093/pasj/53.6.L41.
- Y. Fukui, A. Kawamura, T. Minamidani, Y. Mizuno, Y. Kanai, N. Mizuno, T. Onishi, Y. Yonekura, A. Mizuno, H. Ogawa, and M. Rubio. The Second Survey of the Molecular Clouds in the Large Magellanic Cloud by NANTEN. I. Catalog of Molecular Clouds. *ApJS*, 178:56–70, Sept. 2008. doi: 10.1086/589833.
- Y. Fukui, A. Ohama, N. Hanaoka, N. Furukawa, K. Torii, J. R. Dawson, N. Mizuno, K. Hasegawa, T. Fukuda, S. Soga, N. Moribe, Y. Kuroda, T. Hayakawa, A. Kawamura, T. Kuwahara, H. Yamamoto, T. Okuda, T. Onishi, H. Maezawa, and A. Mizuno. Molecular Clouds toward the Super Star Cluster NGC 3603 Possible Evidence for a Cloud-Cloud Collision in Triggering the Cluster Formation. *ApJ*, 780:36, Jan. 2014. doi: 10.1088/0004-637X/780/1/36.

- N. Furukawa, J. R. Dawson, A. Ohama, A. Kawamura, N. Mizuno, T. Onishi, and Y. Fukui. Molecular Clouds Toward RCW49 and Westerlund 2: Evidence for Cluster Formation Triggered by Cloud-Cloud Collision. *ApJL*, 696:L115–L119, May 2009. doi: 10.1088/0004-637X/696/2/L115.
- C. F. Gammie. Nonlinear Outcome of Gravitational Instability in Cooling, Gaseous Disks. *ApJ*, 553:174–183, May 2001. doi: 10.1086/320631.
- A. Gatto, S. Walch, M.-M. M. Low, T. Naab, P. Girichidis, S. C. O. Glover, R. Wünsch, R. S. Klessen, P. C. Clark, C. Baczynski, T. Peters, J. P. Ostriker, J. C. Ibáñez-Mejía, and S. Haid. Modelling the supernova-driven ISM in different environments. *MNRAS*, 449:1057–1075, May 2015. doi: 10.1093/mnras/stv324.
- R. Genzel, L. J. Tacconi, J. Gracia-Carpio, A. Sternberg, M. C. Cooper, K. Shapiro, A. Bolatto, N. Bouché, F. Bournaud, A. Burkert, F. Combes, J. Comerford, P. Cox, M. Davis, N. M. F. Schreiber, S. Garcia-Burillo, D. Lutz, T. Naab, R. Neri, A. Omont, A. Shapley, and B. Weiner. A study of the gas-star formation relation over cosmic time. *MNRAS*, 407:2091–2108, Oct. 2010. doi: 10.1111/j.1365-2966.2010.16969.x.
- G. Gilmore and N. Reid. New light on faint stars. III - Galactic structure towards the South Pole and the Galactic thick disc. *MNRAS*, 202:1025–1047, Mar. 1983.
- A. Ginsburg, E. Bressert, J. Bally, and C. Battersby. There are No Starless Massive Proto-clusters in the First Quadrant of the Galaxy. *ApJL*, 758:L29, Oct. 2012. doi: 10.1088/2041-8205/758/2/L29.
- P. Goldreich and D. Lynden-Bell. I. Gravitational stability of uniformly rotating disks. *MNRAS*, 130:97, 1965a.
- P. Goldreich and D. Lynden-Bell. II. Spiral arms as sheared gravitational instabilities. *MNRAS*, 130:125, 1965b.
- R. J. J. Grand, D. Kawata, and M. Cropper. Dynamics of stars around spiral arms in an N-body/SPH simulated barred spiral galaxy. *MNRAS*, 426:167–180, Oct. 2012. doi: 10.1111/j.1365-2966.2012.21733.x.
- R. J. J. Grand, D. Kawata, and M. Cropper. Spiral arm pitch angle and galactic shear rate in N-body simulations of disc galaxies. *A&A*, 553:A77, May 2013. doi: 10.1051/0004-6361/201321308.
- P. Gratier, J. Braine, N. J. Rodriguez-Fernandez, K. F. Schuster, C. Kramer, E. Corbelli, F. Combes, N. Brouillet, P. P. van der Werf, and M. Röllig. Giant molecular clouds in the Local Group galaxy M 33. *A&A*, 542:A108, June 2012. doi: 10.1051/0004-6361/201116612.
- A. Habe and K. Ohta. Gravitational instability induced by a cloud-cloud collision - The case of head-on collisions between clouds with different sizes and densities. *PASJ*, 44:203–226, June 1992.
- T. Handa, N. Nakai, Y. Sofue, M. Hayashi, and M. Fujimoto. CO line observations of the bar and nucleus of the barred spiral galaxy M83. *PASJ*, 42:1–17, Feb. 1990.
- J. Harris, D. Calzetti, J. S. Gallagher, III, C. J. Conselice, and D. A. Smith. Young Clusters in the Nuclear Starburst of M83. *AJ*, 122:3046–3064, Dec. 2001. doi: 10.1086/324230.
- M. Heyer, C. Krawczyk, J. Duval, and J. M. Jackson. Re-Examining Larson’s Scaling Relationships in Galactic Molecular Clouds. *ApJ*, 699:1092–1103, July 2009. doi: 10.1088/0004-637X/699/2/1092.
- A. Hirota, N. Kuno, N. Sato, H. Nakanishi, T. Tosaki, H. Matsui, A. Habe, and K. Sorai. Determination of the Pattern Speed of Barred Spiral Galaxies. *PASJ*, 61:441–, June 2009. doi: 10.1093/pasj/61.3.441.
- A. Hirota, N. Kuno, N. Sato, H. Nakanishi, T. Tosaki, and K. Sorai. Giant Molecular Clouds in the Spiral Arm of IC 342. *ApJ*, 737:40, Aug. 2011. doi: 10.1088/0004-637X/737/1/40.
- A. Hirota, N. Kuno, J. Baba, F. Egusa, A. Habe, K. Muraoka, A. Tanaka, H. Nakanishi, and R. Kawabe. Wide-field ^{12}CO ($J = 1-0$) imaging of the nearby barred galaxy M 83 with NMA and Nobeyama 45 m telescope: Molecular gas kinematics and star formation along the bar. *PASJ*, 66:46, Apr. 2014. doi: 10.1093/pasj/psu006.
- V. Hoffmann and A. B. Romeo. The effect of ISM turbulence on the gravitational instability of galactic discs. *MNRAS*, 425:1511–1520, Sept. 2012. doi: 10.1111/j.1365-2966.2012.21675.x.
- P. F. Hopkins, E. Quataert, and N. Murray. Self-regulated star formation in galaxies via momentum input from massive stars. *MNRAS*, 417:950–973, Oct. 2011. doi: 10.1111/j.1365-2966.2011.19306.x.
- P. F. Hopkins, E. Quataert, and N. Murray. The structure of the interstellar medium of star-forming galaxies. *MNRAS*, 421:3488–3521, Apr. 2012. doi: 10.1111/j.1365-2966.2012.20578.x.
- E. P. Hubble. Extragalactic nebulae. *ApJ*, 64:321–369, Dec. 1926. doi: 10.1086/143018.
- W. K. Huchtmeier and H.-D. Bohnenstengel. The extended H I-envelope of NGC 5236 /M83/. *A&A*, 100:72–78, July 1981.
- A. Hughes, T. Wong, J. Ott, E. Muller, J. L. Pineda, Y. Mizuno, J.-P. Bernard, D. Paradis, S. Maddison, W. T. Reach, L. Staveley-Smith, A. Kawamura, M. Meixner, S. Kim, T. Onishi, N. Mizuno, and Y. Fukui. Physical properties of giant molecular clouds in the Large Magellanic Cloud. *MNRAS*, 406:2065–2086, Aug. 2010. doi:

- 10.1111/j.1365-2966.2010.16829.x.
- A. Hughes, S. E. Meidt, D. Colombo, E. Schinnerer, J. Pety, A. K. Leroy, C. L. Dobbs, S. García-Burillo, T. A. Thompson, G. Dumas, K. F. Schuster, and C. Kramer. A Comparative Study of Giant Molecular Clouds in M51, M33, and the Large Magellanic Cloud. *ApJ*, 779:46, Dec. 2013. doi: 10.1088/0004-637X/779/1/46.
- T. Inoue and Y. Fukui. Formation of Massive Molecular Cloud Cores by Cloud-Cloud Collision. *ApJL*, 774:L31, Sept. 2013. doi: 10.1088/2041-8205/774/2/L31.
- T. Inoue, R. Yamazaki, and S.-i. Inutsuka. Turbulence and Magnetic Field Amplification in Supernova Remnants: Interactions Between a Strong Shock Wave and Multiphase Interstellar Medium. *ApJ*, 695:825–833, Apr. 2009. doi: 10.1088/0004-637X/695/2/825.
- T. H. Jarrett, T. Chester, R. Cutri, S. E. Schneider, and J. P. Huchra. The 2MASS Large Galaxy Atlas. *AJ*, 125:525–554, Feb. 2003. doi: 10.1086/345794.
- W. H. Julian and A. Toomre. Non-Axisymmetric Responses of Differentially Rotating Disks of Stars. *ApJ*, 146: 810, Dec. 1966. doi: 10.1086/148957.
- A. Kawamura, Y. Mizuno, T. Minamidani, M. D. Filipović, L. Staveley-Smith, S. Kim, N. Mizuno, T. Onishi, A. Mizuno, and Y. Fukui. The Second Survey of the Molecular Clouds in the Large Magellanic Cloud by NANTEN. II. Star Formation. *ApJS*, 184:1–17, Sept. 2009. doi: 10.1088/0067-0049/184/1/1.
- J. D. P. Kenney and S. D. Lord. Orbit crowding of molecular gas at a bar-spiral arm transition zone in M83. *ApJ*, 381:118–129, Nov. 1991. doi: 10.1086/170634.
- R. C. Kennicutt, Jr. The star formation law in galactic disks. *ApJ*, 344:685–703, Sept. 1989. doi: 10.1086/167834.
- R. C. Kennicutt, Jr. The Global Schmidt Law in Star-forming Galaxies. *ApJ*, 498:541–552, May 1998. doi: 10.1086/305588.
- R. C. Kennicutt, Jr., D. Calzetti, F. Walter, G. Helou, D. J. Hollenbach, L. Armus, G. Bendo, D. A. Dale, B. T. Draine, C. W. Engelbracht, K. D. Gordon, M. K. M. Prescott, M. W. Regan, M. D. Thornley, C. Bot, E. Brinks, E. de Blok, D. de Mello, M. Meyer, J. Moustakas, E. J. Murphy, K. Sheth, and J. D. T. Smith. Star Formation in NGC 5194 (M51a). II. The Spatially Resolved Star Formation Law. *ApJ*, 671:333–348, Dec. 2007. doi: 10.1086/522300.
- S. A. Khoperskov, E. O. Vasiliev, D. A. Ladeyschikov, A. M. Sobolev, and A. V. Khoperskov. GMCs scaling relations: role of the cloud definition. *ArXiv e-prints*, Aug. 2015.
- A. Klypin, A. V. Kravtsov, O. Valenzuela, and F. Prada. Where Are the Missing Galactic Satellites? *ApJ*, 522: 82–92, Sept. 1999. doi: 10.1086/307643.
- J. Koda, N. Scoville, T. Sawada, M. A. La Vigne, S. N. Vogel, A. E. Potts, J. M. Carpenter, S. A. Corder, M. C. H. Wright, S. M. White, B. A. Zauderer, J. Patience, A. I. Sargent, D. C. J. Bock, D. Hawkins, M. Hodges, A. Kembell, J. W. Lamb, R. L. Plambeck, M. W. Pound, S. L. Scott, P. Teuben, and D. P. Woody. Dynamically Driven Evolution of the Interstellar Medium in M51. *ApJL*, 700:L132–L136, Aug. 2009. doi: 10.1088/0004-637X/700/2/L132.
- J. Koda, N. Scoville, T. Hasegawa, D. Calzetti, J. Donovan Meyer, F. Egusa, R. Kennicutt, N. Kuno, M. Louie, R. Momose, T. Sawada, K. Sorai, and M. Umei. Physical Conditions in Molecular Clouds in the Arm and Interarm Regions of M51. *ApJ*, 761:41, Dec. 2012. doi: 10.1088/0004-637X/761/1/41.
- A. Kolmogorov. The Local Structure of Turbulence in Incompressible Viscous Fluid for Very Large Reynolds' Numbers. *Akademiia Nauk SSSR Doklady*, 30:301–305, 1941.
- J. Kormendy and R. Bender. A Proposed Revision of the Hubble Sequence for Elliptical Galaxies. *ApJL*, 464: L119, June 1996. doi: 10.1086/310095.
- M. R. Krumholz and C. F. McKee. A General Theory of Turbulence-regulated Star Formation, from Spirals to Ultraluminous Infrared Galaxies. *ApJ*, 630:250–268, Sept. 2005. doi: 10.1086/431734.
- M. R. Krumholz and J. C. Tan. Slow Star Formation in Dense Gas: Evidence and Implications. *ApJ*, 654: 304–315, Jan. 2007. doi: 10.1086/509101.
- C. J. Lada, M. Margulis, Y. Sofue, N. Nakai, and T. Handa. Observations of molecular and atomic clouds in M31. *ApJ*, 328:143–160, May 1988. doi: 10.1086/166275.
- C. J. Lada, M. Lombardi, and J. F. Alves. On the Star Formation Rates in Molecular Clouds. *ApJ*, 724:687–693, Nov. 2010. doi: 10.1088/0004-637X/724/1/687.
- E. A. Lada and L. Blitz. Two populations of diffuse molecular clouds. *ApJL*, 326:L69–L73, Mar. 1988. doi: 10.1086/185125.

- S. S. Larsen and T. Richtler. Young massive star clusters in nearby galaxies . I. Identification and general properties of the cluster systems. *A&A*, 345:59–72, May 1999.
- R. B. Larson. Turbulence and star formation in molecular clouds. *MNRAS*, 194:809–826, Mar. 1981.
- A. Leroy, A. Bolatto, F. Walter, and L. Blitz. Molecular Gas in the Low-Metallicity, Star-forming Dwarf IC 10. *ApJ*, 643:825–843, June 2006. doi: 10.1086/503024.
- A. K. Leroy, F. Walter, E. Brinks, F. Bigiel, W. J. G. de Blok, B. Madore, and M. D. Thornley. The Star Formation Efficiency in Nearby Galaxies: Measuring Where Gas Forms Stars Effectively. *AJ*, 136:2782–2845, Dec. 2008. doi: 10.1088/0004-6256/136/6/2782.
- A. K. Leroy, F. Walter, F. Bigiel, A. Usero, A. Weiss, E. Brinks, W. J. G. de Blok, R. C. Kennicutt, K.-F. Schuster, C. Kramer, H. W. Wiesemeyer, and H. Roussel. Heracles: The HERA CO Line Extragalactic Survey. *AJ*, 137:4670–4696, June 2009. doi: 10.1088/0004-6256/137/6/4670.
- A. K. Leroy, F. Walter, K. Sandstrom, A. Schrubba, J.-C. Munoz-Mateos, F. Bigiel, A. Bolatto, E. Brinks, W. J. G. de Blok, S. Meidt, H.-W. Rix, E. Rosolowsky, E. Schinnerer, K.-F. Schuster, and A. Usero. Molecular Gas and Star Formation in nearby Disk Galaxies. *AJ*, 146:19, Aug. 2013. doi: 10.1088/0004-6256/146/2/19.
- C. C. Lin and F. H. Shu. On the Spiral Structure of Disk Galaxies. *ApJ*, 140:646, Aug. 1964. doi: 10.1086/147955.
- F. J. Lockman. The H I halo in the inner galaxy. *ApJ*, 283:90–97, Aug. 1984. doi: 10.1086/162277.
- M. Lombardi, J. Alves, and C. J. Lada. Larson’s third law and the universality of molecular cloud structure. *A&A*, 519:L7, Sept. 2010. doi: 10.1051/0004-6361/201015282.
- S. D. Lord and J. D. P. Kenney. A molecular gas ridge offset from the dust lane in a spiral arm of M83. *ApJ*, 381:130–136, Nov. 1991. doi: 10.1086/170635.
- R. B. Loren. Colliding clouds and star formation in NGC 1333. *ApJ*, 209:466, Oct. 1976. doi: 10.1086/154741.
- A. A. Lundgren, H. Olofsson, T. Wiklund, and G. Rydbeck. Molecular gas in the galaxy M 83. II. Kinematics of the molecular gas. *A&A*, 422:865–881, Aug. 2004a. doi: 10.1051/0004-6361:20040230.
- A. A. Lundgren, T. Wiklund, H. Olofsson, and G. Rydbeck. Molecular gas in the galaxy M 83. I. The molecular gas distribution. *A&A*, 413:505–523, Jan. 2004b. doi: 10.1051/0004-6361:20031507.
- M.-M. Mac Low, R. S. Klessen, A. Burkert, and M. D. Smith. Kinetic Energy Decay Rates of Supersonic and Super-Alfvénic Turbulence in Star-Forming Clouds. *Physical Review Letters*, 80:2754–2757, Mar. 1998. doi: 10.1103/PhysRevLett.80.2754.
- M. E. Machacek, G. L. Bryan, and T. Abel. Simulations of Pregalactic Structure Formation with Radiative Feedback. *ApJ*, 548:509–521, Feb. 2001. doi: 10.1086/319014.
- C. F. McKee and J. P. Ostriker. A theory of the interstellar medium - Three components regulated by supernova explosions in an inhomogeneous substrate. *ApJ*, 218:148–169, Nov. 1977. doi: 10.1086/155667.
- S. E. Meidt, E. Schinnerer, S. García-Burillo, A. Hughes, D. Colombo, J. Pety, C. L. Dobbs, K. F. Schuster, C. Kramer, A. K. Leroy, G. Dumas, and T. A. Thompson. Gas Kinematics on Giant Molecular Cloud Scales in M51 with PAWS: Cloud Stabilization through Dynamical Pressure. *ApJ*, 779:45, Dec. 2013. doi: 10.1088/0004-637X/779/1/45.
- S. E. Meidt, A. Hughes, C. L. Dobbs, J. Pety, T. A. Thompson, S. García-Burillo, A. K. Leroy, E. Schinnerer, D. Colombo, M. Querejeta, C. Kramer, K. F. Schuster, and G. Dumas. Short GMC Lifetimes: An Observational Estimate with the PdBI Arcsecond Whirlpool Survey (PAWS). *ApJ*, 806:72, June 2015. doi: 10.1088/0004-637X/806/1/72.
- R. E. Miura, K. Kohno, T. Tosaki, D. Espada, N. Hwang, N. Kuno, S. K. Okumura, A. Hirota, K. Muraoka, S. Onodera, T. Minamidani, S. Komugi, K. Nakanishi, T. Sawada, H. Kaneko, and R. Kawabe. Giant Molecular Cloud Evolutions in the Nearby Spiral Galaxy M33. *ApJ*, 761:37, Dec. 2012. doi: 10.1088/0004-637X/761/1/37.
- R. E. Miura, K. Kohno, T. Tosaki, D. Espada, A. Hirota, S. Komugi, S. K. Okumura, N. Kuno, K. Muraoka, S. Onodera, K. Nakanishi, T. Sawada, H. Kaneko, T. Minamidani, K. Fujii, and R. Kawabe. Enhancement of CO(3-2)/CO(1-0) Ratios and Star Formation Efficiencies in Supergiant H II Regions. *ApJ*, 788:167, June 2014. doi: 10.1088/0004-637X/788/2/167.
- M.-A. Miville-Deschênes, G. Joncas, E. Falgarone, and F. Boulanger. High resolution 21 cm mapping of the Ursa Major Galactic cirrus: Power spectra of the high-latitude H I gas. *A&A*, 411:109–121, Nov. 2003. doi: 10.1051/0004-6361:20031297.
- N. Mizuno, M. Rubio, A. Mizuno, R. Yamaguchi, T. Onishi, and Y. Fukui. First Results of a CO Survey of the Small Magellanic Cloud with NANTEN. *PASJ*, 53:L45–L49, Dec. 2001a. doi: 10.1093/pasj/53.6.L45.

- N. Mizuno, R. Yamaguchi, A. Mizuno, M. Rubio, R. Abe, H. Saito, T. Onishi, Y. Yonekura, N. Yamaguchi, H. Ogawa, and Y. Fukui. A CO Survey of the LMC with NANTEN: II. Catalog of Molecular Clouds. *PASJ*, 53:971–984, Dec. 2001b. doi: 10.1093/pasj/53.6.971.
- R. Momose, S. K. Okumura, J. Koda, and T. Sawada. Star Formation Efficiency in the Barred Spiral Galaxy NGC 4303. *ApJ*, 721:383–394, Sept. 2010. doi: 10.1088/0004-637X/721/1/383.
- B. Moore, S. Ghigna, F. Governato, G. Lake, T. Quinn, J. Stadel, and P. Tozzi. Dark Matter Substructure within Galactic Halos. *ApJL*, 524:L19–L22, Oct. 1999. doi: 10.1086/312287.
- K. Muraoka, K. Kohno, T. Tosaki, N. Kuno, K. Nakanishi, K. Sorai, T. Okuda, S. Sakamoto, A. Endo, B. Hatsukade, K. Kamegai, K. Tanaka, J. Cortes, H. Ezawa, N. Yamaguchi, T. Sakai, and R. Kawabe. ASTE CO (3-2) Observations of the Barred Spiral Galaxy M 83: I. Correlation between CO (3-2)/ CO (1-0) Ratios and Star Formation Efficiencies. *PASJ*, 59:43–54, Feb. 2007. doi: 10.1093/pasj/59.1.43.
- K. Muraoka, K. Kohno, T. Tosaki, N. Kuno, K. Nakanishi, T. Handa, K. Sorai, S. Ishizuki, and T. Okuda. Nobeyama Millimeter Array Observations of the Nuclear Starburst of M 83: A GMA Scale Correlation between Dense Gas Fraction and Star Formation Efficiency. *PASJ*, 61:163–, Feb. 2009a. doi: 10.1093/pasj/61.2.163.
- K. Muraoka, K. Kohno, T. Tosaki, N. Kuno, K. Nakanishi, K. Sorai, T. Sawada, K. Tanaka, T. Handa, M. Fukuhara, H. Ezawa, and R. Kawabe. ASTE CO (3-2) Mapping Toward the Whole Optical Disk of M 83: Properties of Inter-arm Giant Molecular-Cloud Associations. *ApJ*, 706:1213–1225, Dec. 2009b. doi: 10.1088/0004-637X/706/2/1213.
- P. C. Myers. A compilation of interstellar gas properties. *ApJ*, 225:380–389, Oct. 1978. doi: 10.1086/156500.
- J. F. Navarro, C. S. Frenk, and S. D. M. White. A Universal Density Profile from Hierarchical Clustering. *ApJ*, 490:493–508, Dec. 1997.
- M. Nimori, A. Habe, K. Sorai, Y. Watanabe, A. Hirota, and D. Namekata. Dense cloud formation and star formation in a barred galaxy. *MNRAS*, 429:2175–2182, Mar. 2013. doi: 10.1093/mnras/sts487.
- C. A. Norman and A. Ferrara. The Turbulent Interstellar Medium: Generalizing to a Scale-dependent Phase Continuum. *ApJ*, 467:280, Aug. 1996. doi: 10.1086/177603.
- S. Odenwald, J. Fischer, F. J. Lockman, and S. Stemwedel. The unusual cometary star-forming region G110-13. *ApJ*, 397:174–186, Sept. 1992. doi: 10.1086/171777.
- S. H. Oh, W.-T. Kim, H. M. Lee, and J. Kim. Physical Properties of Tidal Features in Interacting Disk Galaxies. *ApJ*, 683:94–113, Aug. 2008. doi: 10.1086/588184.
- A. Ohama, J. R. Dawson, N. Furukawa, A. Kawamura, N. Moribe, H. Yamamoto, T. Okuda, N. Mizuno, T. Onishi, H. Maezawa, T. Minamidani, A. Mizuno, and Y. Fukui. Temperature and Density Distribution in the Molecular Gas Toward Westerlund 2: Further Evidence for Physical Association. *ApJ*, 709:975–982, Feb. 2010. doi: 10.1088/0004-637X/709/2/975.
- T. Oka, T. Hasegawa, F. Sato, M. Tsuboi, A. Miyazaki, and M. Sugimoto. Statistical Properties of Molecular Clouds in the Galactic Center. *ApJ*, 562:348–362, Nov. 2001. doi: 10.1086/322976.
- M. P. Ondrechen. Radio continuum observations of the bar and disk of M83. *AJ*, 90:1474–1480, Aug. 1985. doi: 10.1086/113857.
- J. P. Ostriker and P. J. E. Peebles. A Numerical Study of the Stability of Flattened Galaxies: or, can Cold Galaxies Survive? *ApJ*, 186:467–480, Dec. 1973. doi: 10.1086/152513.
- P. Padoan, S. Kim, A. Goodman, and L. Staveley-Smith. A New Method to Measure and Map the Gas Scale Height of Disk Galaxies. *ApJL*, 555:L33–L36, July 2001. doi: 10.1086/321735.
- P. Padoan, C. Federrath, G. Chabrier, N. J. Evans, II, D. Johnstone, J. K. Jørgensen, C. F. McKee, and Å. Nordlund. The Star Formation Rate of Molecular Clouds. *Protostars and Planets VI*, pages 77–100, 2014. doi: 10.2458/azu_uapress.9780816531240-ch004.
- A. R. Pettitt, C. L. Dobbs, D. M. Acreman, and D. J. Price. The morphology of the Milky Way - I. Reconstructing CO maps from simulations in fixed potentials. *MNRAS*, 444:919–941, Oct. 2014. doi: 10.1093/mnras/stu1075.
- R. J. Rand, S. D. Lord, and J. L. Higdon. The Eastern Arm of M83 Revisited: High-Resolution Mapping of ^{12}CO 1-0 Emission. *ApJ*, 513:720–732, Mar. 1999. doi: 10.1086/306897.
- D. Rebolledo, T. Wong, A. Leroy, J. Koda, and J. Donovan Meyer. Giant Molecular Clouds and Star Formation in the Non-grand Design Spiral Galaxy NGC 6946. *ApJ*, 757:155, Oct. 2012. doi: 10.1088/0004-637X/757/2/155.
- D. Rebolledo, T. Wong, R. Xue, A. Leroy, J. Koda, and J. Donovan Meyer. Scaling Relations of the Properties for CO Resolved Structures in Nearby Spiral Galaxies. *ApJ*, 808:99, July 2015. doi: 10.1088/0004-637X/808/1/99.

- F. Renaud, F. Bournaud, E. Emsellem, B. Elmegreen, R. Teyssier, J. Alves, D. Chapon, F. Combes, A. Dekel, J. Gabor, P. Hennebelle, and K. Kraljic. A sub-parsec resolution simulation of the Milky Way: global structure of the interstellar medium and properties of molecular clouds. *MNRAS*, 436:1836–1851, Dec. 2013. doi: 10.1093/mnras/stt1698.
- D. Reynaud and D. Downes. Kinematics of the gas in a barred galaxy: do strong shocks inhibit star formation? *A&A*, 337:671–680, Sept. 1998.
- G. H. Rieke. The sizes of the nuclei of galaxies at 10 microns. *ApJL*, 206:L15–L17, May 1976. doi: 10.1086/182122.
- W. W. Roberts. Large-Scale Shock Formation in Spiral Galaxies and its Implications on Star Formation. *ApJ*, 158:123, Oct. 1969. doi: 10.1086/150177.
- J. Roman-Duval, J. M. Jackson, M. Heyer, J. Rathborne, and R. Simon. Physical Properties and Galactic Distribution of Molecular Clouds Identified in the Galactic Ring Survey. *ApJ*, 723:492–507, Nov. 2010. doi: 10.1088/0004-637X/723/1/492.
- A. B. Romeo, A. Burkert, and O. Agertz. A Toomre-like stability criterion for the clumpy and turbulent interstellar medium. *MNRAS*, 407:1223–1230, Sept. 2010. doi: 10.1111/j.1365-2966.2010.16975.x.
- A. Rosen and J. N. Bregman. Global Models of the Interstellar Medium in Disk Galaxies. *ApJ*, 440:634, Feb. 1995. doi: 10.1086/175303.
- E. Rosolowsky. Giant Molecular Clouds in M31. I. Molecular Cloud Properties. *ApJ*, 654:240–251, Jan. 2007. doi: 10.1086/509249.
- E. Rosolowsky and L. Blitz. Giant Molecular Clouds in M64. *ApJ*, 623:826–845, Apr. 2005. doi: 10.1086/428897.
- E. Rosolowsky, G. Engargiola, R. Plambeck, and L. Blitz. Giant Molecular Clouds in M33. II. High-Resolution Observations. *ApJ*, 599:258–274, Dec. 2003. doi: 10.1086/379166.
- E. Rosolowsky, E. Keto, S. Matsushita, and S. P. Willner. High-Resolution Molecular Gas Maps of M33. *ApJ*, 661:830–844, June 2007. doi: 10.1086/516621.
- K. S. Rumstay and M. Kaufman. H II regions and star formation in M83 and M33. *ApJ*, 274:611–631, Nov. 1983. doi: 10.1086/161474.
- K. Sakamoto, S. Matsushita, A. B. Peck, M. C. Wiedner, and D. Iono. Molecular Gas around the Double Nucleus in M83. *ApJL*, 616:L59–L62, Nov. 2004. doi: 10.1086/420845.
- F. Salmi, E. Daddi, D. Elbaz, M. T. Sargent, M. Dickinson, A. Renzini, M. Bethermin, and D. Le Borgne. Dissecting the Stellar-mass-SFR Correlation in $z = 1$ Star-forming Disk Galaxies. *ApJL*, 754:L14, July 2012. doi: 10.1088/2041-8205/754/1/L14.
- E. E. Salpeter. The Luminosity Function and Stellar Evolution. *ApJ*, 121:161, Jan. 1955. doi: 10.1086/145971.
- D. B. Sanders, P. M. Solomon, and N. Z. Scoville. Giant molecular clouds in the Galaxy. I - The axisymmetric distribution of H₂. *ApJ*, 276:182–203, Jan. 1984. doi: 10.1086/161602.
- C. L. Sarazin and R. E. White, III. Steady state cooling flow models for normal elliptical galaxies. *ApJ*, 320: 32–48, Sept. 1987. doi: 10.1086/165522.
- M. Schmidt. The Rate of Star Formation. *ApJ*, 129:243, Mar. 1959. doi: 10.1086/146614.
- A. Schrubba, A. K. Leroy, F. Walter, F. Bigiel, E. Brinks, W. J. G. de Blok, G. Dumas, C. Kramer, E. Rosolowsky, K. Sandstrom, K. Schuster, A. Usero, A. Weiss, and H. Wiesemeyer. A Molecular Star Formation Law in the Atomic-gas-dominated Regime in Nearby Galaxies. *AJ*, 142:37, Aug. 2011. doi: 10.1088/0004-6256/142/2/37.
- N. Z. Scoville, D. Thakkar, J. E. Carlstrom, and A. I. Sargent. The scale height and radial distribution of molecular gas in NGC 891. *ApJL*, 404:L59–L62, Feb. 1993. doi: 10.1086/186743.
- L. I. Sedov. *Similarity and Dimensional Methods in Mechanics*. 1959.
- J. A. Sellwood and L. S. Sparke. Pattern speeds in barred spiral galaxies. *MNRAS*, 231:25P–31P, Mar. 1988.
- K. L. Shapiro, R. Genzel, N. M. Förster Schreiber, L. J. Tacconi, N. Bouché, G. Cresci, R. Davies, F. Eisenhauer, P. H. Johansson, D. Krajnović, D. Lutz, T. Naab, N. Arimoto, S. Arribas, A. Cimatti, L. Colina, E. Daddi, O. Daigle, D. Erb, O. Hernandez, X. Kong, M. Mignoli, M. Onodera, A. Renzini, A. Shapley, and C. Steidel. Kinemetry of SINS High-Redshift Star-Forming Galaxies: Distinguishing Rotating Disks from Major Mergers. *ApJ*, 682:231–251, July 2008. doi: 10.1086/587133.
- J. Shen, R. M. Rich, J. Kormendy, C. D. Howard, R. De Propris, and A. Kunder. Our Milky Way as a Pure-disk Galaxy—A Challenge for Galaxy Formation. *ApJL*, 720:L72–L76, Sept. 2010. doi: 10.1088/2041-8205/720/1/L72.

- K. Sheth, S. N. Vogel, M. W. Regan, P. J. Teuben, A. I. Harris, and M. D. Thornley. Molecular Gas and Star Formation in Bars of Nearby Spiral Galaxies. *AJ*, 124:2581–2599, Nov. 2002. doi: 10.1086/343835.
- R. Shetty and E. C. Ostriker. Cloud and Star Formation in Disk Galaxy Models with Feedback. *ApJ*, 684: 978–995, Sept. 2008. doi: 10.1086/590383.
- R. Shetty, C. N. Beaumont, M. G. Burton, B. C. Kelly, and R. S. Klessen. The linewidth-size relationship in the dense interstellar medium of the Central Molecular Zone. *MNRAS*, 425:720–729, Sept. 2012. doi: 10.1111/j.1365-2966.2012.21588.x.
- J. D. Simon and M. Geha. The Kinematics of the Ultra-faint Milky Way Satellites: Solving the Missing Satellite Problem. *ApJ*, 670:313–331, Nov. 2007. doi: 10.1086/521816.
- C. M. Simpson, G. L. Bryan, C. Hummels, and J. P. Ostriker. Kinetic Energy from Supernova Feedback in High-resolution Galaxy Simulations. *ApJ*, 809:69, Aug. 2015. doi: 10.1088/0004-637X/809/1/69.
- P. M. Solomon, A. R. Rivolo, J. Barrett, and A. Yahil. Mass, luminosity, and line width relations of Galactic molecular clouds. *ApJ*, 319:730–741, Aug. 1987. doi: 10.1086/165493.
- K. Sorai, N. Kuno, K. Nishiyama, Y. Watanabe, H. Matsui, A. Habe, A. Hirota, Y. Ishihara, and N. Nakai. Properties of Molecular Gas in the Bar of Maffei 2. *PASJ*, 64:51, June 2012. doi: 10.1093/pasj/64.3.51.
- R. Soria and K. Wu. Properties of discrete X-ray sources in the starburst spiral galaxy M 83. *A&A*, 410:53–74, Oct. 2003. doi: 10.1051/0004-6361:20031074.
- L. S. Sparke and J. S. Gallagher, III. *Galaxies in the universe : an introduction*. Aug. 2000.
- L. S. Sparke and J. A. Sellwood. Dissection of an N-body bar. *MNRAS*, 225:653–675, Apr. 1987.
- L. Spitzer, Jr. Review of Publications: Physical Processes in the Interstellar Medium. *JRASC*, 72:349, Dec. 1978.
- G. Stinson, A. Seth, N. Katz, J. Wadsley, F. Governato, and T. Quinn. Star formation and feedback in smoothed particle hydrodynamic simulations - I. Isolated galaxies. *MNRAS*, 373:1074–1090, Dec. 2006. doi: 10.1111/j.1365-2966.2006.11097.x.
- J. M. Stone and M. L. Norman. ZEUS-2D: A radiation magnetohydrodynamics code for astrophysical flows in two space dimensions. I - The hydrodynamic algorithms and tests. *ApJS*, 80:753–790, June 1992. doi: 10.1086/191680.
- C. Struck, C. L. Dobbs, and J.-S. Hwang. Slowly breaking waves: the longevity of tidally induced spiral structure. *MNRAS*, 414:2498–2510, July 2011. doi: 10.1111/j.1365-2966.2011.18568.x.
- L. J. Tacconi, R. Genzel, R. Neri, P. Cox, M. C. Cooper, K. Shapiro, A. Bolatto, N. Bouché, F. Bournaud, A. Burkert, F. Combes, J. Comerford, M. Davis, N. M. F. Schreiber, S. Garcia-Burillo, J. Gracia-Carpio, D. Lutz, T. Naab, A. Omont, A. Shapley, A. Sternberg, and B. Weiner. High molecular gas fractions in normal massive star-forming galaxies in the young Universe. *Nature*, 463:781–784, Feb. 2010. doi: 10.1038/nature08773.
- K. Takahira, E. J. Tasker, and A. Habe. Do Cloud-Cloud Collisions Trigger High-mass Star Formation? I. Small Cloud Collisions. *ApJ*, 792:63, Sept. 2014. doi: 10.1088/0004-637X/792/1/63.
- J. C. Tan. Star Formation Rates in Disk Galaxies and Circumnuclear Starbursts from Cloud Collisions. *ApJ*, 536:173–184, June 2000. doi: 10.1086/308905.
- E. J. Tasker. Star Formation in Disk Galaxies. II. The Effect Of Star Formation and Photoelectric Heating on the Formation and Evolution of Giant Molecular Clouds. *ApJ*, 730:11, Mar. 2011. doi: 10.1088/0004-637X/730/1/11.
- E. J. Tasker and G. L. Bryan. Simulating Star Formation and Feedback in Galactic Disk Models. *ApJ*, 641: 878–890, Apr. 2006. doi: 10.1086/500567.
- E. J. Tasker and G. L. Bryan. The Effect of the Interstellar Model on Star Formation Properties in Galactic Disks. *ApJ*, 673:810–831, Feb. 2008. doi: 10.1086/523889.
- E. J. Tasker and J. C. Tan. Star Formation in Disk Galaxies. I. Formation and Evolution of Giant Molecular Clouds via Gravitational Instability and Cloud Collisions. *ApJ*, 700:358–375, July 2009. doi: 10.1088/0004-637X/700/1/358.
- E. J. Tasker, J. Wadsley, and R. Pudritz. Star Formation in Disk Galaxies. III. Does Stellar Feedback Result in Cloud Death? *ApJ*, 801:33, Mar. 2015. doi: 10.1088/0004-637X/801/1/33.
- G. Taylor. The Formation of a Blast Wave by a Very Intense Explosion. I. Theoretical Discussion. *Proceedings of the Royal Society of London Series A*, 201:159–174, Mar. 1950. doi: 10.1098/rspa.1950.0049.
- F. Thim, G. A. Tammann, A. Saha, A. Dolphin, A. Sandage, E. Tolstoy, and L. Labhardt. The Cepheid Distance

- to NGC 5236 (M83) with the ESO Very Large Telescope. *ApJ*, 590:256–270, June 2003. doi: 10.1086/374888.
- A. Toomre. On the gravitational stability of a disk of stars. *ApJ*, 139:1217–1238, May 1964. doi: 10.1086/147861.
- A. Toomre. What amplifies the spirals. In S. M. Fall and D. Lynden-Bell, editors, *Structure and Evolution of Normal Galaxies*, pages 111–136, 1981.
- J. K. Truelove, R. I. Klein, C. F. McKee, J. H. Holliman, II, L. H. Howell, and J. A. Greenough. The Jeans Condition: A New Constraint on Spatial Resolution in Simulations of Isothermal Self-gravitational Hydrodynamics. *ApJL*, 489:L179–L183, Nov. 1997. doi: 10.1086/310975.
- A. D. Tubbs. The inhibition of star formation in barred spiral galaxies. *ApJ*, 255:458–466, Apr. 1982. doi: 10.1086/159846.
- J. L. Turner and P. T. P. Ho. Bright radio continuum emission from star formation in the cores of nearby spiral galaxies. *ApJ*, 421:122–139, Jan. 1994. doi: 10.1086/173631.
- S. N. Vogel, F. Boulanger, and R. Ball. Giant molecular clouds in M31. *ApJL*, 321:L145–L149, Oct. 1987. doi: 10.1086/185022.
- K. Wada, J. Baba, and T. R. Saitoh. Interplay between Stellar Spirals and the Interstellar Medium in Galactic Disks. *ApJ*, 735:1, July 2011. doi: 10.1088/0004-637X/735/1/1.
- L. H. Wei, E. Keto, and L. C. Ho. Two Populations of Molecular Clouds in the Antennae Galaxies. *ApJ*, 750:136, May 2012. doi: 10.1088/0004-637X/750/2/136.
- T. Wiklind, G. Rydbeck, A. Hjalmarson, and P. Bergman. Arm and interarm molecular clouds in M 83. *A&A*, 232:L11–L14, June 1990.
- D. J. Williamson, R. J. Thacker, J. Wurster, and B. K. Gibson. Cloud angular momentum and effective viscosity in global SPH simulations with feedback. *MNRAS*, 442:3674–3685, Aug. 2014. doi: 10.1093/mnras/stu1121.
- C. D. Wilson. First observations of individual molecular clouds in the irregular galaxy NGC 6822. *ApJL*, 434:L11–L14, Oct. 1994. doi: 10.1086/187560.
- C. D. Wilson and I. N. Reid. Giant molecular clouds and the CO-to-H₂ conversion factor in IC 10. *ApJL*, 366:L11–L14, Jan. 1991. doi: 10.1086/185898.
- C. D. Wilson and A. L. Rudolph. Interferometric observations of three giant molecular clouds in M31. *ApJ*, 406:477–481, Apr. 1993. doi: 10.1086/172459.
- C. D. Wilson and N. Scoville. The properties of individual giant molecular clouds in M33. *ApJ*, 363:435–450, Nov. 1990. doi: 10.1086/169356.
- M. G. Wolfire, D. Hollenbach, C. F. McKee, A. G. G. M. Tielens, and E. L. O. Bakes. The neutral atomic phases of the interstellar medium. *ApJ*, 443:152–168, Apr. 1995. doi: 10.1086/175510.
- M. G. Wolfire, C. F. McKee, D. Hollenbach, and A. G. G. M. Tielens. Neutral Atomic Phases of the Interstellar Medium in the Galaxy. *ApJ*, 587:278–311, Apr. 2003. doi: 10.1086/368016.
- T. Wong and L. Blitz. The Relationship between Gas Content and Star Formation in Molecule-rich Spiral Galaxies. *ApJ*, 569:157–183, Apr. 2002. doi: 10.1086/339287.
- A. V. Zasov and S. A. Khoperskov. Giant molecular clouds in M33: are they susceptible to dynamical friction? *MNRAS*, 452:4247–4251, Oct. 2015. doi: 10.1093/mnras/stv1511.